iScience

CellPress
OPEN ACCESS

Review

Carbon-based material-supported single-atom catalysts for energy conversion

Huimin Zhang,[1,2] Wenhao Liu,[1,2] Dong Cao,[1,*] and Daojian Cheng[1,*]

SUMMARY

In recent years, single-atom catalysts (SACs) with unique electronic structure and coordination environment have attracted much attention due to its maximum atomic efficiency in the catalysis fields. However, it is still a great challenge to rationally regulate the coordination environments of SACs and improve the loading of metal atoms for SACs during catalysis progress. Generally, carbon-based materials with excellent electrical conductivity and large specific surface area are widely used as catalyst supports to stabilize metal atoms. Meanwhile, carbon-based material-supported SACs have also been extensively studied and applied in various energy conversion reactions, such as hydrogen evolution reaction (HER), oxygen evolution reaction (OER), oxygen reduction reaction (ORR), carbon dioxide reduction reaction (CO_2RR), and nitrogen reduction reaction (NRR). Herein, rational synthesis methods and advanced characterization techniques were introduced and summarized in this review. Then, the theoretical design strategies and construction methods for carbon-based material-supported SACs in electrocatalysis applications were fully discussed, which are of great significance for guiding the coordination regulation and improving the loading of SACs. In the end, the challenges and future perspectives of SACs were proposed, which could largely contribute to the development of single atom catalysts at the turning point.

INTRODUCTION

Generally, catalysts include homogeneous catalysts and heterogeneous catalysts. Homogeneous catalysts have relatively uniform active centers, higher activity and selectivity, and fewer side reactions, but they are hard to separate, recover, and regenerate from the reaction system. Heterogeneous catalysts are easily separated from the system and can be used repeatedly, but the activity and selectivity of heterogeneous catalysts are often worse than that of homogeneous catalysts. Importantly, single-atom catalyst (SAC), a new type of catalyst, was developed, which is considered to be a bridge between homogeneous catalysts and heterogeneous catalysts due to the distinguished selectivity, catalytic activity, and easy to separation (Chen et al., 2018c; Mao et al., 2019; Sun et al., 2019b; Yang et al., 2013). In recent years, many research have contributed to the developments of single atoms catalysis, but the understanding of single atoms from atomic and electronic insights is still inadequate due to the deficiency of characterization techniques. Therefore, it is very important to comprehend the development process, synthesis methods, and coordination regulation approaches thoroughly for SACs.

In 1995, Thomas and colleagues studied isolated single atom of Titanium as the active site of heterogeneous catalyst (Maschmeyer et al., 1995). In 2000, the presence of single atoms was discovered when size-selected Pd_n ($1 \leq n \leq 30$) cluster supported on MgO were prepared by using a mass separation soft landing technique (Abbet et al., 2000). In 2003, single-site Au species on ceria-based catalyst for water-gas shift were reported by Fu and colleagues (Fu et al., 2003). In 2007, mesoporous Pd/Al_2O_3 with single sites was prepared by impregnation method for selective aerobic oxidation of allyl alcohol (Hackett et al., 2007). With the development of characterization techniques, the concept of "single atom" was first proposed by Zhang and colleagues in 2011 (Qiao et al., 2011). The isolated single Pt atoms fabricated on the surfaces of iron oxide (Pt_1/FeO_x) displayed high activity and selectivity in CO oxidation. In recent years, the design and preparation of atomically dispersed catalysts have attracted extensive research interests in plenty of applications, such as photocatalysis, organic catalysis, electrocatalysis, and environmental and

[1]State Key Laboratory of Organic-Inorganic Composites, Beijing Advanced Innovation Center for Soft Matter Science and Engineering, Beijing University of Chemical Technology, Beijing 100029, People's Republic of China

[2]These authors contributed equally

*Correspondence: caod@mail.buct.edu.cn (D.C.), chengdj@mail.buct.edu.cn (D.C.)

https://doi.org/10.1016/j.isci.2022.104367

energy aspect. Meanwhile, because of the high surface free energy of single atoms, it is still a major challenge to increase the loading capacity of single atoms. What's more, the coordination environments, including the coordination number, the coordination atom, and the distance between the center atoms and the neighboring atoms, greatly influence the catalytic activity of single-atom catalysts (Cook and Borovik, 2015; Mao et al., 2019; Sun et al., 2019b; Tao et al., 2020). Therefore, how to systematically regulate the coordination environments is of great significance to the screening of efficient single-atom catalysts (Lang et al., 2019; Liang et al., 2019; Liu et al., 2019a; Qiao et al., 2015).

The coordination environment and the loading of metal atoms are closely related to the catalytic performance of SACs. In order to further study the regulation of coordination environment and loading, a variety of materials are used as supports for single-atom catalysts, including metal and metal oxide (Cao and Lu, 2020; Ma et al., 2021), sulfide (Feng et al., 2018; Li et al., 2022), phosphide (Jiang et al., 2020), zeolites (Sun et al., 2019a), metal-organic frameworks (MOFs) (Zhou et al., 2021a), covalent organic frameworks (COFs) (Liu et al., 2020), and carbon-based materials (Guo et al., 2021), such as graphene, graphdiyne, and hexagonal boron nitride. Among these carriers, carbon-based materials are regarded as the promising candidate materials for large-scale production of SACs due to low cost, superb conductivity, tunable physicochemical property, and high specific surface area (Georgakilas et al., 2015; Shaik et al., 2019; Su et al., 2013). Therefore, the overview and summary of carbon-based-material-supported SACs are necessary for the improvement of future work.

In this review, we summarized the synthesis methods of SACs supported on carbon-based materials and then highlighted the great significance to guide the coordination regulation of single atoms and improve the loading of SACs. Then, we introduced the advanced characterization techniques, including *ex situ* and *in situ* technologies, which is vital to learn about the SACs from atomic and electronic levels. Most important of all, the applications of carbon-based-material-supported SACs in electrocatalysis are discussed by combining calculations and experiments, and the coordination environment and metal loading of the SACs are emphasized, involving hydrogen evolution reaction (HER), oxygen evolution reaction (OER), oxygen reduction reaction (ORR), carbon dioxide reduction reaction (CO_2RR), and nitrogen reduction reaction (NRR). In the end, the challenges and development opportunities of SACs are fully discussed. We believed that this review could provide essential information to rationally construct SACs in the future.

RATIONAL CONSTRUCTION STRATEGIES

SACs usually display superb catalytic activities for electrochemical reactions, hydrogenation reactions, and so on. However, the highly dispersed single-atoms tend to migration and agglomerate during the synthesis process due to the high surface energy. How to synthesize stable and high-loaded single-atom catalysts requires continuous exploration. In this section, the methods of atomic layer deposition (ALD), impregnation strategy, electrochemical deposition, chemical vapor deposition (CVD), balling milling, and pyrolysis strategy are summarized. Notably, impregnation strategy and pyrolysis strategies are beneficial to the large-scale preparation of SACs in industry.

Atomic layer deposition

Atomic layer deposition (ALD) has a promising future in the synthesis of small size catalysts. In the ALD process, the substrate is alternately exposed to different reactions of precursor vapors. The material could be deposited in atomic layers by sequential and self-limiting surface reactions. Previous studies have shown that ALD can control the morphologies of deposited metals, from tiny discrete nanoparticles to continuous films, by surface chemistry strategy (King et al., 2008; Liu et al., 2009). Meanwhile, ALD can precisely control the size and distribution of particles on the substrate (George, 2010; Marichy et al., 2012). In 2013, single Pt atoms on graphene nanosheets with low coordination were prepared by using ALD technique for the first time (Sun et al., 2013). The container for graphene was placed directly on the heated stage of ALD. $MeCpPtMe_3$ acted as the precursor keeping at 65°C to provide a steady state flux to the reactor (~800 mTorr). Gas lines were heated to 100–150°C to avoid precursor condensation. High purity O_2 and N_2 were used as the counter reactant and purging gas, respectively. The reaction took place at 250°C with the pulse of 1 s of $MeCpPtMe_3$, 20 s of N_2 purge, and 5 s of O_2 in an ALD cycles. By increasing the number of ALD cycles, the size of prepared catalysts can be precisely regulated, including single atoms, sub-nanometer clusters, and nanoparticles, while affecting the coordination number of the metal center atom. Similarly, isolated Pt single-atoms and clusters were fabricated on the nitrogen-doped graphene nanosheets through the same ALD synthesis approach expect for the carrier (Cheng et al., 2016; Figure 1A). There

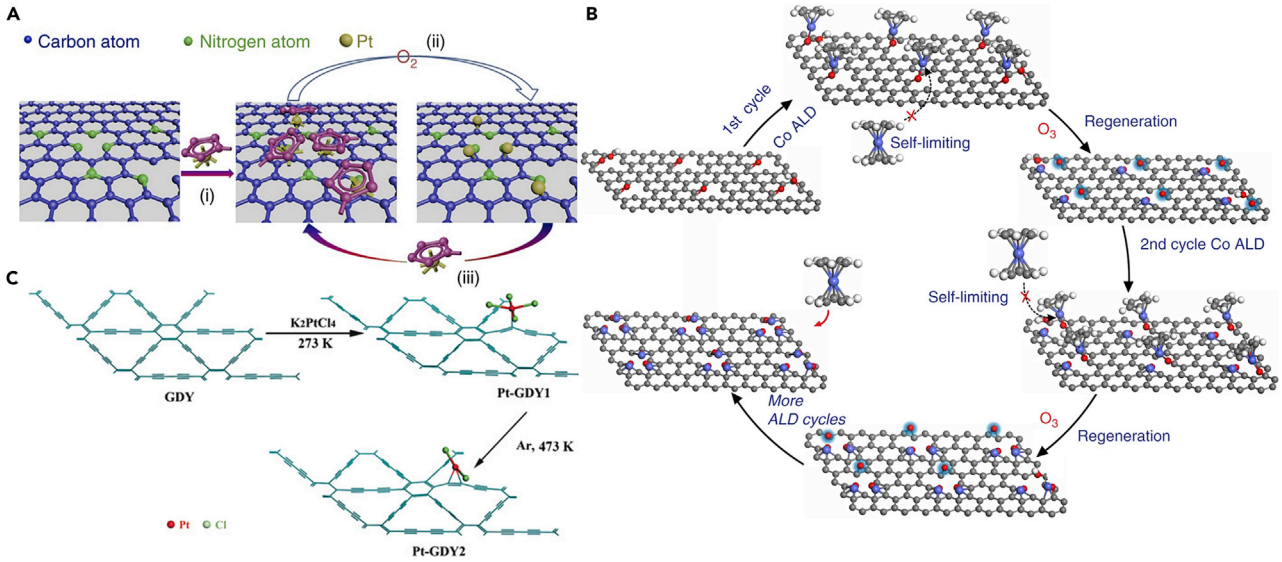

Figure 1. The preparation of SACs by ALD and impregnation methods

(A) Synthetic protocol of the Pt ALD mechanism on NGNs (Cheng et al., 2016).

(B) The fabrication process of Co_1/G SACs with tunable loadings. The gray, white, red, and blue balls represent carbon, hydrogen, oxygen, and cobalt, respectively (Yan et al., 2018b).

(C) The fabrication process of Pt-GDY1 and Pt-GDY2 (Yin et al., 2018).

are numerous individual Pt atoms and very small clusters in the ALD50Pt/NGNs catalysts, whereas some Pt clusters grow into nanoparticles after 100 cycles. Meanwhile, the HER catalytic performance decreased with the increased number of ALD cycles, and ALD Pt/NGN catalysts showed higher catalytic activity and long-term stability in comparison with the commercial Pt/C catalysts in 0.5 M H_2SO_4. What's more, the Pd_1/graphene with Pd-C_2 coordination were prepared by anchoring the palladium hexafluoroacetylacetate ($Pd(hfac)_2$) and formalin at 150°C on a viscous flow reactor (Yan et al., 2015a). The ($Pd(hfac)_2$) was held at 65°C to get a sufficient vapor pressure. Likewise, the 99.999% of purity N_2 act as carrier gas at a flow rate of 200 mL min^{-1}. The manifold was kept at 110°C to avoid precursor condensation. It showed outstanding activity, selectivity, and durability than the Pd-NPs/graphene in selective hydrogenation of 1, 3-butadiene with about 100% butenes selectivity at 95% conversion at about 50°C. ALD can also be used to prepare carbon-based-material-supported nonnoble metal single-atom catalysts. The isolated Co atoms anchored on graphene (Co_1/G) with tunable high metal loading and a six-coordination of Co_1-O_2C_4 were fabricated by ALD (Yan et al., 2018b). The amount of metal loading can be modulated by simply controlling the number of turns of the ALD. As shown in Figure 1B, the first cycle of Co ALD was carried out on thermally reduced graphene oxide by exposing the carrier to $CoCp_2$ vapor. Subsequently, the molecule O_3 is injected into the cavity to remove the ligand. Although the new active site is reconstructed, another batch of Co atoms is loaded in the subsequent ALD cycle. The load density of Co_1/G catalyst was precisely adjusted by controlling the cycles of Co ALD. A series of Co_1/G catalysts with loading capacities of 0.4, 0.8, 1.3, 2.0, and 2.5 wt% were obtained by 1, 2, 3, 4, and 5 ALD cycles, respectively. The Co_1/G SACs exhibited high activity and selectivity for the hydrogenation of nitroarenes to produce azoxy aromatic compounds.

By adjusting the number of cycles, order, and type, ALD can achieve atomically fine control over the structure of catalyst active sites, providing a bottom-up strategy for precise and controllable catalyst synthesis. However, the high cost and low yield are the primary reasons for limiting the industrial application of ALD method.

Impregnation method

Impregnation method, as one of wet-chemical methods, is considered to be the most promising route for mass production due to the low price and easy operation. Impregnation method is widely used in the preparation of supported catalysts, especially low-content noble-metal-supported catalysts. Yin et al. realized

coordination regulation through impregnation method and confirmed better HER performance in low coordination environment (Yin et al., 2018). Pt single-atom supported on graphdiyne (GDY) was prepared by wet-chemical route. The coordination environment is controlled by controlling facile annealing step. React GDY with K_2PtCl_4 aqueous solution at 0°C for 8 h (named as Pt-GDY1) and wash with plenty of water. Then annealing in Ar atmosphere at 200°C for 1 h (named as Pt-GDY2) (Figure 1C). The Pt-GDY2 with four-coordinated C_2-Pt-Cl_2 exhibits higher mass activity up to 3.3 times than Pt-GDY1 with five-coordinated C_1-Pt-Cl_4. Higher total unoccupied density of states of Pt 5d orbital and close to zero $|\Delta G^{Pt}_{H^*}|$ value makes Pt have higher HER catalytic activity. Hetero-atom doping modification of the carrier affects the coordination environment. For example, atomically dispersed electrocatalysts (ADCs) with Ru-C_5 single atoms and Ru-O_4 nanoclusters were fabricated in S-doped carbon black by using impregnation strategy in room temperature (Cao et al., 2021). Activated carbon and 2, 2-bithiophene were grinded fully and then calcined in a tube furnace at 800°C for 2 h under N_2 atmosphere to obtain the S-doped carbon material. Thirty milligrams of S-doped carbon material and 20 mL water were mixed intensively in a beaker; 0.05 mmol $RuCl_3 \cdot xH_2O$ dissolved in 5 mL deionized water was dropped into the above solution and stirred for another 6 h. Then, the mixture was centrifuged and dried in a vacuum drying oven at room temperature to obtain the atomically dispersed Ru catalyst. Meanwhile, dual-site Ir, Rh, Pt, Au, and Mo ADCs can also be prepared by this method. The Ru ADCs show enhanced HER performance in alkaline solution due to the synergic effect between single-atoms and sub-nanoclusters. What's more, Cu-SA/SNC with low-valence Cu(+1)-N_4-C_8S_2 was constructed by impregnation method with single copper atoms embedded in a sulfur and nitrogen-modified carbon support (Jiang et al., 2019). $Na_2S \cdot 9H_2O$ and S powder were dissolved in deionized water by ultrasonic dissolving for 5 h at ambient conditions. Then, the solution was heated at 80°C for 12 h in a Teflon autoclave to obtain S precursor. CuPc, DCDA, and trimesic acid were dissolved in deionized water. Then S precursor was dropped into the above solution for continuously stirring and drying at 80°C. Next, the mixture was annealed at 900°C for 2 h under N_2 atmosphere, and the samples were leached in 0.5 M H_2SO_4 solution at 80°C for 24 h to remove the free-standing metallic residues. Synthesizing single atom catalysts by the impregnation method is simple, without complicated and expensive equipment (Sun et al., 2020). Therefore, this method is very suitable for large-scale synthesis of single-atom catalysts. Yang et al. successfully synthesized a series of M-SACS catalysts (M = Ni, Mn, Fe, Co, Cr, Cu, Zn, Ru, Pt, and their combinations) by complexing a series of metal cations with 1, 10-phenantholine and loading them on commercial carbon black (Yang et al., 2019a). The synthetic approach enables large-scale (>1 kg) production of single-atom catalysts with high metal loadings. The synthesized Ni single-atom catalyst exhibits excellent activity in the electrochemical reduction of carbon dioxide to carbon monoxide. It provides an important approach for large-scale preparation of SACs by impregnation method.

Electrochemical deposition method

Electrochemical methods were regarded as the effective strategies to synthesize high-purity SACs because of low cost and simple applicability. The standard three-electrode system can quickly prepare the target sample and accurately control the catalyst preparation process by adjusting the workstation parameters, which has obvious advantages over the traditional wet chemical method.

Atomic dispersed Ru-doped ultrathin $Co(OH)_2$ nanosheet arrays (CoRu@NF) was fabricated by electrochemical deposition method (Zhu et al., 2021; Figure 2A), which shows excellent catalytic performance of OER in 1.0 M KOH and 0.1 M KOH solution. A standard three-electrode system was carried out for electrochemical deposition. The nickel foam (NF) was immersed 2 cm below the liquid surface; saturated calomel electrode (SCE) and the carbon rod were used as the working electrode, reference electrode, and counter electrode. $Co(NO_3)_2 \bullet 6H_2O$ aqueous solution was poured into a 100 mL electrolytic cell. Cyclic voltammetry with the scanning potential of $0 \sim -1.2$ V (versus SCE), the scanning rate of 100 mV s^{-1}, and the scanning cycles of 40 times was used. The introduction of Ru reduces the thickness of the nanosheets, exposing more active sites. Besides, single-atoms Ru were anchored on the surface of MoS_2 nanosheets array supported by a carbon cloth with 3D porous structure based on theoretical predictions (Wang et al., 2019; Figure 2B). The MoS_2/CC acts as the working electrode. Atomically Ru was electrodeposited by cycling MoS_2/CC substrate from −0.5 to 0.4 V versus SCE at the sweep rate of 20 mV s^{-1} in the electrolyte containing $RuCl_3$ and H_2SO_4 for 20 cycles. Finally, the Ru-MoS_2/CC was taken out, washed with deionized water and dried by nitrogen flow. The catalyst displays HER catalytic performance comparable to commercial Pt/C under pH-universal conditions. What's more, Zeng's group reported the fabrication of SACs by electrochemical deposition method in a wide range of metals and supports (Zhang et al., 2020). The cathodic voltage was from 0.10 to −0.40 V, the anodic voltage was from 1.10 to 1.80 V, and the scanning

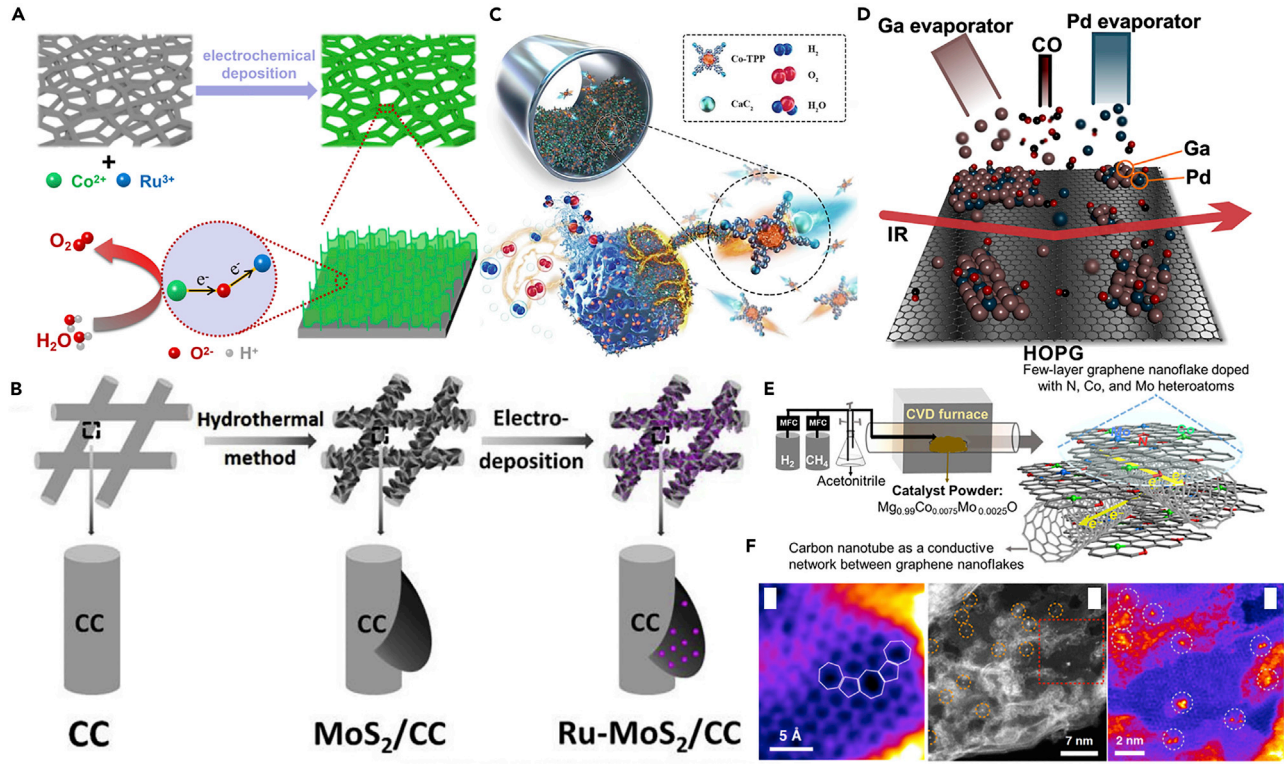

Figure 2. Synthesis illustrations of electrochemical deposition strategy, ball milling method, and chemical vapor deposition

(A) Synthetic protocol of the electrodeposition preparation of CoRu@NF and OER catalysis principle (Zhu et al., 2021).

(B) Synthetic protocol for Ru-MoS_2/CC array-catalyst (Wang et al., 2019).

(C) The fabrication process of Co-BM-C (Jin et al., 2021b).

(D) Scheme of Pd-Ga model SCALMS studied in this work (Kettner et al., 2019).

(E) Schematic representation of the N–Co–Mo–GC/CNT and Co–Mo–GC/CNT materials.

(F) STEM images (Tavakkoli et al., 2020).

rate was 5 mV s^{-1}. The processes were repeated for 10 times and 3 times in cathodic and anodic deposition, respectively. The experimental results showed that SACs displayed different electronic states due to different redox reactions between the cathodes and the anodes. More than 30 different SACs can be successfully fabricated from cathodic or anodic deposition only by varying different metal precursors and supports. Interestingly, the SACs deposited by cathode have higher activity for hydrogen evolution reaction, whereas the SACs deposited by anode have higher activity for oxygen evolution reaction.

In general, the species and coordination environment of SACs can be changed by varying the supports and metal precursors. However, there are still few studies on the preparation of single atoms on carbon-based materials by electrodeposition due to the influence of electrodeposition equipment.

Chemical vapor deposition

As a kind of "top-down" method, CVD is often used to synthesize single-atom catalysts. The research of CVD began in the late nineteenth century. Its principle is to introduce the reaction agent vapor and other gases required into the reaction chamber, by increasing the temperature, or other forms of energy, so that they have chemical reactions on the substrate surface to generate new solid substances deposited on the surface (Drosos and Vernardou, 2018; Zhang et al., 2019).

The CVD method consists of the following four steps: (1) The reaction gas diffuses to the surface of the material; (2) the reaction gas is adsorbed on the surface of the material; (3) the chemical reaction occurs on the surface of the material; (4) the gaseous by-products are separated from the surface of the material. Due to the nucleation or growth at the molecular level, CVD is more suitable for the formation of dense and uniform thin films on the surface of irregularly shaped substrates, and the deposition speed is fast and the

quality of the film is very stable (Gardecka et al., 2018). Some special films also have excellent optical, thermal, and electrical properties and thus easy to achieve mass production (Liu et al., 2019b). For example, Miroslav and colleagues (Kettner et al., 2019) synthesized Pd-Ga alloy supported on highly ordered pyrolytic graphite (HOPG) by vapor deposition under ultra-high vacuum, which is shown in Figure 2D. Pd was deposited using a commercial electron beam evaporator from a Pd wire onto the HOPG substrate that was kept at room temperature, and Gallium was evaporated from a pyrolytic boron nitride crucible in a second electron beam evaporator at an angle of approximately 45° with respect to the sample normal. The evaporation rates were 1.5 Å/min for Pd and 0.5 Å/min for Ga, respectively. Through STM/AFM characterization results, it can be seen that the HOPG-rich Pd-Ga alloy was prepared on HOPG. The Pd-Ga alloys of Ga exhibit superior Pd single-atom site properties and excellent stability. In addition, Mohammad and his team (Tavakkoli et al., 2020) successfully synthesized N, Co, and Mo single-atom-decorated highly graphitized graphene nanoflake-carbon tube (CNT) composites by a one-step reactive vapor deposition method. As shown in Figure 2E, the method first obtains the CoMo mixed catalyst by heating and calcination. Then, acetonitrile was added in the mixed atmosphere of H_2/CH_4 for N doping, and the carbon material was grown on the catalyst at 1000°C. A high specific surface area mesoporous material obtained by this method is favorable for the oxygen mass transfer process and exhibits high catalytic activity and stability (basic conditions) for OER and ORR. Through STEM images, single metal atoms can be clearly identified in the multilayer graphite films, as shown in Figure 2F. However, the deposition temperature of CVD is usually very high, generally between 900°C and 2000°C, so it is usually used on carbon materials. However, high temperature can easily cause great damage to common materials, such as nickel foam, which limits the choice of substrates and deposition layers. At present, two aspects of medium, low temperature and high vacuum, are the main development directions of CVD (Malarde et al., 2017).

Ball milling method

Ball milling can cut and reconstruct the chemical bonds of materials/molecules and is widely used in the preparation of carbon-based-material-supported single atoms. Moving balls with kinetic energy apply their energy to the materials, causing a single metal atom to be embedded on the surface of the carbon substrate (Yang et al., 2020b). A series of graphene-embedded FeN_4 (FeN_4/GN) catalysts with different Fe content were prepared via high-energy ball milling (Deng et al., 2015). Firstly, 2.0 g graphite flake and 60 g steel balls were placed in a hardened steel cylinder in a glove box, cleaned with high-purity argon for 20 min, and sealed. Various ratios of 2.0 g FePc and GN composites and 60 g steel balls (1–1.3 cm in diameter) were operated like before. Ball milling was agitated with 450 rpm for 20 h. A series of FeN_4/GN samples with different Fe content were obtained. Coincidentally, single Fe atoms anchored on graphene nanosheets (FeN_4/GNs) were fabricated by ball milling method for the direct conversion of methane to C_1 oxygenated products at room temperature (Cui et al., 2018). Other transition metals were also prepared by this method, including Mn, Fe, Co, Ni, and Cu. A series of M-N_4-coordinated SACs were obtained by simply regulating the type of metal precursor salt. Fe and/or Co atomically dispersed within the 2D conjugated aromatic networks (CAN) were synthesized with the assistance of ball milling (Yang et al., 2019b). Firstly, PMDA, urea, NH_4Cl, $(NH_4)_6Mo_7O_{24}\cdot 4H_2O$, and a certain amount of metal chloride ($FeCl_3$ and $CoCl_2\cdot 6H_2O$) were mixed in a crucible. The metal polyphthalocyanine weas prepared by heating the mixture in a muffle furnace at 220°C for 3 h; 0.2 g above polyphthalocyanine and 15 mL deionized water were transferred into a zirconium dioxide capsule containing zirconium dioxide balls (0.5 mm in diameter). Ball milling was carried out at 1000 rpm for 1 h. The single-metal-atom-site density up to 10.7 wt% without agglomeration. CAN-Pc (Fe/Co) with Fe-N_4 and Co-N_4 coordination displays superior performance to benchmark Pt/C for ORR and Zn-air batteries. In one study, a rapid one-step mechanochemically induced self-sustaining reaction was proposed (Jin et al., 2021b). Nitrogen-doped-carbon-supported single Co atoms were prepared by direct ball milling of cobalt (II) 5,10,15,20-tetrakis-(4′-bromophenyl) porphyrin (Co-TPP-Br) and calcium carbide without the pretreatment of carbon support and further pyrolysis procedure (Figure 2C). The mechanochemical energy can ignite and propagate a self-sustaining exothermic process, leading to the direct formation of carbon matrix to stabilize metal sites. The sample Co-BM-C with CoN_4 configuration prepared by ball milling (BM) showed excellent HER (η_{10} = 126 mV) and OER (η_{10} = 240 mV) performance in 1.0 M KOH, showing great potential in overall water splitting (1.60 V @ 10 mA cm^{-2}).

Pyrolysis strategy

The pyrolysis strategy shows the merits of low price, environmental friendliness, and simplification in the synthesis procedures. The different types of metal atoms can be controlled by modulating the parameters

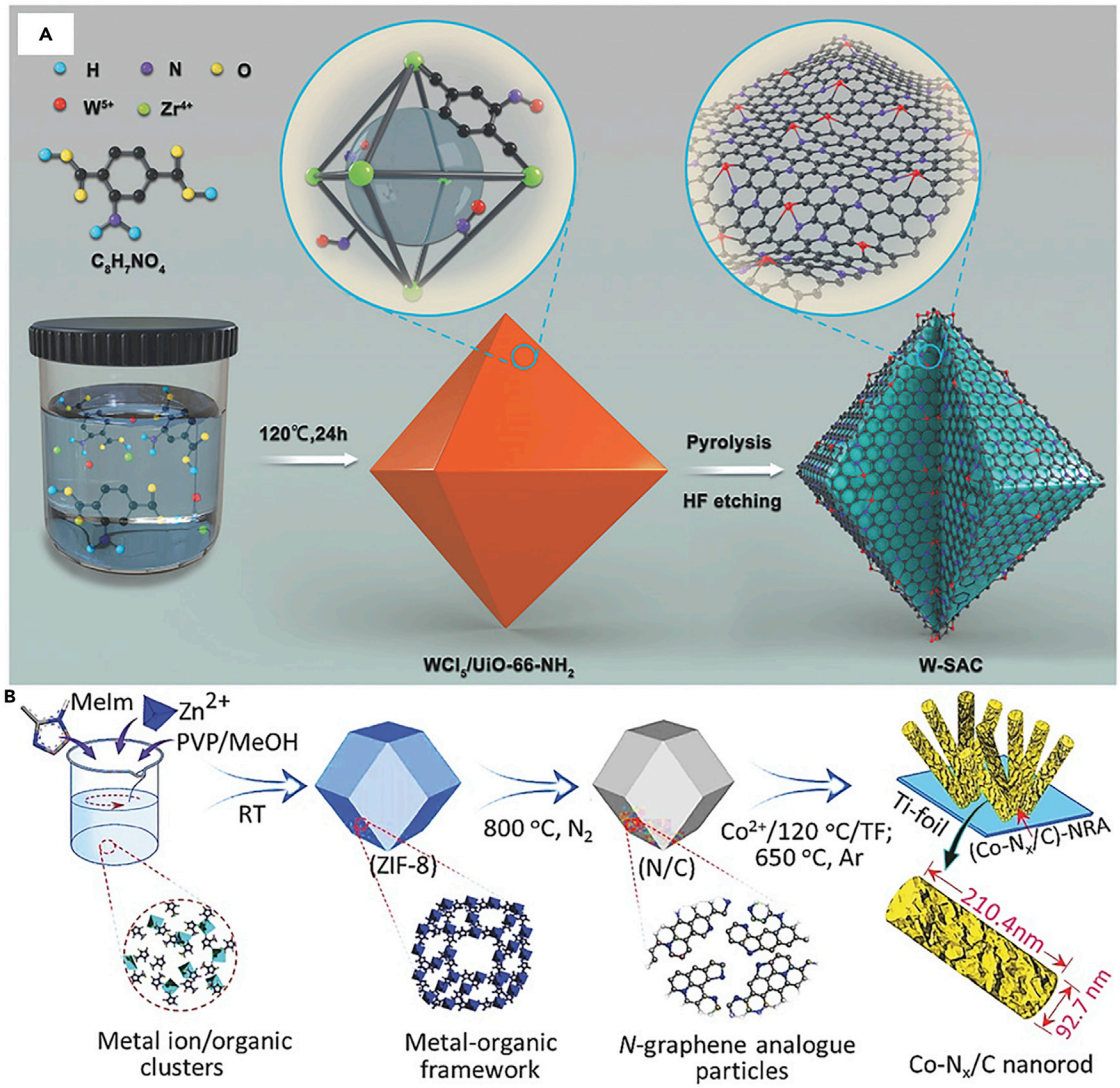

Figure 3. The preparation of SACs by pyrolysis strategy

(A) Scheme of the formation of W-SAC (Chen et al., 2018a).

(B) Schematic illustration of the structural transition of Co-N_x/C nanorod array (Amiinu et al., 2018).

in the synthesis process. Metal nodes in metal-organic framework (MOFs) are known to be atomically dispersed and have a well-coordinated environment, making them ideal precursor types for building SACs (Wang et al., 2018a). The single tungsten atoms supported on MOF-derived N-doped carbon matrix was achieved successfully for HER applications (Chen et al., 2018a). The W-SAC and MOF were prepared by pyrolysis strategy. Tungsten precursor (WCl_5) was encapsulated in the skeleton of MOF (UiO-66-NH_2) and then pyrolyzed at 950°C (Figure 3A). The excess zirconia is removed by hydrofluoric acid solution to obtain W-SAC. It is important to note that the uncoordinated amines in UIO-66-NH_2 play an important role in preventing the aggregation of W species. The catalyst displays 85 mV at a current density of 10 mA cm^{-2} in 0.1 M KOH, where HER catalytic performance is close to that of commercial Pt/C. In addition, zeolitic-imidazolate frameworks (ZIFs) also are often used to design templates and precursor for single-atom catalysts due to its flexibility and ultrahigh surface area (Xia et al., 2015, 2016). ZIFs can be converted into amorphous or graphite-carbon frames by pyrolysis synthesis, thus providing a rich platform for the design of functional custom materials for electrocatalytic applications (Tang et al., 2015; You et al., 2015; Zheng et al., 2014). Co–N_x/C nanorod array derived from 3D ZIF nanocrystals was prepared through Zn^{2+} clusters that react with methylimidazole/PVP ligand to form ZIF nanocrystals, which catalyze the structural evolution of nanorods

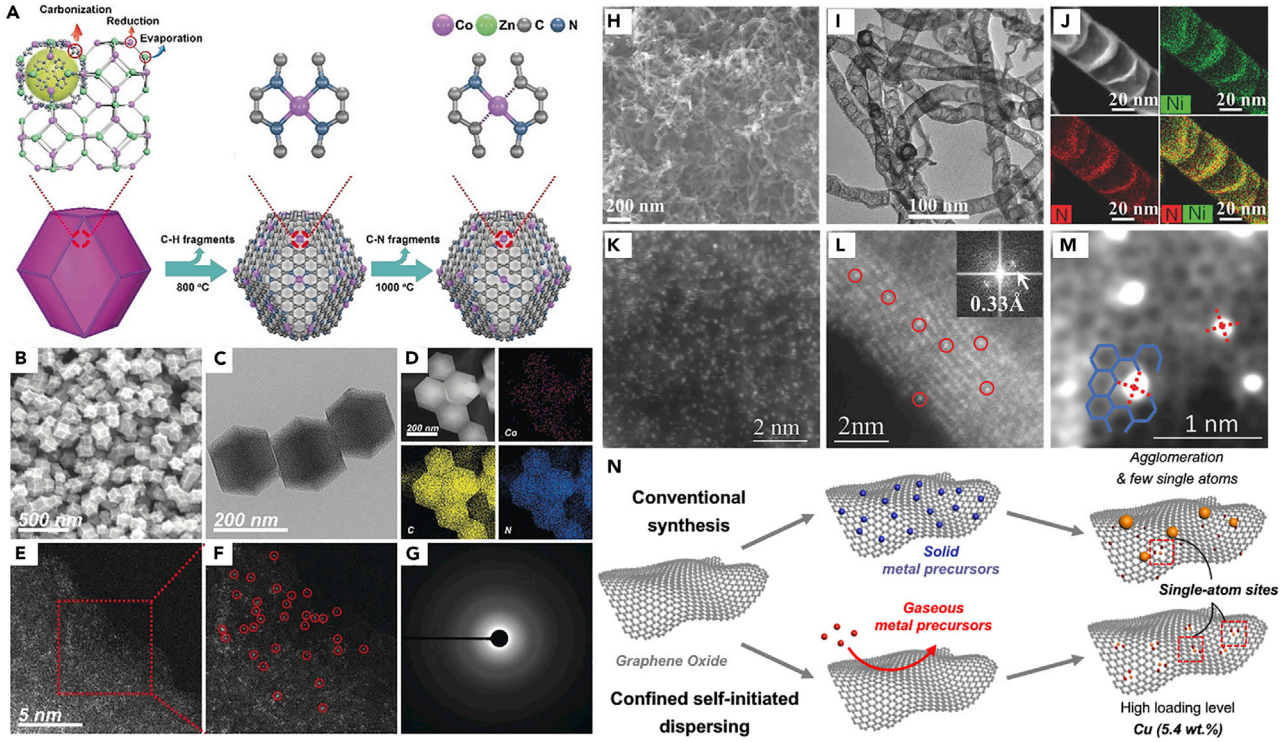

Figure 4. Coordination environment regulation of SACs

(A–D) The synthetic protocol of Co-N_4 and Co-N_2. Images of (B) SEM, (C) TEM, and (D) the corresponding EDS mapping of Co-N_2.

(E and F) Magnified HAADF-STEM images of Co-N_2.

(G–K) Corresponding SAED pattern of Co-N_2 (Wang et al., 2018b). The images of (H) SEM, (I) TEM, (J) STEM-EDS mapping, and (K) AC-STEM-annular dark-field (ADF) of NiSA-N-CNTs.

(L) ADF image showed the Ni single atoms anchored on the walls of a CNT. Inset: the image of Fourier transform (Cheng et al., 2018).

(M) ADF images showed coordination environment of Ni single atoms.

(N) The protocols for the synthesis of (upper) conventional and (lower) confined self-initiated dispersing formation process of metals dispersed on graphene (Han et al., 2019a).

(Amiinu et al., 2018) (Figure 3B). Due to the synergistic effect of the chemical composition and abundant active sites of the nanorods, the catalysts show excellent ORR and OER performance compared with commercial Pt/C and IrO_2.

In order to achieve coordination regulation, Wang and colleagues prepared a series of single-Co-atoms catalysts with different nitrogen coordination numbers and studied their catalytic performance for CO_2 reduction (Wang et al., 2018b). Co/Zn ZIFs were synthesized at room temperature firstly, and then Zn would be evaporated away during the pyrolysis process. The Co ions would be reduced to single Co atoms anchored on nitrogen-doped porous carbon. SACs with coordination number from 2 to 4 were prepared by controlling volatile C-N fragments to adjust the number of N around central Co site through bimetallic Co/Zn ZIFs at 1000°C, 900°C, and 800°C of pyrolysis temperatures, respectively (Figure 4A). Co nanoparticles were also prepared by pyrolysis of ZIFs containing pure Co. As can be seen from Figure 4B and C, the Co-N_2 catalyst maintained the initial ZIF morphology. EDX spectrum indicates that Co atoms are uniformly distributed throughout the structure (Figure 4D). Meanwhile, atomically dispersed Co atoms can be directly observed from AC-HAADF-STEM (Figures 4E and 4F). What's more, SAED with ring pattern indicates that the crystallinity of Co-N_2 catalyst is poor (Figure 4G). The optimum selectivity and activity are shown when Co is coordinated with two N atoms with 94% CO formation Faradaic efficiency and a current density of 18.1 mA cm^{-2} at an overpotential of 520 mV. Meanwhile, the turnover frequency (TOF) value of the CO formation is up to 18200 h^{-1}. The results of experiments and theoretical calculations show that Co-N_2 sites can promote the formation of CO_2 into CO_2^- intermediates, thus enhancing the CO_2RR performance. Moreover, improving the loading of SACs is another factor to promote the industrial application of single atom catalysis. Atomically dispersed transition metals anchored on nitrogen-doped carbon

nanotubes (MSA-N-CNTs, where M = Ni, Co, NiCo, CoFe, and NiPt) with high loading were fabricated through a multi-step pyrolysis strategy (Cheng et al., 2018). Take the NiSA-N-CNTs for example, $Ni(acac)_2$ was dispersed with dicyandiamide $C_2H_8N_2$ in 100 mL solution and stirred for 10 h, followed by drying and grinding. Subsequently, the mixture was heated at 350°C and 650°C for 3 h under Ar atmosphere, respectively. Finally, the as-prepared yellow powder was heated in a selected temperature range of 700–900°C to obtain the target production. From the SEM and TEM image, it can be observed that the average CNT diameter is around 31 nm without metallic nanoparticles (Figure 4H and 4I). Meanwhile, the uniform distribution of N and Ni can be seen from STEM-EDS mapping (Figure 4J). In AC-STEM, bright spots corresponding to Ni atoms were uniformly distributed in CNTs, and individual Ni atoms were located on the walls of a CNT (Figure 4K and 4L). In addition to normal C_6 carbon rings, C_5, C_7, and other nonC_6 carbon rings were also formed in CNT, combining with the results of Raman spectroscopy (Figure 4M). NiSA-N-CNTs with a load of up to 20 wt% showed the best selectivity and activity for the electrochemical reduction of CO_2 to CO, with TOF values two orders of magnitude higher than those of Ni nanoparticles loaded on CNTs. Han and colleagues reported the single Cu atoms dispersed on graphene through a unique confined self-initiated dispersing protocol (Han et al., 2019a). The GO/DICY was prepared by stirring dicyandiamide (DICY) graphene oxide dispersion and then freeze-drying. Then the mixture was added into a quartz boat that was tightly wrapped by a piece of Cu foil. The quartz boat was pyrolyzed at 600°C for 2 h and 800°C for 1 h under Ar atmosphere in a tube furnace. The production was treated with 0.5 M H_2SO_4 and then pyrolyzed at 300°C again. This novel *in situ* dispersion protocol produces highly reactive gaseous copper-containing intermediates that essentially circumvent the large-scale agglomeration of metal atoms in traditional processes and facilitate Cu dispersion on graphene (Figure 4N). The catalyst with the loading of 5.4 wt% showed an outstanding performance for ORR due to the abundant and highly dispersive Cu single atoms. Zhao and colleagues prepared a series of M−NC (M = Mn, Fe, Co, Ni, Cu, Mo, Pt, etc.) SACs with metal loadings up to 12.1 wt% through a cascade anchoring strategy (Zhao et al., 2019). Firstly, the metal ions are chelated by chelating agent and anchored onto oxygen-species rich porous carbon support. Then the complex bound carbon and melamine were put into a tube furnace and heated to 800°C for 2 h under Ar flow to obtain the M-NC. Furthermore, the scale-up synthesis can be achieved in parallel by the same synthesis route except for increasing the amounts of materials.

In general, the precise and controllable preparation of SACs can be achieved by ALD, however, its expensive equipment and low yield limited the development of this technology. From a practical point of view, wet-chemistry synthetic methods for SACs are more desirable approaches because of its ease of operation and feasibility of large-scale manufacturing. From the methods introduced earlier, it can be seen that both impregnation method and pyrolysis method can be used to achieve the scale-up preparation of carbon-based-material-supported SACs. In particular, the impregnation method does not require complex and expensive equipment and displays the characteristics of low cost, simple operation, and easy synthesis, so it shows great potential in mass preparation.

CHARACTERIZATION TECHNIQUES FOR SACS

The research progress of SACs is closely related to the development of characterization technology. Advanced characterization techniques help to understand the coordination environments and electronic structures of SACs, which directly affect the catalytic performance. Hitherto, the main applied characterization methods included high-angle annular dark-field scanning transmission electron microscopy (HAADF-STEM), atomic force microscope (AFM), scanning tunneling microscopy (STM), X-ray absorption spectroscopy (XAS), and Raman measurements. Furthermore, *in situ* characterization has also been introduced as a powerful tool for studying the real active sites, structural changes during the catalysis process, and reaction mechanisms of SACs. Thus, in order to fully understand the structure, composition, and coordination environment of SACs, it is necessary to combine a variety of advanced characterization methods. In addition, density functional theory (DFT) simulation provides an unprecedented opportunity to discover catalytic reaction mechanisms, enabling the rational design of materials with personalized activity.

High-angle annular dark-field scanning transmission electron microscopy

Nowadays, transmission electron microscopy (TEM) is a powerful tool to obtain the fine structure of nanomaterials. From the Figure 5A (Ren et al., 2020), we can see that the received signals are mainly transmitted electron beam and scattered electron in the range of θ_3. In the range of θ_2, Bragg scattered electrons are signals. When the received signal is θ_1, the HAADF image can be obtained. Especially, supported single atoms can be directly observed through aberration-corrected HAADF-STEM, and even the atomic

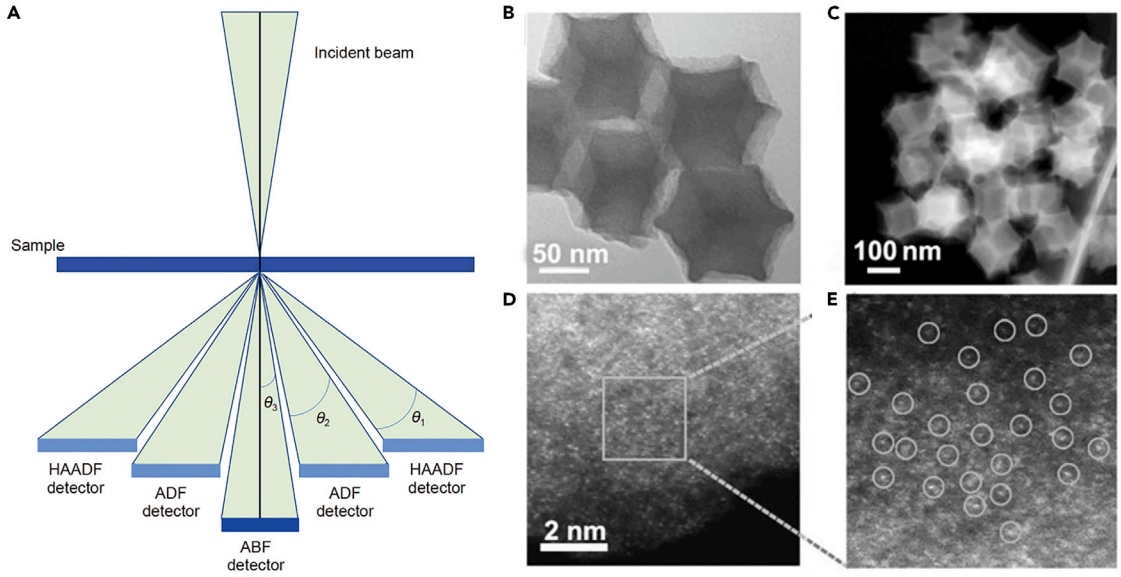

Figure 5. HAADF-STEM characterization

(A) STEM detector distribution diagram (Ren et al., 2020).

(B and C) TEM and (C) HAADF-STEM images of Co SAs/N-C (800).

(D and E) Magnified HAADF-STEM images of Co SAs/N-C (800) (Yin et al., 2016).

structure information could be obtained. The phase contrast of atoms is directly proportional to their relative atomic number Z. Because the Z value of an isolated atom is different from that of the host atom, the relative bright dots of single metal atoms can be observed clearly. Therefore, theoretically speaking, the higher the Z value of the atom on the hosts, the better the image will be. For example, the as-prepared Co SAs/N-C structure shows rhombododecahedral shape (Yin et al., 2016), as revealed by TEM and HAADF-STEM (Figures 5B and 5C). The aberration-corrected HAADF-STEM (Figures 5D and 5E) were carried out to elucidate the form of the Co atoms with sub-angstrom resolution. Due to the different Z contrast between Co and C, the isolated heavier Co SACs can be identified in the carbon support.

Atomic force microscope and scanning tunneling microscopy

The STM is a scanning probe microscopy tool that enables the observation and localization of individual atoms with a higher resolution than its atomic force microscope counterparts. The atomic-level sharp metal tip in STM scans the surface atomic structure based on the electron quantum tunneling effect of the tip-sample nano-gap. The effect causes the tunnel current to show an exponential relationship with the size of the gap, and an atomic-level sample surface topography characteristic image is obtained. It is commonly used in surface scientific research to examine model catalysts, such as single crystals with well-defined surface structures. What's more, the STM can directly observe whether the surface atoms of the material have periodic surface structure features, surface reconstruction, and structural defects. However, STM cannot detect deep information and observe insulators. Atomically dispersed platinum (Pt) was synthesized by photochemical reduction method (Wei et al., 2017). The atomically dispersed Pt on ultrathin carbon films can be directly observed through STM (Figure 6A). At atomic resolution, single Pt atoms appear as single-peak protrusions with a diameter of about 0.2 nm and a height of about 0.3 nm. Besides, Wu and colleagues synthesized high-density Cu(I)-N active sites in an N-doped graphene matrix via pyrolysis of copper phthalocyanine and dicyandiamide (Wu et al., 2016). HAADF-STEM and the corresponding element mappings show the uniform distribution of Cu, N, and C (Figure 6B). From atomic resolution STM image (Figure 6C), the obvious bright spots can be observed, which indicates that the Cu atoms are atomically dispersed. STM simulations further revealed the atomic structure of this catalyst, in which atomically dispersed Cu-N_2 centers are embedded in the graphene lattice (Figure 6D).

AFM can not only measure the surface morphology of the sample (close to the atomic resolution) but also detect the force between the atoms on the surface, the elasticity, plasticity, hardness, adhesion, friction, and so on. From topographic image, the height of the nanoparticle or the surface roughness of the sample

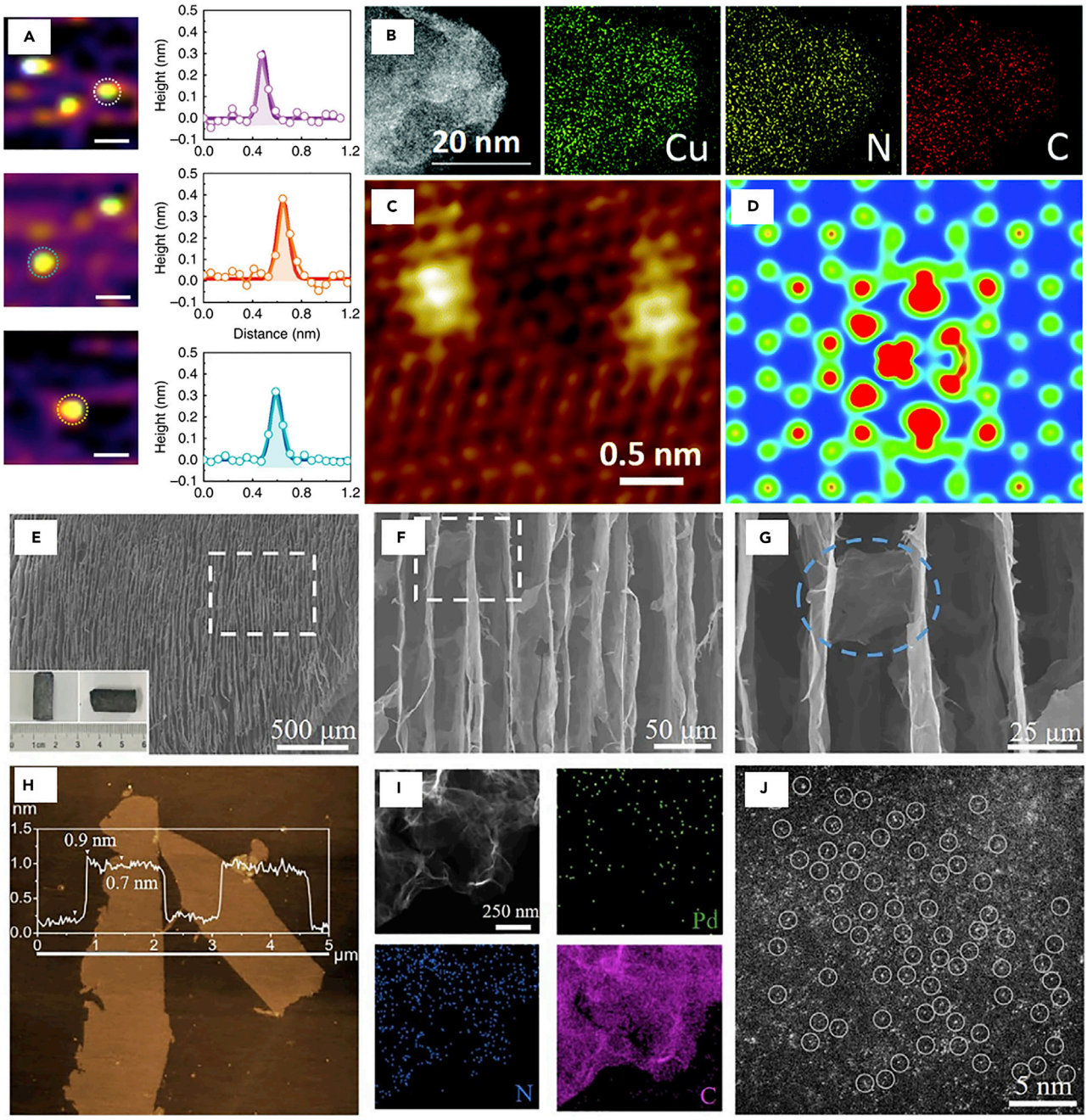

Figure 6. STM and AFM characterizations

(A) Typical STM images of Pt single atoms dispersed on ultrathin carbon films (Wei et al., 2017).

(B) HAADF-STEM image and the corresponding EDS mappings for the Cu, N, and C atoms.

(C) STM and (D) STM simulation images (Wu et al., 2016).

(E–G) SEM images of Pd_1/C_3N_4/rGO with different magnifications. Insets of (E) are the photographic images of the 3D Pd_1/C_3N_4/rGO monolith catalyst.

(H) AFM image of GO substrate.

(I) EDS elemental mapping.

(J) High-resolution HAADF-STEM image of Pd_1/C_3N_4/rGO (Fu et al., 2020).

can be seen clearly. Reduced graphene oxide (rGO) has stable anchor sites for metal single atoms, but the anchor sites are sparse, making it difficult to prepare high-load metal single-atom catalysts. Therefore, combining rGO with two-dimensional materials with abundant connecting atoms, such as carbon nitride,

is an effective strategy to deal with this challenge. Therefore, metal single atoms (Pd, Pt, Ru, Au) were fabricated on porous carbon nitride/reduced graphene oxide (C_3N_4/rGO) foam (Fu et al., 2020). Among these catalysts, Pd_1/C_3N_4/rGO showed enhanced catalytic activity over its NPs counterpart for Suzuki-Miyaura reaction. From the Figures 6E–6G, the C_3N_4/rGO layer with an onion-like microstructure with orderly organization can be observed. The thickness of GO sheet building blocks was measured by AFM (Figure 6H). The sheet height of about 0.7 nm corresponds to the height of a single GO layer. Meanwhile, the AC-HAADF-STEM was applied to observe the samples (Figure 6J). It can be seen from the element mapping diagram (Figure 6I) that Pd element is evenly distributed in the matrix containing N and C. As shown in isolated single Pd atoms, sites can be seen clearly on the 2D C_3N_4/rGO sheet without aggregated Pd nanoparticles or clusters.

X-Ray absorption spectroscopy

XAS is an element-specific technique used to obtain the properties of absorbing atoms and their surroundings, resulting in a comprehensive understanding of the chemical state and structure of catalysts. It is the main technique used to characterize different coordination structures, which can be used to gain insight into the local atomic and electronic structure of single atoms. XAS includes X-ray absorption near edge structure (XANES) spectrum and extended X-ray absorption fine structure (EXAFS) spectrum. The energy of XANES spectrum ranges from the absorption edge to 30–50 eV above the absorption edge, and it is sensitive to the charge state and orbital occupancy of single metal atoms. The EXAFS spectrum represents the spectral region where the energy above absorption edge ranges from 30–50 eV to 1000 eV or more. Through Fourier transform (FT) analysis of EXAFS, the coordination number and distance between the central atom and adjacent atoms can be extracted. Wavelet transform can distinguish backscattered atoms and provide strong resolution in *k* and R space, which is the perfect complement to FT. Single Cu atoms coordinated with both S and N atoms in MOF-derived hierarchically porous carbon (S-Cu-ISA/SNC) was reported by atomic interface regulation (Shang et al., 2020). To better analyze the chemical state and atomic structure of the sample, synchrotron-radiation-based soft XANES and XAFS was carried out. From the analysis of Cu L-edge spectrum (Figure 7A), carbon K-edge spectrum (Figure 7B), N K-edge spectrum (Figure 7C), S L-edge, and K-edge spectra of S-Cu-ISA/SNC combining the XPS results, bonds between atoms can be obtained. Meanwhile, the interface structure at atomic scale, like the average oxidation state of Cu, can be obtained from Cu K-edge XANES spectra of S-Cu-ISA/SNC and the references (Cu foil, CuS, and CuPc) (Figure 7D). The scattering of Cu-N and Cu-S was detected by FT peaks in FT-EXAFS spectra for S-Cu-ISA/SNC, and no Cu-Cu bond was found (Figures 7E and 7G). Cu K-edge wavelet transform (WT)-EXAFS has also been applied to study the atomic configuration and the Cu-N and Cu-S contributions of S-Cu-ISA/SNC due to the strong resolution of k and R spaces (Figure 7F). These results strongly prove the existence of Cu single atoms. Based on the above analysis, the first coordination number of the central copper atom is 4, including one metal-sulfur and three metal-nitrogen bonds, in which bond lengths corresponds to 2.32 and 1.98 Å, respectively (Figure 7H).

Raman spectroscopy

Raman spectroscopy is a nondestructive analysis technique based on the interaction of light and chemical bonds in materials. It can provide detailed information about the chemical structure, phase and morphology, crystallinity, and molecular interaction of the samples. A Raman spectrum is usually composed of a certain number of Raman peaks. Each Raman peak represents the wavelength position and intensity of the corresponding Raman scattered light. Every peak corresponds to a specific molecular bond vibration, which includes not only a single chemical bond, such as C-C, C=C, N-O, and C-H, but also the vibration of a group composed of several chemical bonds, such as the benzene ring breath vibration, long polymer chain vibration, and lattice vibration. Raman measurements are used to further analyze the structural information of SACs. Raman spectra also show the D band and G band, which can be distinguished allotropes of carbon in carbon materials. The D band represents the disordered carbon atoms and sp^2-hybridized carbon atoms (Li et al., 2012, 2018; Pan et al., 2013; Zhang et al., 2017b), whereas G band is related to the tangential stretching mode of sp^2 carbon atoms, indicating the existence of crystalline carbon in the carbon material (Deng et al., 2017). Wei and colleagues prepared N-decorated carbon-encapsulated W_2C/WP heterostructure as an efficient HER electrocatalyst in acid and alkaline solutions (Wei et al., 2021b). The samples prepared with different precursors of $(NH_4)_{10}H_2(W_2O_7)_6/NH_4H_2PO_4$, 1:0, 1:1, 1:2, 1:4, and 1:12, were labeled as W_2C/W@NC, W_2C/WP@NC-1, W_2C/WP@NC-2, W_2C/WP@NC-4, and WP@NC. The two main peaks located at 697 and 803 cm^{-1} in the Raman spectrum correspond to the stretching vibration of W-C (Figure 8A). The I_D/I_G ratios value of W_2C/WP@NC-2 is 0.96 (Figure 8C),

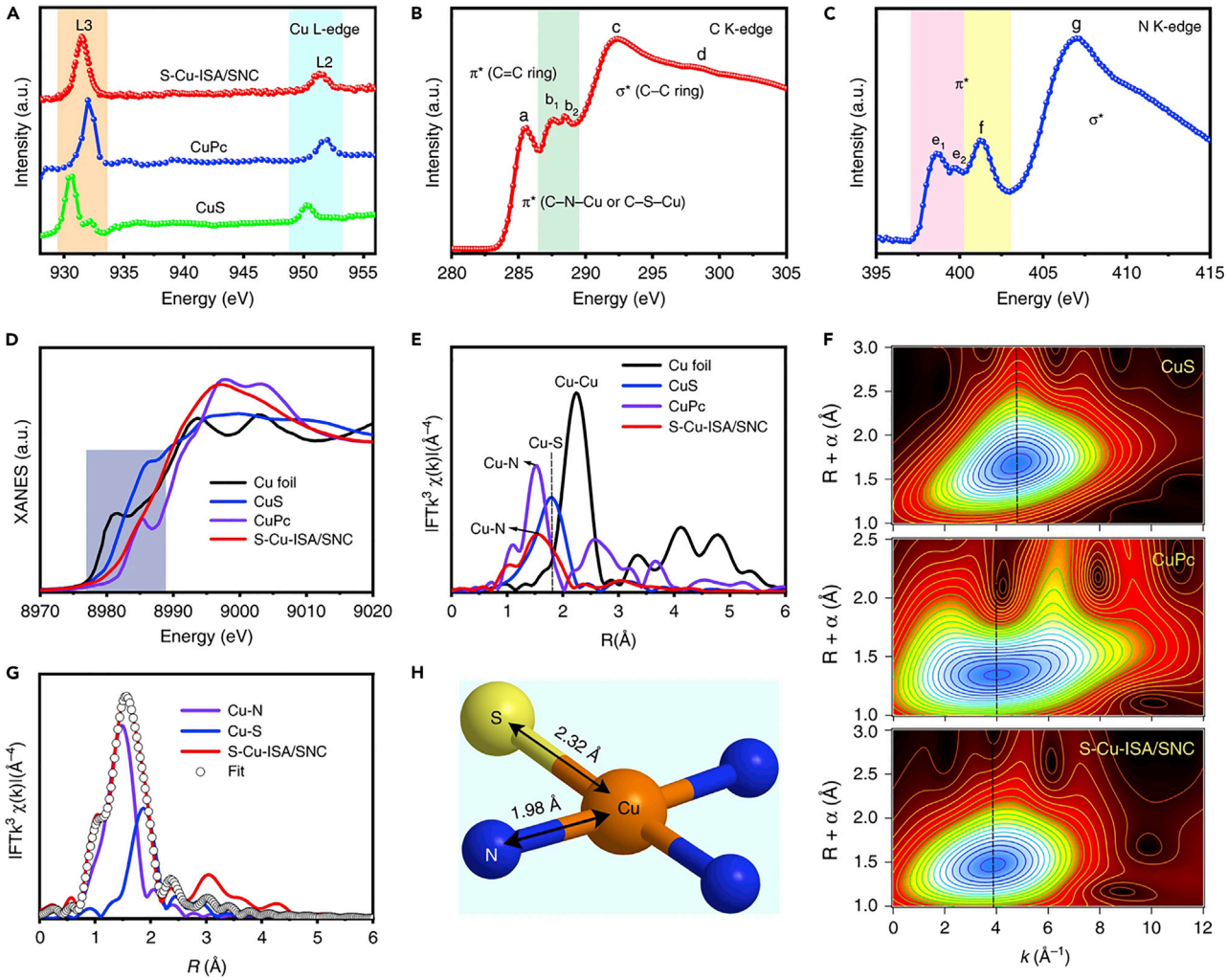

Figure 7. Characterization results of XAS

(A) Cu L-edge XANES spectra of S-Cu-ISA/SNC, CuS, and CuPc.

(B and C) C K-edge (B) and N K-edge (C) XANES spectra of the S-Cu-ISA/SNC.

(D) Cu K-edge XANES spectra of S-Cu-ISA/SNC and the references (Cu foil, CuS, and CuPc).

(E) FT k^3-weighted Cu K-edge EXAFS spectra of S-Cu-ISA/SNC and the references.

(F) WT-EXAFS plots of S-Cu-ISA/SNC, CuS, and CuPc, respectively.

(G) FT-EXAFS fitting curves plot of S-Cu-ISA/SNC at Cu K-edge.

(H) Illustration atomic interface model of S-Cu-ISA/SNC (Shang et al., 2020).

which is smaller than that of W_2C/WP@NC-1 (Figure 8B) and W_2C/WP@NC-4 (Figure 8D). The results showed that W_2C/WP@NC-2 illustrated high conductivity and quick charge-transfer rate.

In situ characterization

Ex situ techniques are used to establish the relationship between electrochemical performance and the properties of materials. However, *in situ* characterization can not only provide plenty of valuable information during the dynamic change process but also assess the coordination environment of the active site accurately. Nowadays, various *in situ* characterizations have gradually emerged with the continuous in-depth study of single atoms.

Infrared spectroscopy can directly detect the interaction between adsorbed molecules and the supporter surface, and time- and temperature-resolved Fourier transform infrared spectroscopy (FTIR) can be used to

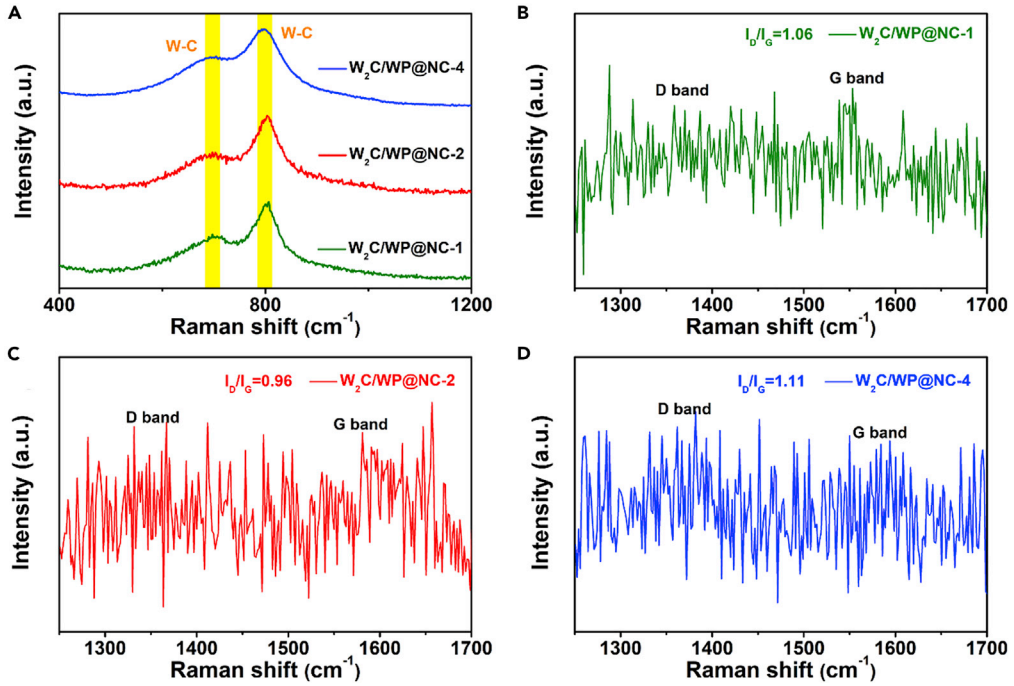

Figure 8. Images of Raman spectra

(A–D) Raman spectra (400–1200 cm^{-1}) of W_2C/WP@NC-1, W_2C/WP@NC-2, and W_2C/WP@NC-4. Raman spectra (1200–1700 cm^{-1}) of (B) W_2C/WP@NC-1, (C) W_2C/WP@NC-2, and (D) W_2C/WP@NC-4 (Wei et al., 2021b).

detect catalytic intermediates. By detecting the vibration frequency and intensity of the model, the characteristics of the active center can be inferred after appropriate correction. Selection of appropriate probe molecules, such as CO, NH_3, pyridine, and so on, can be used to analyze the overall catalyst, which is an important strategy to analyze the SACs. This paper mainly introduces the application of infrared spectroscopy in the characterization of SACs using CO as probe molecule. FTIR measurement was performed using CO as probe molecule to analyze the dispersion and oxidation state of Pt in the sample (Qiao et al., 2011) (Figure 9A). In sample B, there are three vibration bands in 2030 cm^{-1}, 1950 cm^{-1}, and 1860 cm^{-1}. The main peak at 2030 cm^{-1} is the linear adsorption of CO at Pt^0 site, whereas the weak vibration band at 1950 cm^{-1} and 1860 cm^{-1} is caused by the adsorption of CO on the bridge of two Pt atoms and the interface between Pt clusters and the support. That is, bridge-bonded CO indicates the presence of dimer or Pt clusters. These results indicate that Pt clusters and single atoms coexist in the samples. What's more, Hu and colleagues analyzed the existence state of Pt in Pt-SA/$CsPbBr_3$ NCs (Hu et al., 2021). The strong vibration peak at 2058 cm^{-1} indicates the linear adsorption of CO at the $Pt^{\delta+}$ sites, which proves the existence of single Pt atoms (Figure 9B). The absence of CO bridge adsorption peak indicates that Pt atoms may not have formed Pt nanoparticles or massive Pt atoms agglomeration.

In situ XAS can be used to analyze the evolution of the coordination environments during the catalytic process. Xiong et al. reported isolated single-atom Rh anchored on N-doped carbon (SA-Rh/CN) for formic acid oxidation (Xiong et al., 2020). The *in situ* XANES spectra of SA-Rh/CN were collected at Rh K-edge during chronoamperometry (CA) to investigate the change of oxidation state for Rh atom (Figure 9C). The results showed that the intensity of the main absorption peak at ~ 23250 eV gradually increased with the extending of reaction time, indicating that the oxidation state of Rh atoms became higher and higher, which may be caused by the formation of oxides in the process of high potential reaction. Similarly, the structural evolution and atomic interface structure of isolated Cu sites were collected by Cu K-edge XANES (Figures 9E and 9F) and EXAFS during ORR (Shang et al., 2020). *In situ* XAS was carried out in electrochemical cell set-up (Figure 9D). The energy at the edge decreases gradually, along with the intensity of the white line from 1.05 V to 0.75 V. The *in situ* spectroscopic analysis shed light on the evolution of the electronic and atomic structures of the Cu-S_1N_3 moiety of S-Cu-ISA/SNC, revealing that the low-valence (+1) Cu-N-bond-shrinking HOO-Cu-S_1N_3, O-Cu-S_1N_3 and HO-Cu-S_1N_3 may contribute to ORR activity

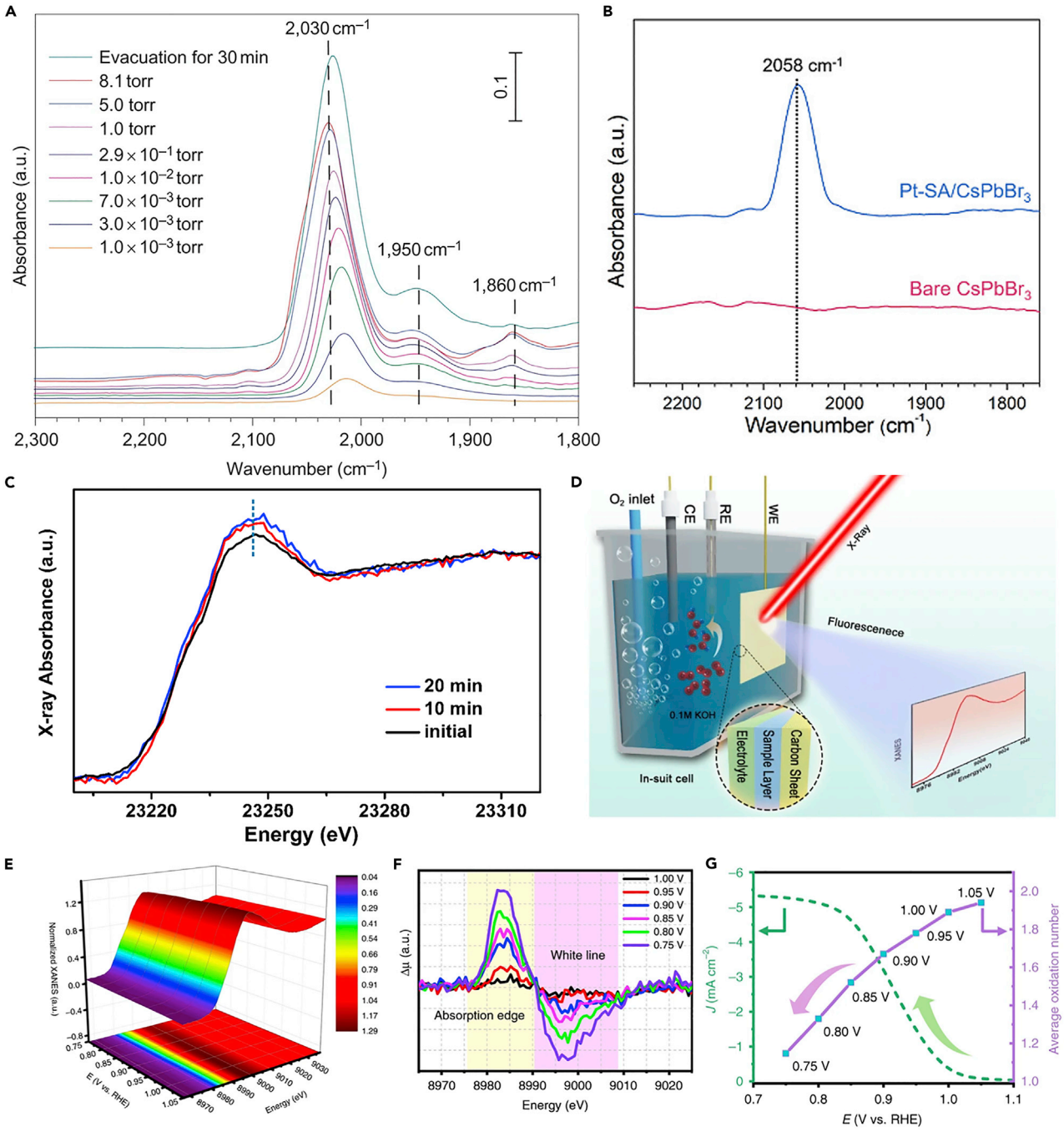

Figure 9. Images of *in situ* characterization

(A) *In situ* FTIR spectra of CO adsorption for sample B (Qiao et al., 2011).

(B) DRIFT spectra of CO adsorption on bare $CsPbBr_3$ NCs and 1.04% Pt-SA/$CsPbBr_3$ NCs (Hu et al., 2021).

(C) *In situ* XANES spectra of SA-Rh/CN (Xiong et al., 2020).

(D) Illustration of the *in situ* electrochemical cell set-up. WE, working electrode; CE, counter electrode; RE, reference electrode.

(E) Cu K-edge XANES spectra of S-Cu-ISA/SNC at different potentials in O_2-saturated 0.1 M KOH during the process of ORR catalysis.

(F) Differential spectra of Δμ XANES are the normalized spectra at each potential minus the spectra recorded at 1.05 V versus RHE.

(G) The relationship between the current density and potential for S-Cu-ISA/SNC (left) and the relationship between the average oxidation number of Cu species in S-Cu-ISA/SNC and potential (right) (Shang et al., 2020).

(Figure 9G). However, *in situ* XANES is not yet prevalent because of the extremely limited resources of synchrotron radiation. With the construction of more advanced synchronous light sources, *in situ* XANES will play an increasingly important role in scientific research.

In situ Raman is a powerful analytical tool for revealing the reaction route and analyzing the reaction mechanism due to the high temporal and spatial resolution. Surface-enhanced Raman scattering (SERS) is caused by electromagnetic and the charge transfer mechanism, which means that when the analyte is adsorbed on rough metal surface, its Raman signal will be enhanced (Cialla et al., 2012). Sun and colleagues employed the *in situ* SERS to monitor the adsorbate-substrate interaction in the process of ORR on the Au@Pd@Pt core/shell nanoparticles, which provided the direct evidence of *OOH intermediate (Sun et al., 2022). Furthermore, it is proved that the introduction of Pd shells affects the strain and electronic effect, leading to enhanced ORR activity. The relationship between ORR performance and strain/electron effect was illustrated by detecting intermediates from *in situ* SERS technique. What's more, time-resolved SERS (TR-SERS) was applied to reveal the dynamics of carbon dioxide (CO_2) reduction reaction intermediates on Cu electrodes (An et al., 2021). The results showed the surface reconstruction of Cu and the dynamic CO surface intermediates. This technique is of great significance for understanding the dynamic information of the surface reaction during CO_2 electrolysis.

However, SERS is limited to metal substrates with nanostructures. Shell-isolated nanoparticle-enhanced Raman spectroscopy (SHINERS) is applicable to the surfaces of various materials and nanostructures (Li et al., 2013). SHINERS are composed of a plasma gold or silver core and an inert shell such as SiO_2 and Al_2O_3. These shell-isolated nanoparticles are easy to manufacture and can be dispersed on the surface of analytes with different composition and morphology, which are employed to enhance the Raman vibration signal of nearby molecules (Ding et al., 2016). Wei and colleagues adopted *in situ* SHINERS to monitor the catalytic reaction process and kinetics of hydrogenation of nitro compounds and to characterize the structure of Pd single atoms for the first time (Wei et al., 2021a). Pd SAs were anchored on the surfaces of TiO_2 or Al_2O_3 shells of Au-shell-isolated nanoparticles. It also revealed the nucleation process of Pd species from single atoms to nanoparticles. This work provided a new spectroscopic tool for the *in situ* study of SACs, especially the solid-liquid interface.

SACS FOR ELECTROCHEMICAL REACTIONS

With the development of science and technology, researchers have developed numerous high-performance electrocatalysts, and the understanding about these reactions is gradually deepening. Density functional theory (DFT) calculations are widely used to study the free energies of intermediates and further reveal the mechanism of enhanced reactivity. The development of DFT theoretical models and advanced characterization techniques has greatly enhanced the understanding of electrocatalyst reaction mechanisms, such as the identification of active sites and the theory design of catalysts. Pt/C is considered to be the best catalyst for HER and ORR. RuO_2 and IrO_2 show the best catalytic performance toward OER. However, due to the scarcity and high price of precious metals, it is urgent to develop new type catalysts to reduce the production cost. SACs display great potential in the realization of efficient and selective electrocatalytic processes because of unique electronic structure and coordination environment. The surrounding coordination atoms of the central metal atom show important effects on their catalytic activity, selectivity, and stability, which are significant indicators of catalysts. In this section, the characterization of the existence of single atoms and coordination environments and their related catalytic performance will be discussed in detail.

Hydrogen evolution reaction

With the consumption of fossil fuels, a series of environmental problems have aroused people's attention. Hydrogen is considered to be the most likely alternative to fossil fuels due to its high energy density, no carbon emission, and without pollution. The method of electrolyzing water to produce hydrogen has attracted wide attention because of high efficiency, no need to consume fossil energy, and high product purity. Since Nicholson and Carlisle proposed the concept of water electrolysis in the 18th century, electrochemical water splitting has been developed for more than 200 years (Kreuter and Hofmann, 1998). Hydrogen evolution reaction (HER) is represented by the chemical formula as: $2H^+ + 2e^- \rightarrow H2$, which is a multi-step electrochemical process that occurs on the electrode surface to generate gaseous hydrogen at the cathode (Zheng et al., 2015). The reaction mechanism of HER is different in acidic and alkaline solutions, but both can be divided into two elementary reactions (Bockris and Potter, 1952; Sheng et al., 2010).

The first step is electrochemical hydrogen adsorption, which is called Volmer reaction. The second step is electrochemical desorption (Heyrovsky reaction) or chemical desorption (Tafel reaction). The mechanism under acidic conditions can be expressed as (Lasia, 2010)

$$H^+ + M + e^- \rightleftharpoons M - H^* \text{(Volmer reaction)} \quad \text{(Equation 1)}$$
$$M - H^* + H^+ + e^- \rightleftharpoons M + H_2 \text{(Heyrovsky reaction)} \quad \text{(Equation 2)}$$

or

$$2M - H^* \rightleftharpoons 2M + H_2 \text{(Tafel reaction)} \quad \text{(Equation 3)}$$

The mechanism under alkaline conditions can be expressed as

$$H_2O + M + e^- \rightleftharpoons M - H^* + OH^- \text{(Volmer reaction)} \quad \text{(Equation 4)}$$
$$M - H^* + H_2O + e^- \rightleftharpoons M + OH^- + H_2 \text{(Heyrovsky reaction)} \quad \text{(Equation 5)}$$

or

$$2M - H^* \rightleftharpoons 2M + H_2 \text{(Tafel reaction)} \quad \text{(Equation 6)}$$

where H* designates a hydrogen atom chemically adsorbed on an active site of the electrode surface (M).

As explained in Conway and Tilak in detail, the Tafel slope value obtained by the HER polarization curve can be used to judge the possible rate-determining step during the reaction process (Conway and Tilak, 2002). From these elementary reactions, we can see that the chemical adsorption and desorption of H atoms is a complicated process. According to the different pathways of H atom desorption, the HER reaction mechanism can be divided into Volmer-Heyrovsky mechanism and Volmer-Tafel mechanism (Li et al., 2016).

The bonding ability of the active sites in the catalyst and H* should neither be too strong nor too weak according to the Sabatier principle (Sabatier, 1920). When the bonding ability of M-H* is too strong, it is not conducive to the breaking of the bond and the release of hydrogen. On the contrary, it is not beneficial to the process of proton-electron transfer. However, the bond energy between the active site of the catalyst and H* cannot be measured directly, so it is difficult to establish a direct correlation between the intermediate H* and the electrochemical reaction rate (Marković and Ross, 2002). From the perspective of physics and chemistry, the adsorption free energy of H* (ΔG_{H^*}) can be used to evaluate the capacity of H adsorption and the release of H_2 (Nørskov et al., 2005). Therefore, ΔG_{H^*} is a key parameter used to evaluate the reaction rate. ΔG_{H^*} close to zero could be used to evaluate the efficiency of the catalyst, but not a requirement. More importantly, it is concluded that the experimental exchange current density j_0 value and ΔG_{H^*} have a "volcano curve" correlation through DFT calculation (Skúlason et al., 2010).

As can be seen from the volcano diagram (Zeradjanin et al., 2016), Pt is located at the top of the volcano diagram, indicating appropriate adsorption energy and the highest current density, which explains the optimal performance of Pt in HER (Figure 10A). However, due to the scarcity of precious metals, the application of SACs in HER has attracted wide attention from researchers in order to improve atomic utilization rate and reduce catalyst cost. Meanwhile, the development of high-active non-noble-metal catalysts is also an effective solution.

The introduction of heteroatoms into carbon substrate can not only form new coordination environments but also improve metal loading, which has attracted extensive attention of researchers. The general coordination number between metal atom and N atom is 4, which may be related to the valence state and electronic structure of the central atom. For example, Ye and colleagues reported single Pt atoms anchored on aniline-stacked graphene with a Pt loading of 0.44 wt% through microwave reduction method (Ye et al., 2019). The Pt SASs/AG with unique Pt-N_4 coordination not only displays high HER activity with the overpotential of 12 mV at 10 mA cm^{-2} in 0.5 M H_2SO_4, better than 20 wt% Pt/C, but also the mass current density of 22,400 Ag_{Pt}^{-1} at the overpotential of 50 mV is 46 times higher than commercial 20 wt% Pt/C. Moreover, stability is also a significant issue in the development SACs. Cyclic stability and long-term stability can be assessed by cyclic voltammetry sweeps and chronopotentiometric measurements. The Pt SASs/AG shows negligible decay by comparing the LSV curves before and after 2000 cycles and displays outstanding long-term stability over 20 h. From the XPS spectrum of Pt 4f (Figure 10B), it shows the strong interaction of Pt and aniline-formed $Pt^{\delta+}$ XAFS, and DFT calculations show that the isolated Pt is coordinated with the N of four aniline molecules (Figures 10C–10E), which optimizes the electronic structure of Pt. The modulation

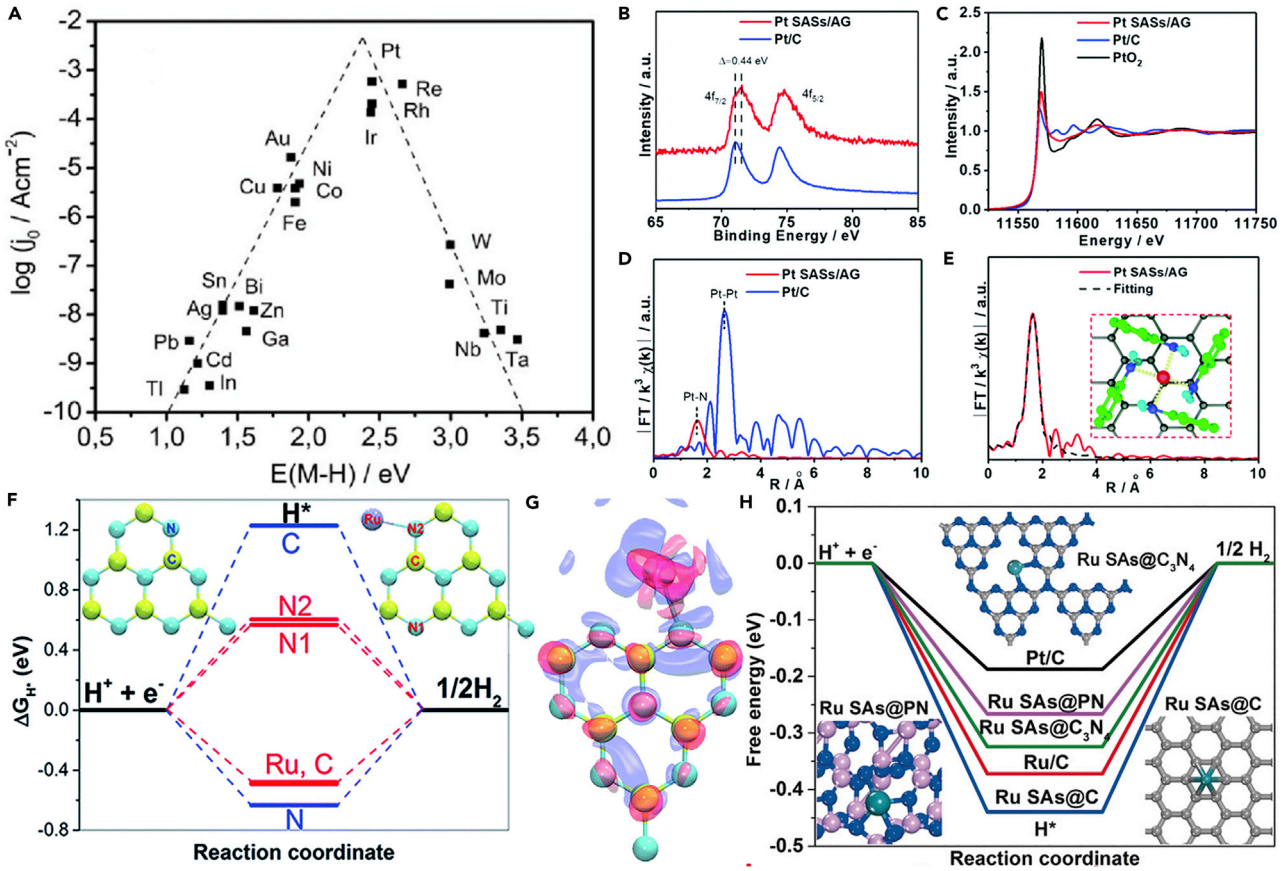

Figure 10. Noble-metal-based SACs for HER

(A) HER "volcano" plot for different metal elements (Zeradjanin et al., 2016).

(B) The XPS spectra of Pt 4f.

(C and D) XANES and (D) FT-EXAFS spectra of the Pt L_3-edge of Pt SASs/AG and Pt/C.

(E)The EXAFS fitting curve of Pt SASs/AG R-space. Inset: the model of the Pt SASs/AG (Ye et al., 2019).

(F) The Gibbs free energy of HER for C_3N_4 (blue) and C_3N_4–Ru (red) at the equilibrium potential at different bonding sites.

(G) Schematic diagram of interfacial charge transfer in C_3N_4–Ru. Red and blue signals are positive and negative charge, respectively. The isosurface value of 0.003 e au^{-3} (Peng et al., 2017).

(H) The calculated HER free-energy diagram at the equilibrium potential for Pt/C, Ru/C, Ru SAs@C, Ru SAs@C_3N_4, and Ru SAs@PN (Yang et al., 2018b).

of the d-band center and density of states (DOS) near the Fermi level of Pt atoms by aniline caused the single Pt sites to have appropriate hydrogen adsorption energy and finally enhances HER activity. In addition, other noble-metal-based SACs have also been studied for HER. The unsaturated coordination between the central Ru atom and the surrounding N atom can also significantly enhance HER performance. For example, C_3N_4-Ru were fabricated by thermal treatment of graphitic C_3N_4 nanosheets and $RuCl_3$ in water, which shows apparent HER activity in acidic media, and the HER activity is positively correlated with loading of Ru (Peng et al., 2017). The test results showed charge transfer from C_3N_4, a unique functional scaffold, to the Ru center (Figure 10G). The formation of unsaturated coordination Ru-N_2 moieties as effective active sites facilitated the adsorption of hydrogen from the DFT calculation (Figure 10F). Besides, single Ruthenium atoms were anchored amorphous phosphorus nitride nanotubes (Ru SAs@PN) through strong coordination interactions between the d orbitals of Ru and the lone pair electrons of N located in the HPN matrix (Yang et al., 2018b). The SACs in Ru-$N_{3.8}$ coordination environment were prepared by impregnation method. The Ru SAs@PN showed excellent HER activity with overpotential of 24 mV at 10 mA cm^{-2} and robust long-term stability over 24 h in 0.5 M H_2SO_4. DFT calculations showed that the Gibbs free energy of adsorbed H* over the Ru SAs on PN is much closer to zero compared with the Ru/C and Ru SAs supported on carbon and C_3N_4 (Figure 10H). Therefore, adjusting the number of coordination atoms of metal centers is considered to be a very effective way to optimize HER performance.

In recent years, non-noble-metal-based SACs have also attracted extensive attention. However, compared with Pt based catalysts, their performance still needs to be further improved. Non-noble-metal-based SACs with low coordination environment and unique electronic structure have the potential to replace Pt-based catalysts (Chen et al., 2017a; Zhang et al., 2018). Graphdiyne (GD) is a two-dimensional carbon material with monatomic thickness, which has natural uniform pores, rich triple bonds, and strong reduction ability (Li et al., 2010, 2014). It has been used in various research fields, so GD may also be an excellent candidate as support. Isolated nickel/iron atoms anchored on graphdiyne were fabricated by electrochemical synthesis method with Ni-C and Fe-C coordination, respectively (Xue et al., 2018) (Figure 11A). From the results of ICP-MS, the loading of Ni in Ni/GD is 0.278 wt% and the loading of Fe in Fe/GD is 0.680 wt%. Fe/GD with higher metal laoding exhibits the overpotential of 66 mV at 10 mA cm^{-2}, which is smaller than Ni/GD (88 mV). And their performances are superior to the most state-of-the-art bulk nonprecious catalysts. Meanwhile, the Fe/GD displays more superior durability through 5000 cycling tests. The strong chemical interaction and electronic coupling between single atoms Ni/Fe and GD allow a high charge transfer between the catalytic active center and the support, so the performance of HER is improved.

In addition to coordinating with the same type of surrounding atom, the central metal atom can also coordinate with different atoms simultaneously. Mo-based catalysts such as carbide, nitride, and sulfide have attracted a lot of attention because of good performance in HER. Chen and colleagues designed single Mo atoms supported on N-doped carbon for the first time (Chen et al., 2017a), which shows high HER performance with the overpotential of 132 mV at 10 mA cm^{-2} and onset overpotential of 13 mV in 0.1 M KOH. From AC-STEM and XAFS, it can be seen that $Mo_1N_1C_2$ was formed by single Mo atom immobilized with one nitrogen atom and two carbon atoms (Figures 11B–11F). More importantly, the active sites $Mo_1N_1C_2$ showed higher catalytic activity than Mo_2C and MoN due to the lowest absolute value of ΔG_{H^*} in $Mo_1N_1C_2$ compared with the Mo_2C and MoN from the DFT calculation results. Further DOS calculations revealed that the DOS of $Mo_1N_1C_2$ near the Fermi level was much higher than that of Mo_2C and MoN, which was favorable for the charge transfer during the HER process because of higher carrier density. Moreover, tungsten-based catalysts, including WC_x (Gong et al., 2016; Wang et al., 2020), WN_x (Yan et al., 2015b), WP_x (Wang et al., 2016; Xing et al., 2015), WS_x (Lin et al., 2014; Lukowski et al., 2014; Merki and Hu, 2011; Voiry et al., 2013), and so on, also have outstanding properties in HER. However, in order to achieve industrial application, it is necessary to further improve HER activity and stability of the tungsten-based materials. W-SAC with W-N_1C_3 sites supported on MOF-derived N-doped carbon was prepared for HER in both alkaline and acidic media (Chen et al., 2018a). The W-SAC showed excellent stability without attenuation after 10,000 CV cycles. It is determined by HAADF-STEM and XAFS that the atomically dispersed $W_1N_1C_3$ act as the active site, which plays a significant role in enhancing the HER performance as proved by DFT calculation results. The DOS of W-SAC near the Fermi level is much higher than of WC and WN, leading to a larger carried density for promoting charge transfer in HER (Figures 11G and 11H). Furthermore, the DOS near the Fermi level in W-SAC was mainly contributed by the W d-orbital, whereas the contributions of C and N p-orbital were negligible; this suggested that the single W dispersion as well as unique electronic structure could efficiently enhance the d-electron domination near the Fermi level and enhance the HER catalytic performance. The coordinating atom N is partially replaced by other atoms, which shows a great influence on the local chemical environment of the central atom. Thus, it can be used to optimize the electronic structure of the central atom and is an important method to enhance the activity of SACs by modulating the N coordination to form dual-atom coordination.

Oxygen evolution reaction

Oxygen evolution reaction (OER) is another important half-reaction that occurs at the anode during the water electrolysis process, involving four coordinated proton-electron transfer steps. However, there is still a long way to go in the mechanism understanding and material design of OER catalysts. As shown in Figure 12A (Chen et al., 2021), the generally accepted OER reaction mechanisms are the traditional adsorbate evolution mechanism (AEM) and lattice oxygen mechanism (LOM).

In AEM, the reaction mechanism of OER is similar to HER, involving the steps of adsorption and desorption. The mechanism can be expressed as follows (Man et al., 2011; Rossmeisl et al., 2007):

$$^* + H_2O(1) \rightarrow OH^* + H^+ + e^- \quad \text{(Equation 7)}$$

$$OH^* \rightarrow O^* + H^+ + e^- \quad \text{(Equation 8)}$$

$$O^* + H_2O(1) \rightarrow OOH^* + H^+ + e^- \quad \text{(Equation 9)}$$

$$OOH^* \rightarrow O_2(g) + H^+ + e^- \quad \text{(Equation 10)}$$

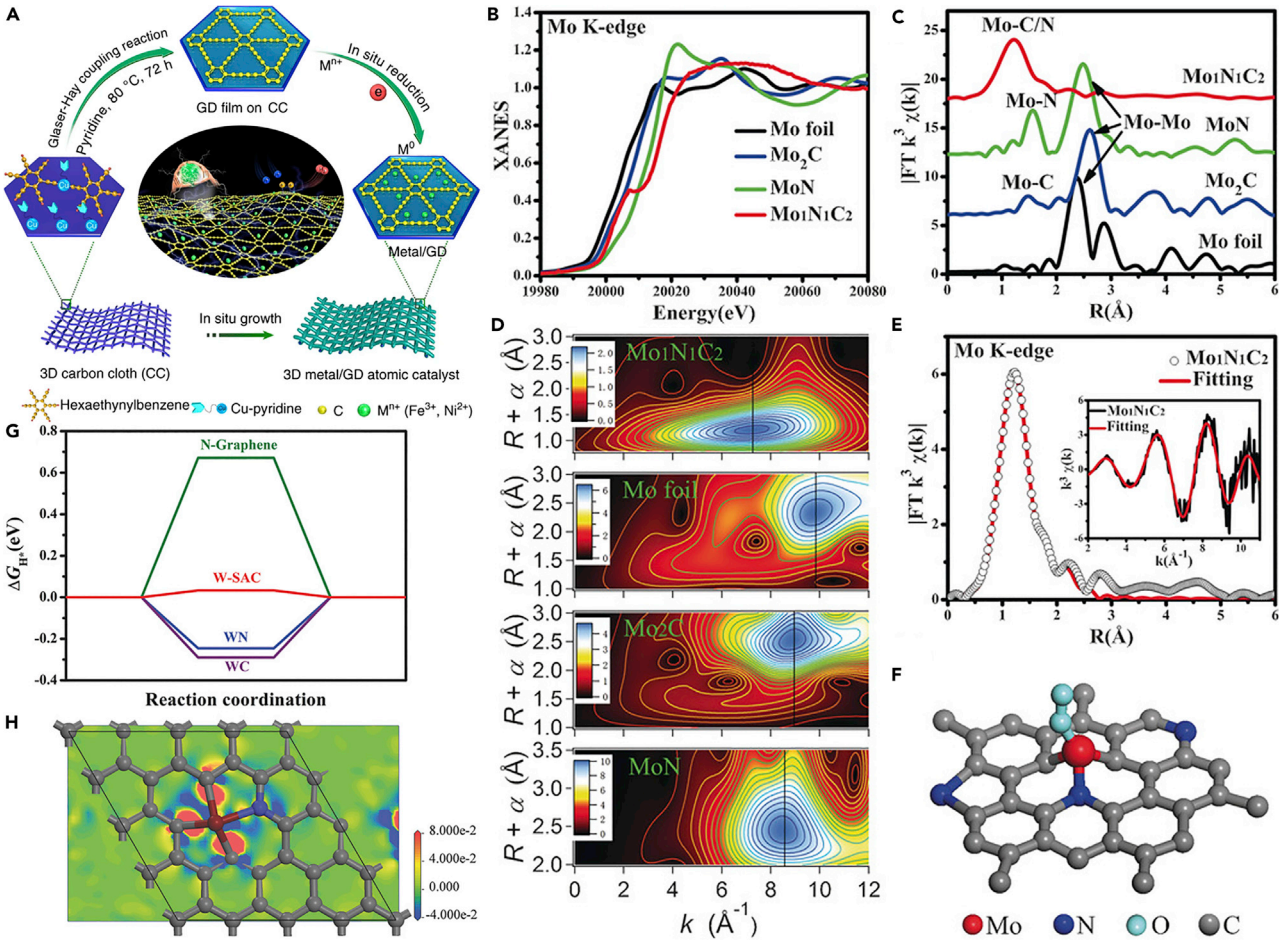

Figure 11. Non-noble-metal SACs for HER

(A) Protocols for the synthesis of Ni/GD and Fe/GD (Xue et al., 2018).

(B) XANES and (C) FT-EXAFS curves of the $Mo_1N_1C_2$ at Mo K-edge.

(D) WT-EXAFS of the $Mo_1N_1C_2$, Mo foil, Mo_2C, and MoN.

(E) FT-EXAFS fitting curves of the $Mo_1N_1C_2$ at Mo K-edge (FT range: 2.0–10.5 $Å^{-1}$, fitting range: 0.5–2.5 Å), inset: k space fitting curve of $Mo_1N_1C_2$.

(F) Atomic structure model of the $Mo_1N_1C_2$ (Chen et al., 2017a).

(G) Gibbs free energy (ΔG_{H^*}) of hydrogen adsorption on the W-SAC, WC, WN, and N-doped graphene.

(H) The differential charge density slice parallel to the xy plane for W-SAC (Chen et al., 2018a).

Similarly, OER also has a volcanic curve based on oxygen adsorption energy. Noble metal oxides, such as IrO_2 and RuO_2, showed the best OER performance due to low overpotential. Based on this mechanism, the OER performance can be effectively improved by modifying the catalyst supports, such as introducing heteroatoms through synergistic effects to optimize the electronic structure, creating defects to redistribute surface charges and so on.

LOM has attracted much attention in recent years. The lattice oxygen participates in the proton-electron transfer in the reaction process (Huang et al., 2019). The mechanism can be expressed as follows (Rong et al., 2016):

$$OH^* \rightarrow (V_O + OO^*)^\dagger + H^+ + e^- \quad \text{(Equation 11)}$$

$$(V_O + OO^*)^\dagger + H_2O(1) \rightarrow O_2(g) + (V_O + OH^*)^\dagger + H^+ + e^- \quad \text{(Equation 12)}$$

$$(V_O + OH^*)^\dagger + H_2O(1) \rightarrow (H^*_{O-site} + OH^*)^\dagger + H^+ + e^- \quad \text{(Equation 13)}$$

$$(H^*_{o-site} + OH^*)^\dagger \rightarrow OH^* + H^+ + e^- \quad \text{(Equation 14)}$$

† Parentheses indicate that adsorbates are calculated in the same supercell.

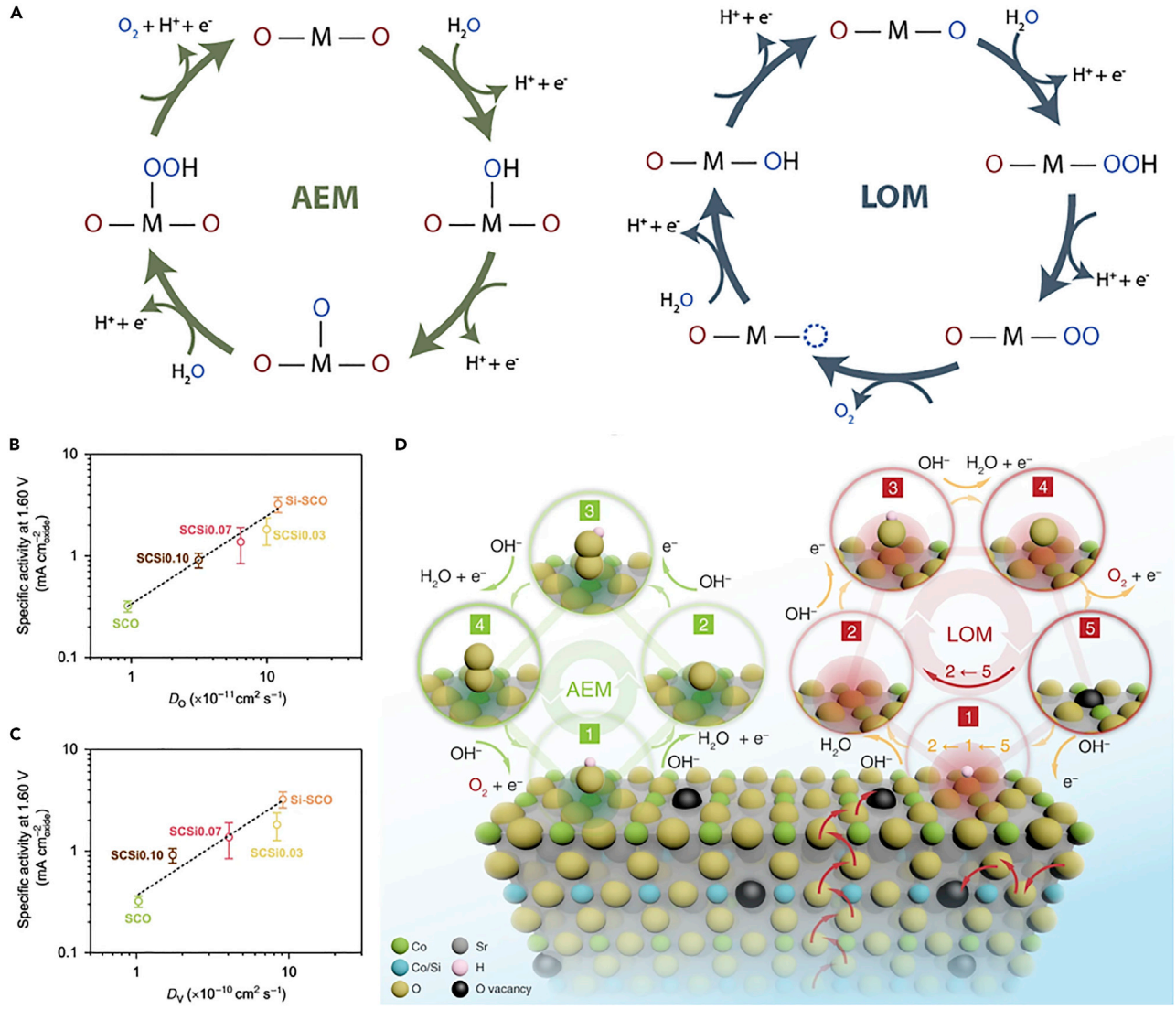

Figure 12. Schematic diagrams of OER mechanism

(A) The reaction pathways of OER (Chen et al., 2021).

(B) Correlation between intrinsic OER activity and the oxygen anion diffusion rate in 0.1 M KOH.

(C) Correlation between intrinsic OER activity and the oxygen vacancy diffusion rate in 0.1 M KOH.

(D) A schematic diagram of the AEM and LOM reaction pathways for Si-incorporated strontium cobaltites (Pan et al., 2020).

In early studies, the involvement of lattice oxygen in OER process under acidic conditions was confirmed by isotope labeling and differential electrochemical mass spectrometry (DEMS) techniques (Kötz et al., 1984; Willsau et al., 1985; Wohlfahrt-Mehrens and Heitbaum, 1987). The O in RuO_2 participates in the reaction to form soluble RuO_4, which is detected in the solution. Pan and colleagues reported a model system of Si-incorporated strontium cobaltite perovskite electrocatalysts in alkaline solution with similar surface transition metal properties but different oxygen diffusion rates (Pan et al., 2020). The correlation of intrinsic OER activity with oxygen ion diffusion rate and oxygen vacancy diffusion rate are shown in Figures 12B and 12C. The evolution of oxygen correlates with the contribution of the LOM mechanism at different degrees that closely relates to the oxygen ion diffusivity (Figure 12D). This work provides a reference for designing more stable perovskite surfaces to further optimize electrocatalysts. A series of perovskite OER catalysts were also tested through *in situ* ^{18}O isotope labeling mass spectrometry (Grimaud et al., 2017). The results showed that the O_2 generated from the lattice oxygen for some highly active oxides. In combination with experiments and DFT calculations, catalysts with lattice oxygen exchange exhibited pH-dependent

OER activity, whereas those without lattice oxygen exchange displayed pH-independent OER activity. LOM shows higher OER activity than the conventional AEM as proved for the ABO_3 (A = lanthanum or strontium, B = transition metal) perovskites (Yoo et al., 2018). Activity volcano plots for AEM and LOM of perovskite systems have been established by a simulation work. Furthermore, the LOM is preferred for achieving bifunctional catalysts for OER and ORR.

In the HER and OER of water splitting, OER is the core of electrochemical energy conversion. However, OER displays high overpotential during the reaction because of sluggish kinetics, which is the main step of energy consumption. Therefore, high-efficiency electrocatalysts are particularly important to OER (Chen et al., 2019; Liu et al., 2021; Zhou et al., 2019). RuO_2 and IrO_2 exhibit high catalytic activity for OER in a wide pH value and are often used as benchmarks for OER catalyst evaluation. It was found that the coordination environments of single atom may undergo changes during the process of reaction. Ru single atoms anchored on nitrogen-carbon support (Ru-N-C) were synthesized with Ru_1-N_4 sites (Cao et al., 2019). The catalyst showed an efficient and durable electrocatalyst for acidic OER with overpotential of 267 mV at the current density of 10 mA cm^{-2}, mass activity of 3571 A $g_{metal}{}^{-1}$, and TOF of 3348 O_2 h^{-1}. The dissolution rate of Ru is less than 5% in acid solution due to the outstanding structural stability. The Ru-N-C was employed to measure the overall water splitting in a two-electrode system to mimic the PEMWE, showing superior activity and stability. The dynamic pre-adsorption of single oxygen atom into the formation of O-Ru_1-N_4 structure with more charge donations of Ru through *in situ* XAFS and FTIR was also identified (Figures 13A–13F). Theoretical calculations showed O-Ru_1-N_4 with higher Ru oxidation state as the real active site for the high OER activity in acidic solution. The formed O-Ru_1-N_4 moieties under operando state exhibited a low barrier of O-O coupling to form the OOH* intermediate. It is also an effective way to prepare SACs by creating defects on the support to regulate the coordination environment. Atomically dispersed Ni catalyst on defective graphene (a-Ni@DG) with four-coordination Ni-C_4 structure was fabricated through an incipient wetness impregnation method and subsequent acid leaching (Zhang et al., 2018). The Ni loading of a-Ni@DG was around 1.24 wt% by this facile and inexpensive strategy. XAS and DFT calculation revealed that the diverse defects in graphene can induce different local electronic DOS of a-Ni, which suggested that aNi@defect serves as an active site for unique electrocatalytic reactions (Figures 13J–13L). For example, aNi@G5775 and aNi@G585 are responsible for HER and OER with low overpotential and high TOF values and stability, respectively. HAADF-STEM not only confirmed the uniform distribution of single Ni atoms but also observed that aNi trapped in the Di-vacancy provided direct evidence for the Ni-C_4 configuration (Figures 13G–13I). Diverse defects can induce different local electronic density of states. Creating specific defects on the support forming various active sites can achieve good catalytic effects for different reactions at the same time.

What's more, bimetallic center SACs have gradually attracted extensive attention from researchers. The synergistic effect of bimetallic centers can optimize the adsorption and desorption of intermediates and reduce the reaction energy barrier. For example, atomically dispersed binary Co-Ni sites embedded in N-doped hollow carbon nanocubes (CoNi-SAs/NC) are synthesized for bifunctional OER and ORR (Han et al., 2019b) (Figure 13M). The rechargeable process of Zn-air batteries is realized efficiently and with low potential and robust reversibility. DFT calculation showed that the uniformly dispersed single sites and synergistic effect of adjacent Co-Ni bimetallic centers optimized the adsorption and desorption process, reduced the overall reaction energy barriers, and finally promoted the reversible oxygen electrocatalysis.

In the reported literature, the activity and stability of HER and OER were measured in standard three-electrode system of lab scale. Nonetheless, the catalyst's performance in the lab scale is somewhat different from that in practical electrolyzers. The practical electrolyzers usually require higher current density and voltage, and the operating environment is more intense. Therefore, the practical electrolyzers put forward higher requirements for the activity and stability of the catalysts.

Currently, the electrolyzers used for water electrolysis include alkaline water electrolyzers (AWE), proton exchange membrane water electrolyzers (PEMWE), and anion exchange membrane water electrolyzers (AEMWE). Although traditional AWE has been fully industrialized, it is limited by its environmental friendliness and purity of hydrogen production. PEMWE and AEMWE have received extensive attention due to the high efficiency, high purity of hydrogen produced, and low energy consumption. Influenced by the properties of the membrane and the local pH, PEMWE and AEMWE are suitable for catalysts in acidic

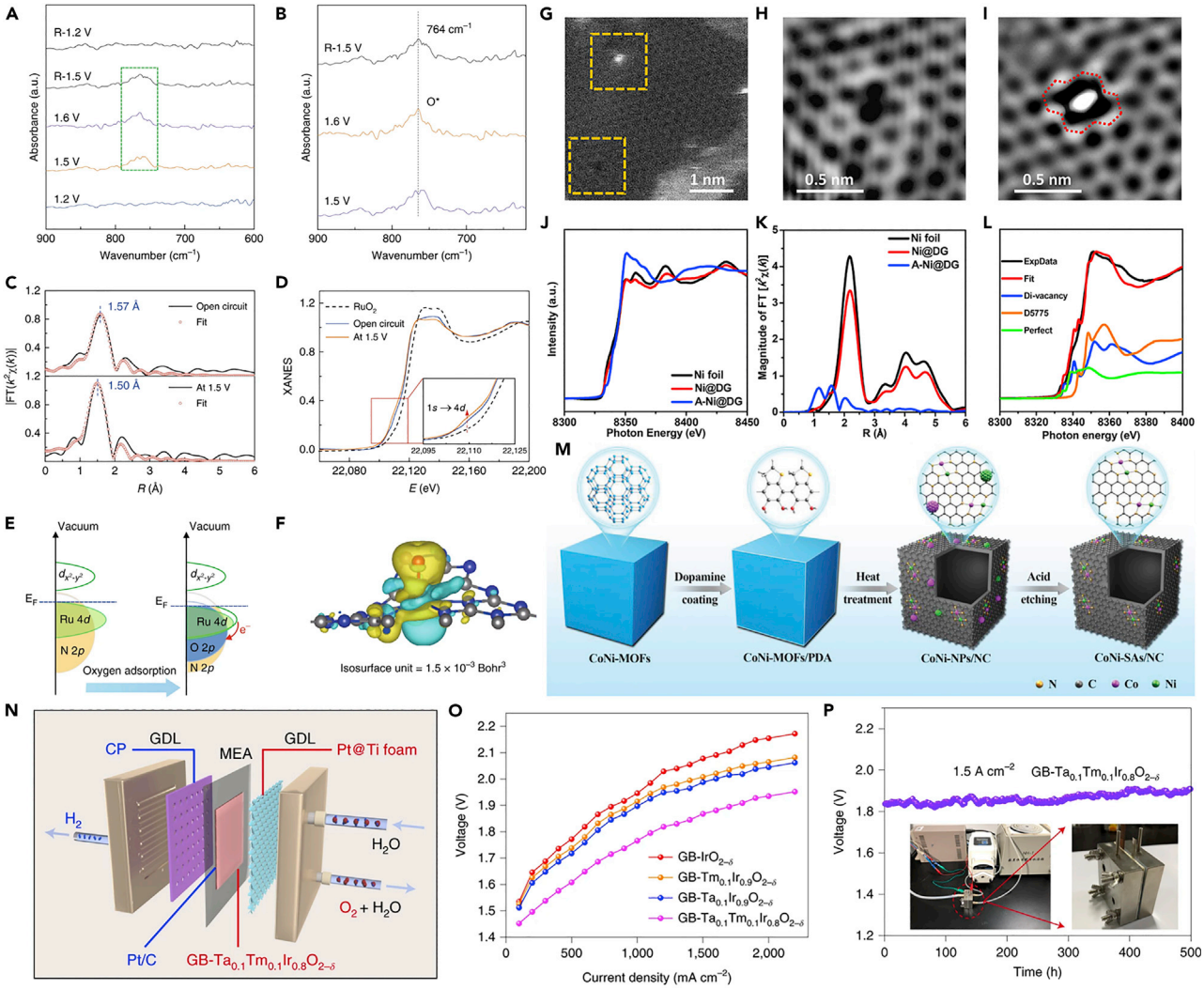

Figure 13. The application of SACs for OER

(A) The operando SR-FTIR spectroscopy measurements of Ru-N-C in the acid OER process.

(B) The amplified infrared signal at ~764 cm^{-1}.

(C) The operando EXAFS spectrum and the fitting curves of first shell for Ru-N-C from the open circuit condition to 1.5 V under various voltages in OER process.

(D) Operando XANES spectrum of Ru-N-C in OER process. Inset: magnified pre-edge XANES region.

(E) Schematic diagram of the effect of oxygen adsorption on the electronic structure of Ru-N-C.

(F) Electron density difference map of the O-Ru_1-N_4 (Cao et al., 2019).

(G) The image of HADDF-STEM for A-Ni@DG.

(H) The enlarged image of the defective area (vacancy) marked with the yellow dotted line frames in the lower left corner of (G).

(I) The enlarged image of the defective area (with atomic Ni trapped) marked with the yellow dotted line frames in the upper left corner of (G).

(J and K) Ni K-edge XANES spectra (J) and the K^2-weighted Fourier transform spectra (K) of Ni@DG, A-Ni@DG, and the Ni foil reference samples.

(L) The LCF analysis of XANES theoretical modeling (Zhang et al., 2018).

(M) Schematic protocol of the synthesis method of CoNi-SAs/NC (Han et al., 2019b).

(N) Illustration of the PEM water electrolyzer.

(O) Polarization curves of the PEMWE applying as-prepared catalysts as anode.

(P) The stability measurement of GB-$Ta_{0.1}Tm_{0.1}Ir_{0.8}O_{2-\delta}$ in the PEMWE at 1.5 A cm^{-2} (Hao et al., 2021).

and alkaline environments, respectively. The current development of PEMWE is relatively mature in commercial-scale water electrolysis for long-term operation, but the progress of durable catalysts other than Ir-based noble metal OER catalysts in acidic environments remains a great challenge. As more OER catalysts display better performance in alkaline environment, AEMWE shows certain advantages, but the stability of

membrane and the design of electrolyzer still need to be further improved to meet the requirements of long-term electrolysis.

The membrane electrode assemblies (MEA), composed of the catalytic layer and the proton exchange membrane, is the main site for material transport and electrochemical reaction in the entire electrolytic cell. The characteristics and structure of the MEA directly affect the performance and life of the PEMWE. Hao and colleagues applied the prepared grain boundaries (GB)-$Ta_xTm_yIr_{1-x-y}O_{2-\delta}$ nanocatalysts to PEMWE as anode in an acidic condition (Hao et al., 2021). The pretreated carbon paper- (CP) and platinum-plated titanium foam were applied as cathode and anode gas diffusion layers (GDLs), respectively. The MEA were constructed by placing the catalyst-supported Nafion 117 membrane between CP and Pt-plated Ti foam GDLs (Figure 13N). The polarization curves were measured at 50°C, showing the cell voltage of GB-$Ta_{0.1}Tm_{0.1}Ir_{0.8}O_{2-\delta}$ is 1.766V to reach the current density of 1 A cm^{-2} (Figure 13O). Moreover, the PEMWE using GB-$Ta_{0.1}Tm_{0.1}Ir_{0.8}O_{2-\delta}$ displayed the outstanding stability at 1.5 A cm^{-2} for at least 500 h without obvious attenuation (Figure 13P). However, the research of SACs on PEMWE still needs to be further explored.

Oxygen reduction reaction

Oxygen reduction reaction (ORR) occurs at the cathode of electrochemical energy equipment through either a 4-electron pathway ($O_2+4H^++4e^-\rightarrow 2H_2O$) or a 2-electron pathway ($O_{2+}2H^++2e^-\rightarrow H_2O_2$). The four-electron reaction mechanisms are shown as follows (Nørskov et al., 2004):

$$\frac{1}{2}O_2 + {}^* \rightarrow O^* \xrightarrow{e^-+H^+} HO^* \xrightarrow{e^-+H^+} H_2O + {}^* \quad (15)$$

or

$$O_2 + {}^* \xrightarrow{e^-+H^+} HOO^* \xrightarrow{e^-+H^+} H_2O + O^* \xrightarrow{e^-+H^+} HO^* \xrightarrow{e^-+H^+} H_2O + {}^* \quad (16)$$

The two-electron reaction mechanisms are shown as follows:

$$O_2 + {}^* \xrightarrow{e^-+H^+} HOO^* \xrightarrow{e^-+H^+} H_2O_2 + O^* \quad (17)$$

where * represents the catalytically active sites.

The Equations (7) and (8) represent dissociative and associative mechanisms, respectively. Whether the O-O bond breaks during ORR process determines the selectivity of H_2O_2 or H_2O. The 2-electronic process is clean and pollution free, and the hydrogen peroxide produced is an important fine chemical. The 4-electronic process produces water directly, which is mainly used in fuel cells and metal-air batteries (Liu et al., 2018; Tong et al., 2021; Zhou et al., 2021b). However, these two reaction pathways often occur at the same time, resulting in reduced selectivity of the desired product. Thus, the application of SACs in ORR has been extensively studied to improve selectivity, stability, and activity.

The precious-metal-group (PMG) catalysts exhibit high-efficiency electrocatalytic performance for ORR. Doping heteroatoms into carbon materials can affect the coordination environment of the metal center atoms, which in turn shows an impact on the catalytic performance. M-N-C catalysts with M-N_4 coordination structure are considered as potential catalysts for replacing Pt-based materials in ORR. Single Pt atoms supported on carbon black were fabricated with carbon monoxide/methanol tolerance for ORR (Liu et al., 2017). DFT calculations were used to study the synergetic effect between single Pt atoms and doped-N and the intrinsic activity of the active sites on Pt_1-N/BP (carbon black) (Figures 14A and 14B). The results showed that the main effective sites are single-pyridinic-nitrogen-atom-anchored single-Pt-atom centers, displaying highly active and making it one of the most promising sustainable, large-scale alternatives to conventional Pt-NP-based electrocatalysts. The catalyst was employed as a cathode in acid single cell, and the power density reached 680 mW cm^{-2} at 80°C. The current of Pt_1-N/BP still maintains more than 70% when used as cathode in fuel cell after working for 200 h continuously. It shows good stability compared with other non-noble-metal catalysts. Other precious metal-based SACs have also been used in ORR studies. Ir-N-C SAC with Ir-N_4 configuration fabricated by host strategy exhibited orders of magnitude higher ORR activity than Ir NPs (Xiao et al., 2019) (Figure 14C). The Ir-SAC was applied in a H_2/O_2 fuel cell as cathode, showing a higher open circuit voltage of 0.0955V and a power density of 932 mW cm^{-2}. The SEM and HAADF-STEM displayed the morphology and nanostructure of Ir-SAC, and the EDS mapping showed the existence of Ir embedment within the carbon matrix (Figures 14D–14H). The bright spots in Figure 14I

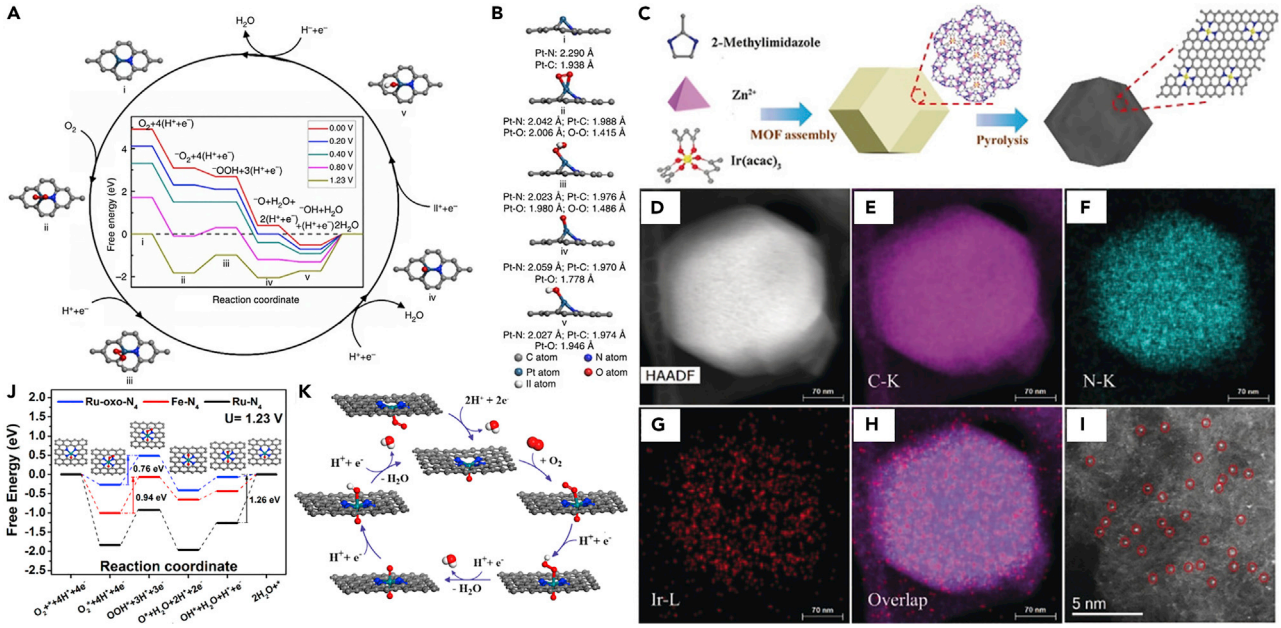

Figure 14. The application of noble-metal-based SACs for ORR

(A and B) The proposed reaction pathways for complete ORR on the g-P-N_1-Pt_1. (A) Top view; (B) side view and bond lengths. The inset in cycle (A) is the free energy plot for ORR on the g-P-N_1-Pt_1 in acidic solution (Liu et al., 2017).

(C) Host–guest strategy diagram for the synthesis of single atomic site catalysts.

(D–H) STEM images and the corresponding EDX mappings of Ir-SAC.

(I) The image of high-resolution HAADF-STEM for Ir-SAC (Xiao et al., 2019).

(J) Free-energy illustration of the ORR on selected N-coordinated metal moieties embedded on graphene sheets.

(K) Proposed reaction diagram of the associative mechanism for the ORR on Ru-oxo-N_4 moiety in acidic solution (Zhang et al., 2017a).

corresponded to the atomically dispersed Ir atoms. Atomic structure characterization results and DFT calculations showed that the high activity of Ir-SAC was attributed to the moderate adsorption energy of the Ir-N_4 moiety. Single Ru atoms supported on N-doped graphene oxide for ORR in acidic solution were prepared through NH_3 atmosphere annealing (Zhang et al., 2017a). The Ru/N-doped graphene showed excellent four-electron ORR activity, stability, and tolerance. Combing the DFT calculations, the Ru-oxo-N_4 moieties during the oxidative electrocatalytic condition are responsible for the ORR catalytic activity (Figures 14J and 14K).

Recently, transition-metal-based catalysts have emerged as promising alternatives to PMG materials due to the adjustable electronic structure. Fe-N_4 is considered to be the best performing non-noble-metal catalyst in ORR. Chen and colleagues performed adjustment of O coordination on Fe SACs to enhance ORR performance. Single iron atoms anchored on N-porous carbon with Fe loading of 2.16 wt% were fabricated through a cage-encapsulated-precursor pyrolysis strategy (Chen et al., 2017b). It can be seen from XANES that Fe is positively charged (Figure 15A). According to the analysis results of FT-and WT-EXAFS, Fe exists in the form of a single atom in the catalyst (Figures 15B–15E). Meanwhile, the corresponding EXAFS R space fitting curves of Fe-ISAs/CN is shown as Figure 15F. The coordination number of Fe is 5 with four N atoms and one O atom. So, the atomic structure model is shown in Figure 15G through further analysis. The Fe as isolated atoms with N coordination showed higher ORR activity than commercial Pt/C and most non-precious-metal materials, which was attributed to the high capability of the single Fe atoms in transferring electrons to the adsorbed OH species demonstrated by first principle calculations. Meanwhile, Fe-ISAs/CN showed superb durability with little change in $E_{1/2}$ for 5000 CV sweeps.

What's more, changing the metal central atom is a direct means to regulate the coordination environment, which also affects the catalytic performance. Single Co atom and N co-doped carbon nanofibers with CoN_4-G coordination were reported for ORR in both acidic and basis medium (Cheng et al., 2017). TEM and HRTEM showed that the diameter of the prepared catalyst was about 150 nm, and the substrate

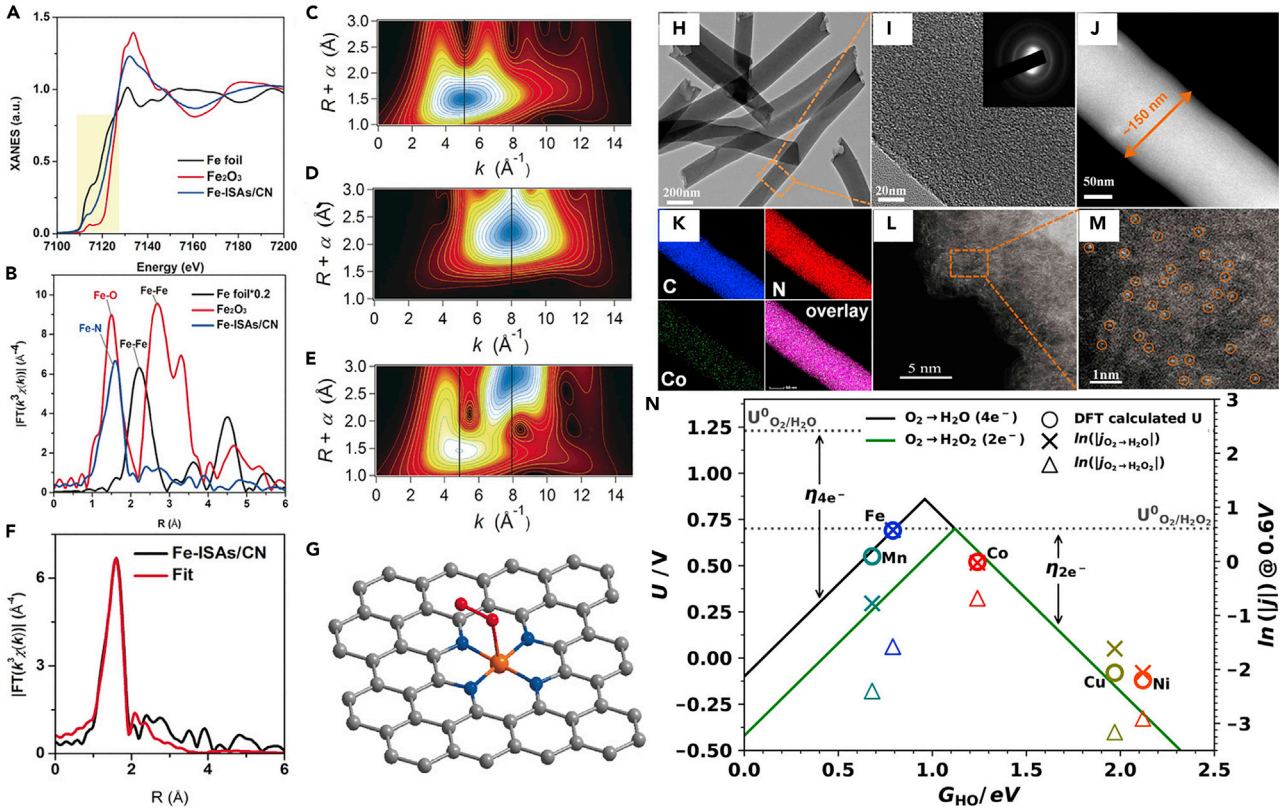

Figure 15. SACs for ORR

(A) XANES spectra.

(B) FT of the Fe K-edge and WT of Fe-ISAs/CN (C), Fe foil (D), and Fe_2O_3 samples (E).

(F) The corresponding EXAFS *r* space fitting curves of Fe-ISAs/CN.

(G) Protocol model of Fe-ISAs/CN (Chen et al., 2017b).

(H) TEM image and (I) zoomed-in TEM image of Co–N/CNFs (inset: SAED image).

(J) HAADF-STEM image and (K) EDX mapping of Co–N/CNFs. (L) AC-STEM image and (M) zoomed-in image of Co–N/CNFs (Cheng et al., 2017).

(N) Thermodynamic relations (volcano) lines for the two e^- (green solid line) and four e^- ORR (black solid line) (Sun et al., 2019c).

was amorphous carbon (Figures 15H and 15I). No obvious bright regions were observed in HAADF-STEM (Figure 15J), further indicating the absence of cobalt-containing particles. EDX mapping results showed that Co, N, and C were evenly distributed in CNFs (Figure 15K), and the Co corresponding to bright spots existed as a single atom in AC-HAADF-STEM (Figures 15L and 15M). The Co-N/CNFs displays desirable ORR performance and high stability with negligible decrease of $E_{1/2}$ after 10,000 CV cycles. Moreover, the catalyst as cathode reached a power density of 16 mW cm^{-2} and an outstanding stability with more than 200 h, showing the potential of application. What's more, a series of M-N-C materials (M = Mn, Fe, Co, Ni, and Cu) with atomically dispersed M-N_x sites were investigated the trends in electrochemical H_2O_2 production from molecular first principles to bench-scale electrolyzers operating at industrial current density (Sun et al., 2019c). Co-N-C catalyst showed outstanding ORR activity and selectivity to H_2O_2 and more than 4 mol peroxide $g_{catalyst}^{-1}$ h^{-1} at a current density of 50 mA cm^{-2}. The relationship of activity-selectivity and the trend of M-N-C materials was further analyzed by DFT calculations, providing a molecular scale understanding of the experimental volcanic trend of four-electron and two-electron ORR (Figure 15N). Meanwhile, the binding free energy of HO* intermediate placed Co-N-C close to the top of the two-electron volcano, retaining catalytic activity while promoting two-electron pathway selectivity.

Carbon dioxide reduction reaction

The increasing global environmental crisis has aroused people's attention to greenhouse gas emissions, conversion, and storage (Anagnostou et al., 2016; Mun et al., 2018; Obama, 2017). CO_2 is considered to be the main cause of the greenhouse effect. Electroreduction of CO_2 into high value-added products,

such as CO, HCOOH, CH_4, CH_3OH, C_2H_4, and so on, is a promising route, which can mitigate environmental problems. Because water acts as the medium of CO_2RR, HER inevitably becomes the side reaction of this reaction (Li et al., 2017; Yang et al., 2018a). Therefore, efficient catalysts in CO_2RR should reduce HER activity and enhance CO_2RR activity at the same time (Lin et al., 2019; Yan et al., 2018a).

Currently, the key obstacle to the development of efficient CO_2RR catalysts is the lack of a basic understanding of surface-mediated electrochemical reactions. There are many possible products in CO_2RR, involving electron transfer numbers ranging from CO ($2e^-$) and HCOOH ($2e^-$) to $CH_3CH_2CH_2OH$ ($18e^-$), so the interpretation of the reaction mechanism is more demanding (Lu and Jiao, 2016). Some typical multi-electron reactions in neutral medium are shown as follows:

$$CO_2(g) + 2H^+ + 2e^- \rightarrow CO(g) + H_2O \quad \text{(Equation 18)}$$

$$CO_2(g) + 2H^+ + 2e^- \rightarrow HCOOH(1) \quad \text{(Equation 19)}$$

$$CO_2(g) + 4H^+ + 2e^- \rightarrow HCOOH(1) + H_2O \quad \text{(Equation 20)}$$

$$CO_2(g) + 6H^+ + 6e^- \rightarrow CH_3OH(1) + H_2O \quad \text{(Equation 21)}$$

$$CO_2(g) + 8H^+ + 8e^- \rightarrow CH_4(g) + 2H_2O \quad \text{(Equation 22)}$$

SACs show high activity in many reactions with the highest atomic utilization rate, especially the unsaturated coordination between the central metal atom and the surrounding atoms, which significantly enhances the catalytic performance. Meanwhile, the uniform active site and geometry structure enhance the interaction between the mental centers and the support, which helps to improve the selectivity of the catalyst (Chen et al., 2018c). Therefore, SACs display great application potential in CO_2RR.

Reducing the coordination number between metal center and N leads to form unsaturated coordination, which is helpful to optimize the catalytic performance. Zhao and colleagues prepared Ni atoms anchoring on N-doped porous carbon with Ni-N_3 coordination by ZIF-assisted strategy for the first time in CO_2RR (Zhao et al., 2017) (Figure 16A). The SAC displayed outperforming current density of 10.48 mA cm^{-2} at an overpotential of 0.89 V with a high turnover frequency (TOF) of 5273 h^{-1} and Faradaic efficiency (FE) for CO production of over 71.9%. Besides, Zheng and colleagues fabricated an unsaturated coordination copper with nitrogen sites anchored into graphene matrix (Cu-N_2/GN) for CO_2RR to CO production (Zheng et al., 2019). The catalyst showed higher activity and selectivity with the maximum FE of 81% at a low potential of −0.50 V and an onset potential of −0.33 V than the atomically dispersed Cu-N anchored on carbon materials reported previously. From a practical point of view, the Cu-N_2/GN was applied in rechargeable Zn-CO_2 battery with a peak power density of 0.6 mW cm^{-2}, and the battery charging process can be powered by natural solar energy. Theoretical calculations showed that the moderate free energy of Cu-N_2 sites promote the adsorption of CO_2 molecules at the Cu-N_2 site (Figures 16B–16E). The adsorption state of H_2O, CO_2, COOH, and CO with Cu-N_2-based DFT electron density was hybridized with surface states of Cu-N_2 (Figures 16F–16I). The short bond length of Cu-N_2 sites caused the accelerated charge transfer from Cu-N_2 site to *CO_2, which enhanced effectively the formation of *COOH and CO_2RR performance. Adjustment of N coordination was also applicable for controlling the coordination environment of CO_2RR SACs. Bifunctional catalysis of Co and N co-doped hollow carbon for CO_2RR and HER has been reported (Song et al., 2018). The loading of Co single-atoms was around 3.4 wt%, and Co-C_2N_2 moieties acted as the major active sites during the process of CO_2 reduction. The catalyst was prepared through high temperature pyrolysis (900°C) to remain the high content of Co single atoms and prevent the loss of nitrogen. The Co-HNC possessed better catalysis performance than Co NP-SNC in 0.1 M $KHCO_3$ (Figure 16J). The Co-HNC showed a nearly 100% FE and high formation rate of around 425 mmol g^{-1} h^{-1} at 1.0 V, with the product ration of CO/H_2 approximating ideal 1/2 in the potential range from −0.7 to −1.0 V (Figure 16K). Meanwhile, the catalyst displayed the long-term stability for 24 h with negligible degradation of current density (Figure 16L) and the almost identical resistance to the Co NP-SNC (Figure 16M). Potassium thiocyanate (KSCN) poisoning experiment was carried out to confirm the selectively functioning of Co SAs and N-C groups for CO_2RR and HER. The CV curves and formation rate change were recorded in Figures 16N and 16O, which showed the gaseous products increased significantly but the CO selectivity of Co-HNC decreased sharply to 9.8%. What's more, the flow-cell electrolyzer effectively solves the limitation of CO_2 dissolution and diffusion in the traditional test device, realizing the highly selective conversion of CO_2 under the high current density and accelerating the industrial application of CO_2RR technology (Jin et al., 2021a). Yuan et al. designed single Cu atoms anchoring on the graphediyne (Yuan et al., 2022). *In situ* Raman and DFT calculations revealed that the presence of Cu-C bonds leads to the formation of CH_4, more facile during the process of CO_2RR. The catalyst also showed high activity and CH_4 FE and partial CH_4 current density in flow-cell electrolyzer.

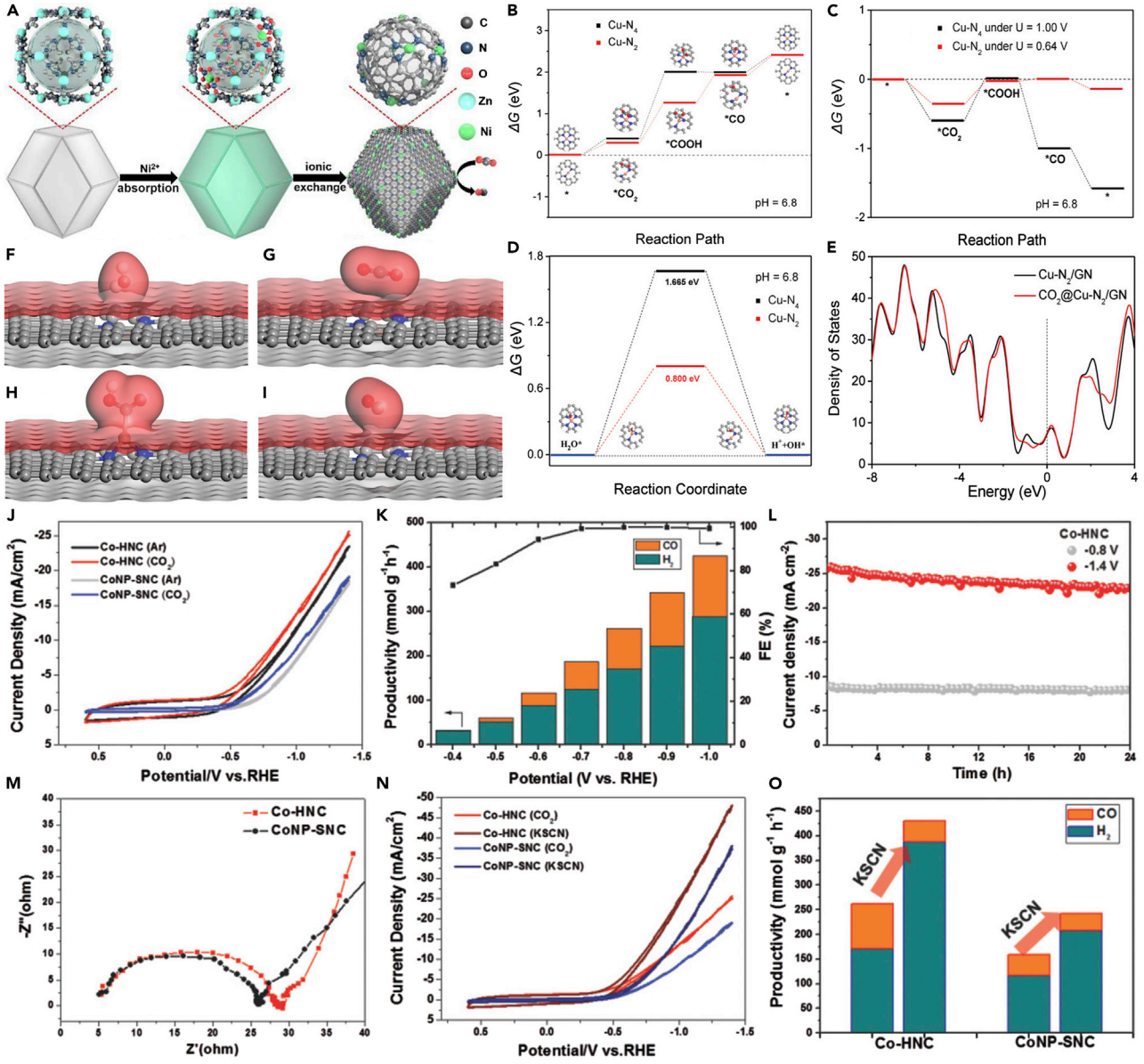

Figure 16. SACs for CO_2RR

(A) Illustration of the synthesis process of Ni SAs/N-C (Zhao et al., 2017).

(B) DFT-based free energy profile of the optimized Cu–N_2 and Cu–N_4 models in the CO_2ER.

(C) DFT-based free energy profile of the optimized Cu–N_2 and Cu–N_4 models in the CO_2ER under various applied voltages.

(D) DFT-based free energy profiles of water splitting.

(E) The density of states of Cu–N_2 without CO_2 adsorption and with CO_2 adsorption during the CO_2ER. The electron density of Cu–N_2 with (F) H_2O, (G) CO_2, (H) COOH, and (I) CO adsorptions based on DFT (Zheng et al., 2019).

(J) CV curves of Co-HNC and Co NP-SNC tested in 0.1 M $KHCO_3$ electrolyte saturated with Ar and CO_2.

(K) Dependence of Co-HNC productivity (left Y axis) and Co-HNC FE (right Y axis) on the applied potential. The orange and dark cyan bars represent CO and H_2, respectively.

(L) Durability test of Co-HNC at −0.8 V and −1.4 V.

(M) Nyquist plot of Co-HNC and Co NP-SNC.

(N) CV curves of Co-HNC and Co NP-SNC tested in 0.1 M $KHCO_3$-containing CO_2-saturated media with and without KSCN poisoning.

(O) Changes in the formation rate of Co-HNC and Co NP-SNC before and after KSCN poisoning (Song et al., 2018).

Nitrogen reduction reaction

Ammonia (NH_3) is not only a key raw material for main agricultural fertilizers but also shows important applications in chemical engineering and pharmaceutical and synthetic fiber fields (Galloway et al., 2004, 2008; Yang et al., 2020a; Zamfirescu and Dincer, 2008). Currently, the industrial synthesis of NH_3 commonly depends on the Haber-Bosch method under high temperature and pressure conditions (300–500°C, 15–30 MPa), consuming more than 1% of the global energy supply annually (Guo et al., 2018; Song et al., 2019; van der Ham et al., 2014a). Moreover, the thermodynamically limited conversion is only ~15%. Using N_2 as raw material, electrocatalytic nitrogen reduction reaction (NRR) realizes the synthesis of ammonia at room temperature and pressure, which exhibits the merits of low energy consumption and without pollution. It provides a green and low-carbon technical route for ammonia synthesis industry. NRR involves a $6e^-$ transfer process:

$$N_2(g) + 6H^+ + 6e^- \rightarrow 2NH_3(g) \quad \text{(Equation 23)}$$

However, the high bond energy of N≡N (940.95 kJ mol^{-1}) is a major obstacle to the NRR process, so it is necessary to develop efficient electrocatalysts, especially SACs, to reduce the reaction energy barrier and accelerate the generation of NH_3 (Chen et al., 2018b; van der Ham et al., 2014b; Wang et al., 2017). What's more, the adsorption of N_2 on the catalyst surface is usually not satisfactory, which is not conducive to the formation of intermediates and limits the selectivity and yield of NH_3 (Tao et al., 2019). Although many metal-based catalysts have been researched, most metals are too weakly bonded to achieve efficient N_2 adsorption and activation, which is generally considered a rate-limiting step for NRR. Meanwhile, NH_3 yield and faradaic efficiency (FE) are still far below the requirements of practical application.

Carbon-based-material-supported SACs show great application potential toward NRR due to the abundant exposed active sites and high catalytic activity. Single Ru atoms anchored on nitrogen-doped carbon (Ru SAs/N-C) were fabricated by facile pyrolysis method. The Ru SAs/N-C achieved a recorded-high activity in NRR, which possessed an FE of 29.6% for NH_3 production with partial current density of −0.13 mA cm^{-2} (Geng et al., 2018). More importantly, the yield of the SACs reaches 120.9 μg_{NH3} $mg_{cat.}^{-1}$ h^{-1}, well above the highest number ever reported (Figures 17A–17D). The stability of Ru SAs/N-C displayed less than 7% attenuation of NH_3 yield rate after 12 h potentiostatic measurement. DFT calculation showed that Ru SAs/N-C promoted N_2 dissociation, resulting in increased activity relative to Ru NPs/N-C. In addition to noble metals, non-noble-metal SACs have also been studied in NRR. Copper single atoms attached in porous N-doped carbon network (Cu SAC) with Cu-N_2 active sites as pH-universal catalyst showed outstanding NH_3 yield rate and FE under 0.1 M KOH and 0.1 M HCl conditions (Figures 17E–17H) (Zang et al., 2019). Meanwhile, the Cu SAC also displayed excellent stability over 12 h with little current attenuation. The combination of experiment and first-principles calculations revealed that Cu-N_2 coordination acts the effective active sites in NRR catalysis.

CONCLUSION AND OUTLOOK

Up to now, SACs have attracted extensive research interests in a wide range of catalytic fields, including photocatalysis, organic catalysis, electrocatalysis, and environmental aspect. The primary target of the rapid-developing SACs field is reducing the using of precious metals while keeping the catalytic activity. Carbon-based-material-supported SACs display great application prospect because of its low cost, high efficiency, and robustness. In this review, we introduced the synthesis methods and the advanced characterization techniques used in the identification of SACs, mainly concerning X-ray-derived spectroscopy and *in situ* techniques, which showed important guiding significance for coordination regulation and coordination environment recognition of SACs. In addition, the applications of carbon-based-material-supported SACs were discussed in electrocatalysis fields, including HER, OER, ORR, CO_2RR, and NRR. To date, some progress has been made in enhancing catalytic performance of SACs. However, there are still many opportunities and challenges for the prospect of single atoms in the future.

Firstly, the low loading of single atom in the SACs prepared by the existing synthesis strategies restricts the development of SACs. The sluggish reaction kinetics need to be overcome through exposing more active sites in catalysis. Low loading SACs may lead to the accumulation of intermediates during the reaction process, resulting in side reactions and reduced selectivity, which is not suitable for industrial scale applications. However, when the metal atom loading increases, the migration and agglomeration of single atoms tends to form nanoclusters or nanoparticles due to its high surface free energy. Therefore, it is imperative to develop SACs with high loading active sites for industrial production. In addition, it is very essential to study

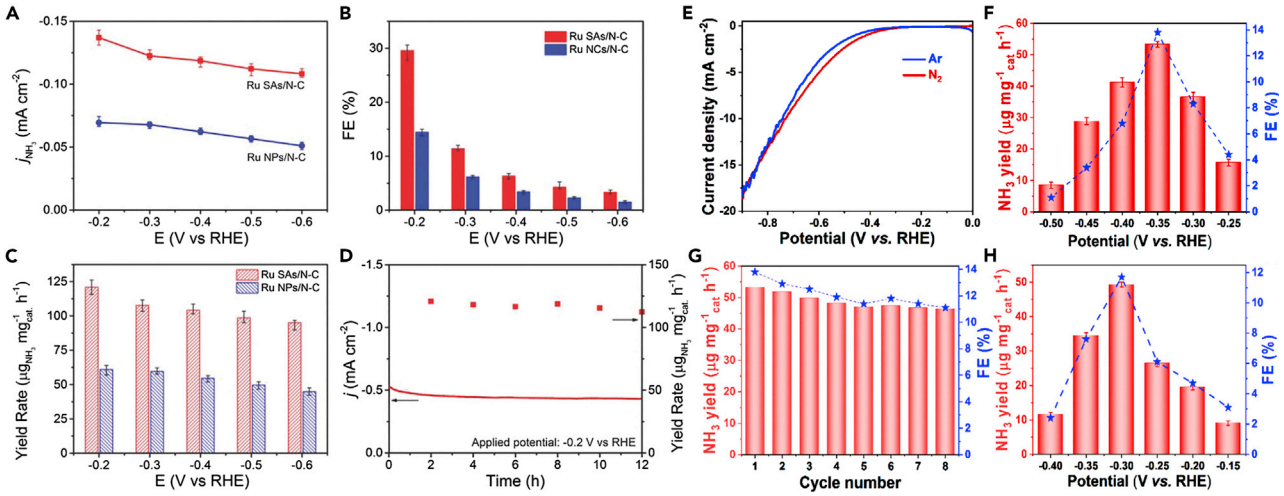

Figure 17. SACs for NRR

(A) Current densities diagram, (B) FE diagram, and (C) yield rate diagram for NH_3 production at different potentials on Ru SAs/N-C and Ru NPs/N-C, respectively.

(D) Stability test for Ru SAs/N-C at −0.2 V versus RHE (Geng et al., 2018).

(E) LSV curves in N_2-saturated and Ar-saturated basic solution.

(F) Yield rate and FE at different applied potentials in basic solution.

(G) Yield rates of NH_3 with increasing cycle numbers in basic solution.

(H) Yield rate and FE at different applied potentials in acid solution (Zang et al., 2019).

the interaction between metal single atoms and support, because the support shows an effect on the loading and electronic structure of single atom. For example, Xia and colleagues used graphene quantum dots as carbon substrates, which were modified with -NH_2 groups to improve the coordination activity for metal ions (Xia et al., 2021). The as-prepared transition metal single-atom material achieved a loading of up to 40 wt% and excellent thermal stability. Besides carbon-based materials, two-dimensional material transition metals, such as the sulfides, selenides, phosphides, and so on, have also been studied as carriers for SACs. The electron transfer between metal and carrier can be directly regulated by electronic metal-support interaction (EMSI), thereby regulating the electronic state of the supported metal. Therefore, it is of significance to develop the novel supports of SACs with superior catalytic performance for energy conversions.

Secondly, the coordination environments show a great influence on the electronic and geometric structure of the central metal atoms, which plays an important role in the catalytic properties of SACs. Nonmetal heteroatomic doping (N, O, S, P, etc.) is one of the main strategies to regulate coordination environments. However, other elements, such as SE, Te, and halogen elements, are rarely studied and may display unexpected catalytic properties. In addition, the asymmetric distribution of charges may lead to superior performance. Thus, it is imperative to study the dual or more metal center sites. In a word, rationally constructing coordination environments of SACs is significant to boost the catalytic activity, which provides a direct way to understand the intrinsic activity of SACs.

Thirdly, the characterization techniques are the significant fundament for the recognition of SACs. At present, the identification of coordination environments relies heavily on XAS, whereas the technique is bulk sensitive and only provides bulk average information. Therefore, it is very important to improve the spatial resolution of characterization technology. Furthermore, in order to determine the active sites of SACs and dynamic changes during the reaction, it is necessary to combine *in situ* characterization techniques. The dynamic changes of coordination structures and oxidation states of SACs during the catalytic process is worthy of further exploration because it is closely related to intrinsic activity.

Finally, the step process and reaction mechanism of single-atom catalytic reaction are still in the preliminary exploration stage. Constructing a reliable structure-activity relationship of catalytic reactions is crucial for designing high-performance SACs. Theoretical simulation is conducive to understanding the structure-activity

relationship of catalysts at atomic level. DFT calculation is a powerful tool to explore the atomic structure and intrinsic active sites. In addition, the reaction free energy of each elementary step and the adsorption energies of the intermediates can be obtained from DFT calculation, which is of great significance to the understanding of reaction mechanism. However, some of the proposed mechanisms do not match well with experimental results. More accurate models should be developed to reflect rational catalytic processes. What's more, DFT calculation combined with machine learning can predict efficient SACs, which shows a positive effect on the prospect of electrocatalysis. We believe that this work can promote the development of single-atom catalysis and deepen readers' understanding of single atoms.

ACKNOWLEDGMENTS

This work is supported by the National Key Research and Development Program of China (2021YFA1500500), National Natural Science Foundation of China (Grant Nos. 21822801 and 22005025), and China Postdoctoral Science Foundation (2021M700352).

AUTHOR CONTRIBUTIONS

D. Cao and D.J. Cheng supervised the preparation of this review article. D. Cao, D.J. Cheng and H.M. Zhang conceived the topic. H.M. Zhang contributed to the most of the writing, and W.H. Liu contributed to some content and figures. H.M. Zhang and W.H. Liu revised the manuscript. D. Cao and D.J. Cheng revised and finalized the manuscript. All author approved the final version of the manuscript.

DECLARATION OF INTERESTS

The authors declare no competing interests.

REFERENCES

Abbet, S., Sanchez, A., Heiz, U., Schneider, W.-D., Ferrari, A.M., Pacchioni, G., and Rösch, N. (2000). Acetylene cyclotrimerization on supported size-selected Pd_n clusters ($1 \leq n \leq 30$): one atom is enough. J. Am. Chem. Soc. *122*, 3453–3457. https://doi.org/10.1021/ja9922476.

Amiinu, I.S., Liu, X., Pu, Z., Li, W., Li, Q., Zhang, J., Tang, H., Zhang, H., and Mu, S. (2018). From 3D ZIF nanocrystals to Co-N_x/C nanorod array electrocatalysts for ORR, OER, and Zn-air batteries. Adv. Funct. Mater. *28*, 1704638. https://doi.org/10.1002/adfm.201704638.

An, H., Wu, L., Mandemaker, L.D.B., Yang, S., de Ruiter, J., Wijten, J.H.J., Janssens, J.C.L., Hartman, T., van der Stam, W., and Weckhuysen, B.M. (2021). Sub-second time-resolved surface-enhanced Raman spectroscopy reveals dynamic CO intermediates during electrochemical CO_2 reduction on copper. Angew. Chem. Int. Ed. Engl. *60*, 16576–16584. https://doi.org/10.1002/ange.202104114.

Anagnostou, E., John, E.H., Edgar, K.M., Foster, G.L., Ridgwell, A., Inglis, G.N., Pancost, R.D., Lunt, D.J., and Pearson, P.N. (2016). Changing atmospheric CO_2 concentration was the primary driver of early Cenozoic climate. Nature *533*, 380–384. https://doi.org/10.1038/nature17423.

Bockris, J.O.M., and Potter, E.C. (1952). The mechanism of the cathodic hydrogen evolution reaction. J. Electrochem. Soc. *99*, 169. https://doi.org/10.1149/1.2779692.

Cao, L., and Lu, J. (2020). Atomic-scale engineering of metal–oxide interfaces for advanced catalysis using atomic layer deposition. Catal. Sci. Technol. *10*, 2695–2710. https://doi.org/10.1039/d0cy00304b.

Cao, L., Luo, Q., Chen, J., Wang, L., Lin, Y., Wang, H., Liu, X., Shen, X., Zhang, W., Liu, W., et al. (2019). Dynamic oxygen adsorption on single-atomic Ruthenium catalyst with high performance for acidic oxygen evolution reaction. Nat. Commun. *10*, 4849. https://doi.org/10.1038/s41467-019-12886-z.

Cao, D., Wang, J., Xu, H., and Cheng, D. (2021). Construction of dual-site atomically dispersed electrocatalysts with Ru-C_5 single atoms and Ru-O_4 nanoclusters for accelerated alkali hydrogen evolution. Small *17*, e2101163. https://doi.org/10.1002/smll.202101163.

Chen, W., Pei, J., He, C.T., Wan, J., Ren, H., Zhu, Y., Wang, Y., Dong, J., Tian, S., Cheong, W.C., et al. (2017a). Rational design of single molybdenum atoms anchored on N-doped carbon for effective hydrogen evolution reaction. Angew. Chem. Int. Ed. Engl. *56*, 16086–16090. https://doi.org/10.1002/ange.201710599.

Chen, Y., Ji, S., Wang, Y., Dong, J., Chen, W., Li, Z., Shen, R., Zheng, L., Zhuang, Z., Wang, D., and Li, Y. (2017b). Isolated single iron atoms anchored on N-doped porous carbon as an efficient electrocatalyst for the oxygen reduction reaction. Angew. Chem. Int. Ed. Engl. *56*, 6937–6941. https://doi.org/10.1002/ange.201702473.

Chen, W., Pei, J., He, C.T., Wan, J., Ren, H., Wang, Y., Dong, J., Wu, K., Cheong, W.C., Mao, J., et al. (2018a). Single tungsten atoms supported on MOF-derived N-doped carbon for robust electrochemical hydrogen evolution. Adv. Mater. *30*, e1800396. https://doi.org/10.1002/adma.201800396.

Chen, X., Li, N., Kong, Z., Ong, W.-J., and Zhao, X. (2018b). Photocatalytic fixation of nitrogen to ammonia: state-of-the-art advancements and future prospects. Mater. Horiz. *5*, 9–27. https://doi.org/10.1039/c7mh00557a.

Chen, Y., Ji, S., Chen, C., Peng, Q., Wang, D., and Li, Y. (2018c). Single-atom catalysts: synthetic strategies and electrochemical applications. Joule *2*, 1242–1264. https://doi.org/10.1016/j.joule.2018.06.019.

Chen, R., Hung, S.F., Zhou, D., Gao, J., Yang, C., Tao, H., Yang, H.B., Zhang, L., Zhang, L., Xiong, Q., et al. (2019). Layered structure causes bulk NiFe layered double hydroxide unstable in alkaline oxygen evolution reaction. Adv. Mater. *31*, e1903909. https://doi.org/10.1002/adma.201903909.

Chen, F.-Y., Wu, Z.-Y., Adler, Z., and Wang, H. (2021). Stability challenges of electrocatalytic oxygen evolution reaction: from mechanistic understanding to reactor design. Joule *5*, 1704–1731. https://doi.org/10.1016/j.joule.2021.05.005.

Cheng, N., Stambula, S., Wang, D., Banis, M.N., Liu, J., Riese, A., Xiao, B., Li, R., Sham, T.K., Liu, L.M., et al. (2016). Platinum single-atom and cluster catalysis of the hydrogen evolution reaction. Nat. Commun. *7*, 13638. https://doi.org/10.1038/ncomms13638.

Cheng, Q., Yang, L., Zou, L., Zou, Z., Chen, C., Hu, Z., and Yang, H. (2017). Single cobalt atom and N codoped carbon nanofibers as highly durable electrocatalyst for oxygen reduction reaction. ACS Catal. *7*, 6864–6871. https://doi.org/10.1021/acscatal.7b02326.

Cheng, Y., Zhao, S., Johannessen, B., Veder, J.P., Saunders, M., Rowles, M.R., Cheng, M., Liu, C., Chisholm, M.F., De Marco, R., et al. (2018). Atomically dispersed transition metals on carbon nanotubes with ultrahigh loading for selective

electrochemical carbon dioxide reduction. Adv. Mater. *30*, e1706287. https://doi.org/10.1002/adma.201706287.

Cialla, D., März, A., Böhme, R., Theil, F., Weber, K., Schmitt, M., and Popp, J. (2012). Surface-enhanced Raman spectroscopy (SERS): progress and trends. Anal. Bioanal. Chem. *403*, 27–54. https://doi.org/10.1007/s00216-011-5631-x.

Conway, B.E., and Tilak, B.V. (2002). Interfacial processes involving electrocatalytic evolution and oxidation of H_2, and the role of chemisorbed H. Electrochim. Acta *47*, 3571–3594. https://doi.org/10.1016/s0013-4686(02)00329-8.

Cook, S.A., and Borovik, A.S. (2015). Molecular designs for controlling the local environments around metal ions. Acc. Chem. Res. *48*, 2407–2414. https://doi.org/10.1021/acs.accounts.5b00212.

Cui, X., Li, H., Wang, Y., Hu, Y., Hua, L., Li, H., Han, X., Liu, Q., Yang, F., He, L., et al. (2018). Room-temperature methane conversion by graphene-confined single iron atoms. Chem *4*, 1902–1910. https://doi.org/10.1016/j.chempr.2018.05.006.

Deng, D., Chen, X., Yu, L., Wu, X., Liu, Q., Liu, Y., Yang, H., Tian, H., Hu, Y., Du, P., et al. (2015). A single iron site confined in a graphene matrix for the catalytic oxidation of benzene at room temperature. Sci. Adv. *1*, e1500462. https://doi.org/10.1126/sciadv.1500462.

Deng, Y., Dong, Y., Wang, G., Sun, K., Shi, X., Zheng, L., Li, X., and Liao, S. (2017). Well-defined ZIF-derived Fe-N codoped carbon nanoframes as efficient oxygen reduction catalysts. ACS Appl. Mater. Inter. *9*, 9699–9709. https://doi.org/10.1021/acsami.6b16851.

Ding, S.-Y., Yi, J., Li, J.-F., Ren, B., Wu, D.-Y., Panneerselvam, R., and Tian, Z.-Q. (2016). Nanostructure-based plasmon-enhanced Raman spectroscopy for surface analysis of materials. Nat. Rev. Mater. *1*, 16021. https://doi.org/10.1038/natrevmats.2016.21.

Drosos, C., and Vernardou, D. (2018). Advancements, Challenges and prospects of chemical vapour pressure at atmospheric pressure on vanadium dioxide structures. Materials *11*, 384. https://doi.org/10.3390/ma11030384.

Feng, Y., Guan, Y., Zhang, H., Huang, Z., Li, J., Jiang, Z., Gu, X., and Wang, Y. (2018). Selectively anchoring Pt single atoms at hetero-interfaces of γ-Al_2O_3/NiS to promote the hydrogen evolution reaction. J. Mater. Chem. A *6*, 11783–11789. https://doi.org/10.1039/c8ta02556h.

Fu, Q., Saltsburg, H., and Flytzani-Stephanopoulos, M. (2003). Active nonmetallic Au and Pt species on ceria-based water-gas shift catalysts. Science *301*, 935–938. https://doi.org/10.1126/science.1085721.

Fu, N., Liang, X., Li, Z., Chen, W., Wang, Y., Zheng, L., Zhang, Q., Chen, C., Wang, D., Peng, Q., et al. (2020). Fabricating Pd isolated single atom sites on C_3N_4/rGO for heterogenization of homogeneous catalysis. Nano Res. *13*, 947–951. https://doi.org/10.1007/s12274-020-2720-1.

Galloway, J.N., Dentener, F.J., Capone, D.G., Boyer, E.W., Howarth, R.W., Seitzinger, S.P., Asner, G.P., Cleveland, C.C., Green, P.A., Holland, E.A., et al. (2004). Nitrogen cycles: past, present, and future. Biogeochemistry *70*, 153–226. https://doi.org/10.1007/s10533-004-0370-0.

Galloway, J.N., Townsend, A.R., Erisman, J.W., Bekunda, M., Cai, Z., Freney, J.R., Martinelli, L.A., Seitzinger, S.P., and Sutton, M.A. (2008). Transformation of the nitrogen cycle: recent trends, questions, and potential solutions. Science *320*, 889–892. https://doi.org/10.1126/science.1136674.

Gardecka, A.J., Bishop, C., Lee, D., Corby, S., Parkin, I.P., Kafizas, A., and Krumdieck, S. (2018). High efficiency water splitting photoanodes composed of nano-structured anatase-rutile TiO_2 heterojunctions by pulsed-pressure MOCVD. Appl. Catal. B Environ. *224*, 904–911. https://doi.org/10.1016/j.apcatb.2017.11.033.

Geng, Z., Liu, Y., Kong, X., Li, P., Li, K., Liu, Z., Du, J., Shu, M., Si, R., and Zeng, J. (2018). Achieving a record-high yield rate of 120.9 μg_{NH3} $mg_{cat.}^{-1}$ h^{-1} for N_2 electrochemical reduction over Ru single-atom catalysts. Adv. Mater. *30*, e1803498. https://doi.org/10.1002/adma.201803498.

Georgakilas, V., Perman, J.A., Tucek, J., and Zboril, R. (2015). Broad family of carbon nanoallotropes: classification, chemistry, and applications of fullerenes, carbon dots, nanotubes, graphene, nanodiamonds, and combined superstructures. Chem. Rev. *115*, 4744–4822. https://doi.org/10.1021/cr500304f.

George, S.M. (2010). Atomic layer deposition: an overview. Chem. Rev. *110*, 111–131. https://doi.org/10.1021/cr900056b.

Gong, Q., Wang, Y., Hu, Q., Zhou, J., Feng, R., Duchesne, P.N., Zhang, P., Chen, F., Han, N., Li, Y., et al. (2016). Ultrasmall and phase-pure W_2C nanoparticles for efficient electrocatalytic and photoelectrochemical hydrogen evolution. Nat. Commun. *7*, 13216–13218. https://doi.org/10.1038/ncomms13216.

Grimaud, A., Diaz-Morales, O., Han, B., Hong, W.T., Lee, Y.L., Giordano, L., Stoerzinger, K.A., Koper, M.T.M., and Shao-Horn, Y. (2017). Activating lattice oxygen redox reactions in metal oxides to catalyse oxygen evolution. Nat. Chem. *9*, 457–465. https://doi.org/10.1038/nchem.2695.

Guo, C., Ran, J., Vasileff, A., and Qiao, S.-Z. (2018). Rational design of electrocatalysts and photo(electro)catalysts for nitrogen reduction to ammonia (NH_3) under ambient conditions. Energy Environ. Sci. *11*, 45–56. https://doi.org/10.1039/c7ee02220d.

Guo, J., Zhang, W., Zhang, L.-H., Chen, D., Zhan, J., Wang, X., Shiju, N.R., and Yu, F. (2021). Control over electrochemical CO_2 reduction selectivity by coordination engineering of tin single-atom catalysts. Adv. Sci. *8*, 2102884. https://doi.org/10.1002/advs.202102884.

Hackett, S.F., Brydson, R.M., Gass, M.H., Harvey, I., Newman, A.D., Wilson, K., and Lee, A.F. (2007). High-activity, single-site mesoporous Pd/Al_2O_3 catalysts for selective aerobic oxidation of allylic alcohols. Angew. Chem. *119*, 8747–8750. https://doi.org/10.1002/ange.200702534.

Han, G., Zheng, Y., Zhang, X., Wang, Z., Gong, Y., Du, C., Banis, M.N., Yiu, Y.-M., Sham, T.-K., Gu, L., et al. (2019a). High loading single-atom Cu dispersed on graphene for efficient oxygen reduction reaction. Nano Energy *66*, 104088. https://doi.org/10.1016/j.nanoen.2019.104088.

Han, X., Ling, X., Yu, D., Xie, D., Li, L., Peng, S., Zhong, C., Zhao, N., Deng, Y., and Hu, W. (2019b). Atomically dispersed binary Co-Ni Sites in Nitrogen-doped hollow carbon nanocubes for reversible oxygen reduction and evolution. Adv. Mater. *31*. e1905622. https://doi.org/10.1002/adma.201905622.

Hao, S., Sheng, H., Liu, M., Huang, J., Zheng, G., Zhang, F., Liu, X., Su, Z., Hu, J., Qian, Y., et al. (2021). Torsion strained iridium oxide for efficient acidic water oxidation in proton exchange membrane electrolyzers. Nat. Nanotechnol. *16*, 1371–1377. https://doi.org/10.1038/s41565-021-00986-1.

Hu, H., Guan, W., Xu, Y., Wang, X., Wu, L., Chen, M., Zhong, Q., Xu, Y., Li, Y., Sham, T.K., et al. (2021). Construction of single-atom platinum catalysts enabled by $CsPbBr_3$ nanocrystals. ACS Nano *15*, 13129–13139. https://doi.org/10.1021/acsnano.1c02515.

Huang, Z.-F., Song, J., Du, Y., Xi, S., Dou, S., Nsanzimana, J.M.V., Wang, C., Xu, Z.J., and Wang, X. (2019). Chemical and structural origin of lattice oxygen oxidation in Co–Zn oxyhydroxide oxygen evolution electrocatalysts. Nat. Energy *4*, 329–338. https://doi.org/10.1038/s41560-019-0355-9.

Jiang, Z., Sun, W., Shang, H., Chen, W., Sun, T., Li, H., Dong, J., Zhou, J., Li, Z., Wang, Y., et al. (2019). Atomic interface effect of a single atom copper catalyst for enhanced oxygen reduction reactions. Energy Environ. Sci. *12*, 3508–3514. https://doi.org/10.1039/c9ee02974e.

Jiang, K., Luo, M., Peng, M., Yu, Y., Lu, Y.-R., Chan, T.-S., Liu, P., de Groot, F.M.F., and Tan, Y. (2020). Dynamic active-site generation of atomic iridium stabilized on nanoporous metal phosphides for water oxidation. Nat. Commun. *11*, 2701. https://doi.org/10.1038/s41467-020-16558-1.

Jin, S., Hao, Z., Zhang, K., Yan, Z., and Chen, J. (2021a). Advances and challenges for the electrochemical reduction of CO_2 to CO: from fundamentals to industrialization. Angew. Chem. Int. Ed. Engl. *60*, 20627–20648. https://doi.org/10.1002/ange.202101818.

Jin, T., Liu, X., Gao, Q., Zhu, H., Lian, C., Wang, J., Wu, R., and Lyu, Y. (2021b). Pyrolysis-free, facile mechanochemical strategy toward cobalt single-atom/nitrogen-doped carbon for highly efficient water splitting. Chem. Eng. J. https://doi.org/10.1016/j.cej.2021.134089.

Kettner, M., Maisel, S., Stumm, C., Schwarz, M., Schuschke, C., Görling, A., and Libuda, J. (2019). Pd-Ga model SCALMS: characterization and stability of Pd single atom sites. J. Catal. *369*, 33–46. https://doi.org/10.1016/j.jcat.2018.10.027.

King, J.S., Wittstock, A., Biener, J., Kucheyev, S.O., Wang, Y.M., Baumann, T.F., Giri, S.K., Hamza, A.V., Baeumer, M., and Bent, S.F. (2008). Ultralow loading Pt nanocatalysts prepared by atomic layer deposition on carbon aerogels. Nano Lett. *8*, 2405–2409. https://doi.org/10.1021/nl801299z.

Kötz, R., Stucki, S., Scherson, D., and Kolb, D.M. (1984). In-situ identification of RuO_4 as the

corrosion product during oxygen evolution on ruthenium in acid media. J. Electroanal. Chem. Inter. Electrochem. *172*, 211–219. https://doi.org/10.1016/0022-0728(84)80187-4.

Kreuter, W., and Hofmann, H. (1998). Electrolysis: the important energy transformer in a world of sustainable energy. Int. J. Hydrogen Energy *23*, 661–666. https://doi.org/10.1016/s0360-3199(97)00109-2.

Lang, R., Xi, W., Liu, J.-C., Cui, Y.-T., Li, T., Lee, A.F., Chen, F., Chen, Y., Li, L., Li, L., et al. (2019). Non defect-stabilized thermally stable single-atom catalyst. Nat. Commun. *10*, 234–243. https://doi.org/10.1038/s41467-018-08136-3.

Lasia, A. (2010). Hydrogen evolution reaction. In Handbook of Fuel Cells, *2*, pp. 416–440.

Li, G., Li, Y., Liu, H., Guo, Y., Li, Y., and Zhu, D. (2010). Architecture of graphdiyne nanoscale films. Chem. Commun. (Camb) *46*, 3256–3258. https://doi.org/10.1039/b922733d.

Li, W., Zhang, L.-S., Wang, Q., Yu, Y., Chen, Z., Cao, C.-Y., and Song, W.-G. (2012). Low-cost synthesis of graphitic carbon nanofibers as excellent room temperature sensors for explosive gases. J. Mater. Chem. *22*, 15342. https://doi.org/10.1039/c2jm32031b.

Li, J.F., Tian, X.D., Li, S.B., Anema, J.R., Yang, Z.L., Ding, Y., Wu, Y.F., Zeng, Y.M., Chen, Q.Z., Ren, B., et al. (2013). Surface analysis using shell-isolated nanoparticle-enhanced Raman spectroscopy. Nat. Protoc. *8*, 52–65. https://doi.org/10.1038/nprot.2012.141.

Li, Y., Xu, L., Liu, H., and Li, Y. (2014). Graphdiyne and graphyne: from theoretical predictions to practical construction. Chem. Soc. Rev. *43*, 2572–2586. https://doi.org/10.1039/c3cs60388a.

Li, Y., Wang, J., Tian, X., Ma, L., Dai, C., Yang, C., and Zhou, Z. (2016). Carbon doped molybdenum disulfide nanosheets stabilized on graphene for the hydrogen evolution reaction with high electrocatalytic ability. Nanoscale *8*, 1676–1683. https://doi.org/10.1039/c5nr07370g.

Li, X., Bi, W., Chen, M., Sun, Y., Ju, H., Yan, W., Zhu, J., Wu, X., Chu, W., Wu, C., and Xie, Y. (2017). Exclusive Ni-N_4 sites realize near-unity CO selectivity for electrochemical CO_2 reduction. J. Am. Chem. Soc. *139*, 14889–14892. https://doi.org/10.1021/jacs.7b09074.

Li, D., Jia, Y., Chang, G., Chen, J., Liu, H., Wang, J., Hu, Y., Xia, Y., Yang, D., and Yao, X. (2018). A defect-driven metal-free electrocatalyst for oxygen reduction in acidic electrolyte. Chem *4*, 2345–2356. https://doi.org/10.1016/j.chempr.2018.07.005.

Li, W., Chu, X.-s., Wang, F., Dang, Y.-y., Liu, X.-y., Ma, T.-h., Li, J.-y., and Wang, C.-y. (2022). Pd single-atom decorated CdS nanocatalyst for highly efficient overall water splitting under simulated solar light. Appl. Catal. B: Environ. *304*, 121000. https://doi.org/10.1016/j.apcatb.2021.121000.

Liang, Z., Guo, W., Zhao, R., Qiu, T., Tabassum, H., and Zou, R. (2019). Engineering atomically dispersed metal sites for electrocatalytic energy conversion. Nano Energy *64*, 103917. https://doi.org/10.1016/j.nanoen.2019.103917.

Lin, J., Peng, Z., Wang, G., Zakhidov, D., Larios, E., Yacaman, M.J., and Tour, J.M. (2014). Enhanced electrocatalysis for hydrogen evolution reactions from WS_2 nanoribbons. Adv. Energy Mater. *4*, 1301875. https://doi.org/10.1002/aenm.201301875.

Lin, L., Li, H., Yan, C., Li, H., Si, R., Li, M., Xiao, J., Wang, G., and Bao, X. (2019). Synergistic catalysis over iron-nitrogen sites anchored with cobalt phthalocyanine for efficient CO_2 electroreduction. Adv. Mater. *31*, e1903470. https://doi.org/10.1002/adma.201903470.

Liu, C., Wang, C.-C., Kei, C.-C., Hsueh, Y.-C., and Perng, T.-P. (2009). Atomic layer deposition of platinum nanoparticles on carbon nanotubes for application in proton-exchange membrane fuel cells. Small *5*, 1535–1538. https://doi.org/10.1002/smll.200900278.

Liu, J., Jiao, M., Lu, L., Barkholtz, H.M., Li, Y., Wang, Y., Jiang, L., Wu, Z., Liu, D.J., Zhuang, L., et al. (2017). High performance platinum single atom electrocatalyst for oxygen reduction reaction. Nat. Commun. *8*, 15938. https://doi.org/10.1038/ncomms15938.

Liu, X., Wang, L., Yu, P., Tian, C., Sun, F., Ma, J., Li, W., and Fu, H. (2018). A stable bifunctional catalyst for rechargeable zinc-air batteries: iron-cobalt nanoparticles embedded in a nitrogen-doped 3D carbon matrix. Angew. Chem. Int. Ed. Engl. *57*, 16166–16170. https://doi.org/10.1002/ange.201809009.

Liu, J., Jin, Z., Wang, X., Ge, J., Liu, C., and Xing, W. (2019a). Recent advances in active sites identification and regulation of M-N/C electrocatalysts towards ORR. Sci. China Chem. *62*, 669–683. https://doi.org/10.1007/s11426-018-9425-5.

Liu, X., Cao, L., Guo, Z., Li, Y., Gao, W., and Zhou, L. (2019b). A review of perovskite photovoltaic materials' synthesis and applications via chemical vapor deposition method. Materials *12*, 3304. https://doi.org/10.3390/ma12203304.

Liu, C., Li, H., Liu, F., Chen, J., Yu, Z., Yuan, Z., Wang, C., Zheng, H., Henkelman, G., Wei, L., and Chen, Y. (2020). Intrinsic activity of metal centers in metal–nitrogen–carbon single-atom catalysts for hydrogen peroxide synthesis. J. Am. Chem. Soc. *142*, 21861–21871. https://doi.org/10.1021/jacs.0c10636.

Liu, W., Cao, D., and Cheng, D. (2021). Review on synthesis and catalytic coupling mechanism of highly active electrocatalysts for water splitting. Energy Technol. *9*, 2000855. https://doi.org/10.1002/ente.202000855.

Lu, Q., and Jiao, F. (2016). Electrochemical CO_2 reduction: electrocatalyst, reaction mechanism, and process engineering. Nano Energy *29*, 439–456. https://doi.org/10.1016/j.nanoen.2016.04.009.

Lukowski, M.A., Daniel, A.S., English, C.R., Meng, F., Forticaux, A., Hamers, R.J., and Jin, S. (2014). Highly active hydrogen evolution catalysis from metallic WS_2 nanosheets. Energy Environ. Sci. *7*, 2608–2613. https://doi.org/10.1039/c4ee01329h.

Ma, Y., Zhang, X., Cao, L., and Lu, J. (2021). Effects of the morphology and heteroatom doping of CeO2 support on the hydrogenation activity of Pt single-atoms. Catal. Sci. Technol. *11*, 2844–2851. https://doi.org/10.1039/d0cy02279a.

Malarde, D., Powell, M.J., Quesada-Cabrera, R., Wilson, R.L., Carmalt, C.J., Sankar, G., Parkin, I.P., and Palgrave, R.G. (2017). Optimized atmospheric-pressure chemical vapor deposition thermochromic VO_2 thin films for intelligent window applications. ACS Omega *2*, 1040–1046. https://doi.org/10.1021/acsomega.7b00042.

Man, I.C., Su, H.-Y., Calle-Vallejo, F., Hansen, H.A., Martínez, J.I., Inoglu, N.G., Kitchin, J., Jaramillo, T.F., Nørskov, J.K., and Rossmeisl, J. (2011). Universality in oxygen evolution electrocatalysis on oxide surfaces. ChemCatChem *3*, 1159–1165. https://doi.org/10.1002/cctc.201000397.

Mao, J., Li, J., Pei, J., Liu, Y., Wang, D., and Li, Y. (2019). Structure regulation of noble-metal-based nanomaterials at an atomic level. Nano Today *26*, 164–175. https://doi.org/10.1016/j.nantod.2019.03.008.

Marichy, C., Bechelany, M., and Pinna, N. (2012). Atomic layer deposition of nanostructured materials for energy and environmental applications. Adv. Mater. *24*, 1017–1032. https://doi.org/10.1002/adma.201104129.

Marković, N.M., and Ross, P.N. (2002). Surface science studies of model fuel cell electrocatalysts. Surf. Sci. Rep. *45*, 117–229. https://doi.org/10.1016/s0167-5729(01)00022-x.

Maschmeyer, T., Rey, F., Sankar, G., and Thomas, J.M. (1995). Heterogeneous catalysts obtained by grafting metallocene complexes onto mesoporous silica. Nature *378*, 159–162. https://doi.org/10.1038/378159a0.

Merki, D., and Hu, X. (2011). Recent developments of molybdenum and tungsten sulfides as hydrogen evolution catalysts. Energy Environ. Sci. *4*, 3878–3888. https://doi.org/10.1039/c1ee01970h.

Mun, Y., Kim, K., Kim, S., Lee, S., Lee, S., Kim, S., Choi, W., Kim, S.-k., Han, J.W., and Lee, J. (2018). A novel strategy to develop non-noble metal catalyst for CO_2 electroreduction: hybridization of metal-organic polymer. Appl. Catal. B Environ. *236*, 154–161. https://doi.org/10.1016/j.apcatb.2018.05.025.

Nørskov, J.K., Bligaard, T., Logadottir, A., Kitchin, J.R., Chen, J.G., Pandelov, S., and Stimming, U. (2005). Trends in the exchange current for hydrogen evolution. J. Electrochem. Soc. *152*, J23. https://doi.org/10.1149/1.1856988.

Nørskov, J.K., Rossmeisl, J., Logadottir, A., Lindqvist, L., Kitchin, J.R., Bligaard, T., and Jonsson, H. (2004). Origin of the overpotential for oxygen reduction at a fuel-cell cathode. J. Phys. Chem. B *108*, 17886–17892. https://doi.org/10.1021/jp047349j.

Obama, B. (2017). The irreversible momentum of clean energy. Science *355*, 126–129. https://doi.org/10.1126/science.aam6284.

Pan, F., Jin, J., Fu, X., Liu, Q., and Zhang, J. (2013). Advanced oxygen reduction electrocatalyst based on nitrogen-doped graphene derived from edible sugar and urea. ACS Appl. Mater. Inter. *5*, 11108–11114. https://doi.org/10.1021/am403340f.

Pan, Y., Xu, X., Zhong, Y., Ge, L., Chen, Y., Veder, J.P.M., Guan, D., O'Hayre, R., Li, M., Wang, G., et al. (2020). Direct evidence of boosted oxygen evolution over perovskite by enhanced lattice oxygen participation. Nat. Commun. *11*, 2002. https://doi.org/10.1038/s41467-020-15873-x.

Peng, Y., Lu, B., Chen, L., Wang, N., Lu, J.E., Ping, Y., and Chen, S. (2017). Hydrogen evolution reaction catalyzed by ruthenium ion-complexed graphitic carbon nitride nanosheets. J. Mater. Chem. A *5*, 18261–18269. https://doi.org/10.1039/c7ta03826g.

Qiao, B., Wang, A., Yang, X., Allard, L.F., Jiang, Z., Cui, Y., Liu, J., Li, J., and Zhang, T. (2011). Single-atom catalysis of CO oxidation using Pt_1/FeOx. Nat. Chem. *3*, 634–641. https://doi.org/10.1038/nchem.1095.

Qiao, B., Liang, J.-X., Wang, A., Xu, C.-Q., Li, J., Zhang, T., and Liu, J.J. (2015). Ultrastable single-atom gold catalysts with strong covalent metal-support interaction (CMSI). Nano Res. *8*, 2913–2924. https://doi.org/10.1007/s12274-015-0796-9.

Ren, S., Yu, Q., Yu, X., Rong, P., Jiang, L., and Jiang, J. (2020). Graphene-supported metal single-atom catalysts: a concise review. Sci. China Mater. *63*, 903–920. https://doi.org/10.1007/s40843-019-1286-1.

Rong, X., Parolin, J., and Kolpak, A.M. (2016). A fundamental relationship between reaction mechanism and stability in metal oxide catalysts for oxygen evolution. ACS Catal. *6*, 1153–1158. https://doi.org/10.1021/acscatal.5b02432.

Rossmeisl, J., Qu, Z.W., Zhu, H., Kroes, G.J., and Nørskov, J.K. (2007). Electrolysis of water on oxide surfaces. J. Electroanal. Chem. *607*, 83–89. https://doi.org/10.1016/j.jelechem.2006.11.008.

Sabatier, P. (1920). La catalyse en chimie organique (Librairie polytechnique).

Shaik, S.A., Goswami, A., Varma, R.S., and Gawande, M.B. (2019). Nitrogen-doped nanocarbons (NNCs): current status and future opportunities. Curr. Opin. Green Sustain. Chem. *15*, 67–76. https://doi.org/10.1016/j.cogsc.2018.10.001.

Shang, H., Zhou, X., Dong, J., Li, A., Zhao, X., Liu, Q., Lin, Y., Pei, J., Li, Z., Jiang, Z., et al. (2020). Engineering unsymmetrically coordinated $Cu-S_1N_3$ single atom sites with enhanced oxygen reduction activity. Nat. Commun. *11*, 3049. https://doi.org/10.1038/s41467-020-16848-8.

Sheng, W., Gasteiger, H.A., and Shao-Horn, Y. (2010). Hydrogen oxidation and evolution reaction kinetics on platinum: acid vs alkaline electrolytes. J. Electrochem. Soc. *157*, B1529. https://doi.org/10.1149/1.3483106.

Skúlason, E., Tripkovic, V., Björketun, M.E., Gudmundsdóttir, S., Karlberg, G., Rossmeisl, J., Bligaard, T., Jónsson, H., and Nørskov, J.K. (2010). Modeling the electrochemical hydrogen oxidation and evolution reactions on the basis of density functional theory calculations. J. Phys. Chem. C *114*, 18182–18197. https://doi.org/10.1021/jp1048887.

Song, X., Zhang, H., Yang, Y., Zhang, B., Zuo, M., Cao, X., Sun, J., Lin, C., Li, X., and Jiang, Z. (2018). Bifunctional nitrogen and cobalt codoped hollow carbon for electrochemical syngas production. Adv. Sci. *5*, 1800177. https://doi.org/10.1002/advs.201800177.

Song, P., Wang, H., Kang, L., Ran, B., Song, H., and Wang, R. (2019). Electrochemical nitrogen reduction to ammonia at ambient conditions on nitrogen and phosphorus co-doped porous carbon. Chem. Commun. *55*, 687–690. https://doi.org/10.1039/c8cc09256g.

Su, D.S., Perathoner, S., and Centi, G. (2013). Nanocarbons for the development of advanced catalysts. Chem. Rev. *113*, 5782–5816. https://doi.org/10.1021/cr300367d.

Sun, S., Zhang, G., Gauquelin, N., Chen, N., Zhou, J., Yang, S., Chen, W., Meng, X., Geng, D., Banis, M.N., et al. (2013). Single-atom catalysis using Pt/graphene achieved through atomic layer deposition. Scientific Rep. *3*, 1775. https://doi.org/10.1038/srep01775.

Sun, Q., Wang, N., Zhang, T., Bai, R., Mayoral, A., Zhang, P., Zhang, Q., Terasaki, O., and Yu, J. (2019a). Zeolite-encaged single-atom rhodium catalysts: highly-efficient hydrogen generation and shape-selective tandem hydrogenation of nitroarenes. Angew. Chem. Int. Ed. Engl. *58*, 18570–18576. https://doi.org/10.1002/ange.201912367.

Sun, T., Xu, L., Wang, D., and Li, Y. (2019b). Metal organic frameworks derived single atom catalysts for electrocatalytic energy conversion. Nano Res. *12*, 2067–2080. https://doi.org/10.1007/s12274-019-2345-4.

Sun, Y., Silvioli, L., Sahraie, N.R., Ju, W., Li, J., Zitolo, A., Li, S., Bagger, A., Arnarson, L., Wang, X., et al. (2019c). Activity-selectivity trends in the electrochemical production of hydrogen peroxide over single-site metal-nitrogen-carbon catalysts. J. Am. Chem. Soc. *141*, 12372–12381. https://doi.org/10.1021/jacs.9b05576.

Sun, X., Dawson, S.R., Parmentier, T.E., Malta, G., Davies, T.E., He, Q., Lu, L., Morgan, D.J., Carthey, N., Johnston, P., et al. (2020). Facile synthesis of precious-metal single-site catalysts using organic solvents. Nat. Chem. *12*, 560–567. https://doi.org/10.1038/s41557-020-0446-z.

Sun, Y.L., Yue, M.F., Chen, H.Q., Ze, H., Wang, Y.H., Dong, J.C., Tian, Z.Q., Fang, P.P., and Li, J.F. (2022). Exploring the effect of pd on the oxygen reduction performance of Pt by in situ Raman spectroscopy. Anal. Chem. *94*, 4779–4786. https://doi.org/10.1021/acs.analchem.1c05566.

Tang, J., Salunkhe, R.R., Liu, J., Torad, N.L., Imura, M., Furukawa, S., and Yamauchi, Y. (2015). Thermal conversion of core–shell metal–organic frameworks: a new method for selectively functionalized nanoporous hybrid carbon. J. Am. Chem. Soc. *137*, 1572–1580. https://doi.org/10.1021/ja511539a.

Tao, H., Choi, C., Ding, L.-X., Jiang, Z., Han, Z., Jia, M., Fan, Q., Gao, Y., Wang, H., Robertson, A.W., et al. (2019). Nitrogen fixation by ru single-atom electrocatalytic reduction. Chem *5*, 204–214. https://doi.org/10.1016/j.chempr.2018.10.007.

Tao, L., Wang, Y., Zou, Y., Zhang, N., Zhang, Y., Wu, Y., Wang, Y., Chen, R., and Wang, S. (2020). Charge transfer modulated activity of carbon-based electrocatalysts. Adv. Energy Mater. *10*, 1901227. https://doi.org/10.1002/aenm.201901227.

Tavakkoli, M., Flahaut, E., Peljo, P., Sainio, J., Davodi, F., Lobiak, E.V., Mustonen, K., and Kauppinen, E.I. (2020). Mesoporous single-atom-doped graphene–carbon nanotube hybrid: synthesis and tunable electrocatalytic activity for oxygen evolution and reduction reactions. ACS Catal. *10*, 4647–4658. https://doi.org/10.1021/acscatal.0c00352.

Tong, M., Sun, F., Xie, Y., Wang, Y., Yang, Y., Tian, C., Wang, L., and Fu, H. (2021). Operando cooperated catalytic mechanism of atomically dispersed $Cu-N_4$ and $Zn-N_4$ for promoting oxygen reduction reaction. Angew. Chem. Int. Ed. Engl. *60*, 14005–14012. https://doi.org/10.1002/ange.202102053.

van der Ham, C.J.M., Koper, M.T.M., and Hetterscheid, D.G.H. (2014a). Challenges in reduction of dinitrogen by proton and electron transfer. Chem. Soc. Rev. *43*, 5183–5191. https://doi.org/10.1039/c4cs00085d.

van der Ham, C.J.M., Koper, M.T.M., and Hetterscheid, D.G.H. (2014b). Challenges in reduction of dinitrogen by proton and electron transfer. Chem. Soc. Rev. *43*, 5183–5191. https://doi.org/10.1039/c4cs00085d.

Voiry, D., Yamaguchi, H., Li, J., Silva, R., Alves, D.C.B., Fujita, T., Chen, M., Asefa, T., Shenoy, V.B., Eda, G., and Chhowalla, M. (2013). Enhanced catalytic activity in strained chemically exfoliated WS_2 nanosheets for hydrogen evolution. Nat. Mater. *12*, 850–855. https://doi.org/10.1038/nmat3700.

Wang, X.-D., Xu, Y.-F., Rao, H.-S., Xu, W.-J., Chen, H.-Y., Zhang, W.-X., Kuang, D.-B., and Su, C.-Y. (2016). Novel porous molybdenum tungsten phosphide hybrid nanosheets on carbon cloth for efficient hydrogen evolution. Energy Environ. Sci. *9*, 1468–1475. https://doi.org/10.1039/c5ee03801d.

Wang, S., Hai, X., Ding, X., Chang, K., Xiang, Y., Meng, X., Yang, Z., Chen, H., and Ye, J. (2017). Light-switchable oxygen vacancies in ultrafine Bi_5O_7Br nanotubes for boosting solar-driven nitrogen fixation in pure water. Adv. Mater. *29*, 1701774. https://doi.org/10.1002/adma.201701774.

Wang, J., Li, Z., Wu, Y., and Li, Y. (2018a). Fabrication of single-atom catalysts with precise structure and high metal loading. Adv. Mater. *30*, e1801649. https://doi.org/10.1002/adma.201801649.

Wang, X., Chen, Z., Zhao, X., Yao, T., Chen, W., You, R., Zhao, C., Wu, G., Wang, J., Huang, W., et al. (2018b). Regulation of coordination number over single Co sites: triggering the efficient electroreduction of CO_2. Angew. Chem. Int. Ed. Engl. *57*, 1944–1948. https://doi.org/10.1002/ange.201712451.

Wang, D., Li, Q., Han, C., Xing, Z., and Yang, X. (2019). Single-atom ruthenium based catalyst for enhanced hydrogen evolution. Appl. Catal. B Environ. *249*, 91–97. https://doi.org/10.1016/j.apcatb.2019.02.059.

Wang, L., Li, Z., Wang, K., Dai, Q., Lei, C., Yang, B., Zhang, Q., Lei, L., Leung, M.K., and Hou, Y. (2020). Tuning d-band center of tungsten carbide

via Mo doping for efficient hydrogen evolution and Zn–H_2O cell over a wide pH range. Nano Energy *74*, 104850. https://doi.org/10.1016/j.nanoen.2020.104850.

Wei, H., Huang, K., Wang, D., Zhang, R., Ge, B., Ma, J., Wen, B., Zhang, S., Li, Q., Lei, M., et al. (2017). Iced photochemical reduction to synthesize atomically dispersed metals by suppressing nanocrystal growth. Nat. Commun. *8*, 1490. https://doi.org/10.1038/s41467-017-01521-4.

Wei, J., Qin, S.N., Yang, J., Ya, H.L., Huang, W.H., Zhang, H., Hwang, B.J., Tian, Z.Q., and Li, J.F. (2021a). Probing single-atom catalysts and catalytic reaction processes by shell-isolated nanoparticle-enhanced Raman spectroscopy. Angew. Chem. Int. Ed. Engl. *60*, 9306–9310. https://doi.org/10.1002/ange.202100198.

Wei, P., Sun, X., Wang, M., Xu, J., He, Z., Li, X., Cheng, F., Xu, Y., Li, Q., Han, J., et al. (2021b). Construction of an N-decorated carbon-encapsulated W_2C/WP heterostructure as an efficient electrocatalyst for hydrogen evolution in both alkaline and acidic media. ACS Appl. Mater. Inter. *13*, 53955–53964. https://doi.org/10.1021/acsami.1c16547.

Willsau, J., Wolter, O., and Heitbaum, J. (1985). Does the oxide layer take part in the oxygen evolution reaction on platinum?: a DEMS study. J. Electroanal. Chem. Inter. Electrochem. *195*, 299–306. https://doi.org/10.1016/0022-0728(85)80050-4.

Wohlfahrt-Mehrens, M., and Heitbaum, J. (1987). Oxygen evolution on Ru and RuO_2 electrodes studied using isotope labelling and on-line mass spectrometry. J. Electroanal. Chem. Inter. Electrochem. *237*, 251–260. https://doi.org/10.1016/0022-0728(87)85237-3.

Wu, H., Li, H., Zhao, X., Liu, Q., Wang, J., Xiao, J., Xie, S., Si, R., Yang, F., Miao, S., et al. (2016). Highly doped and exposed Cu(i)–N active sites within graphene towards efficient oxygen reduction for zinc–air batteries. Energy Environ. Sci. *9*, 3736–3745. https://doi.org/10.1039/c6ee01867j.

Xia, W., Mahmood, A., Zou, R., and Xu, Q. (2015). Metal–organic frameworks and their derived nanostructures for electrochemical energy storage and conversion. Energy Environ. Sci. *8*, 1837–1866. https://doi.org/10.1039/c5ee00762c.

Xia, B.Y., Yan, Y., Li, N., Wu, H.B., Lou, X.W., and Wang, X. (2016). A metal–organic framework-derived bifunctional oxygen electrocatalyst. Nat. Energy *1*, 15006. https://doi.org/10.1038/nenergy.2015.6.

Xia, C., Qiu, Y., Xia, Y., Zhu, P., King, G., Zhang, X., Wu, Z., Kim, J.Y.T., Cullen, D.A., Zheng, D., et al. (2021). General synthesis of single-atom catalysts with high metal loading using graphene quantum dots. Nat. Chem. *13*, 887–894. https://doi.org/10.1038/s41557-021-00734-x.

Xiao, M., Zhu, J., Li, G., Li, N., Li, S., Cano, Z.P., Ma, L., Cui, P., Xu, P., Jiang, G., et al. (2019). A single-atom iridium heterogeneous catalyst in oxygen reduction reaction. Angew. Chem. Int. Ed. Engl. *58*, 9640–9645. https://doi.org/10.1002/anie.201905241.

Xing, Z., Liu, Q., Asiri, A.M., and Sun, X. (2015). High-efficiency electrochemical hydrogen evolution catalyzed by tungsten phosphide submicroparticles. ACS Catal. *5*, 145–149. https://doi.org/10.1021/cs5014943.

Xiong, Y., Dong, J., Huang, Z.Q., Xin, P., Chen, W., Wang, Y., Li, Z., Jin, Z., Xing, W., Zhuang, Z., et al. (2020). Single-atom Rh/N-doped carbon electrocatalyst for formic acid oxidation. Nat. Nanotechnol. *15*, 390–397. https://doi.org/10.1038/s41565-020-0665-x.

Xue, Y., Huang, B., Yi, Y., Guo, Y., Zuo, Z., Li, Y., Jia, Z., Liu, H., and Li, Y. (2018). Anchoring zero valence single atoms of nickel and iron on graphdiyne for hydrogen evolution. Nat. Commun. *9*, 1460. https://doi.org/10.1038/s41467-018-03896-4.

Yan, H., Cheng, H., Yi, H., Lin, Y., Yao, T., Wang, C., Li, J., Wei, S., and Lu, J. (2015a). Single-atom Pd(1)/graphene catalyst achieved by atomic layer deposition: remarkable performance in selective hydrogenation of 1,3-butadiene. J. Am. Chem. Soc. *137*, 10484–10487. https://doi.org/10.1021/jacs.5b06485.

Yan, H., Tian, C., Wang, L., Wu, A., Meng, M., Zhao, L., and Fu, H. (2015b). Phosphorus-modified tungsten nitride/reduced graphene oxide as a high-performance, non-noble-metal electrocatalyst for the hydrogen evolution reaction. Angew. Chem. *127*, 6423–6427. https://doi.org/10.1002/ange.201501419.

Yan, C., Li, H., Ye, Y., Wu, H., Cai, F., Si, R., Xiao, J., Miao, S., Xie, S., Yang, F., et al. (2018a). Coordinatively unsaturated nickel–nitrogen sites towards selective and high-rate CO_2 electroreduction. Energy Environ. Sci. *11*, 1204–1210. https://doi.org/10.1039/c8ee00133b.

Yan, H., Zhao, X., Guo, N., Lyu, Z., Du, Y., Xi, S., Guo, R., Chen, C., Chen, Z., Liu, W., et al. (2018b). Atomic engineering of high-density isolated Co atoms on graphene with proximal-atom controlled reaction selectivity. Nat. Commun. *9*, 3197. https://doi.org/10.1038/s41467-018-05754-9.

Yang, X.-F., Wang, A., Qiao, B., Li, J., Liu, J., and Zhang, T. (2013). Single-atom catalysts: a new Frontier in heterogeneous catalysis. Acc. Chem. Res. *46*, 1740–1748. https://doi.org/10.1021/ar300361m.

Yang, H.B., Hung, S.-F., Liu, S., Yuan, K., Miao, S., Zhang, L., Huang, X., Wang, H.-Y., Cai, W., Chen, R., et al. (2018a). Atomically dispersed Ni(i) as the active site for electrochemical CO_2 reduction. Nat. Energy *3*, 140–147. https://doi.org/10.1038/s41560-017-0078-8.

Yang, J., Chen, B., Liu, X., Liu, W., Li, Z., Dong, J., Chen, W., Yan, W., Yao, T., Duan, X., et al. (2018b). Efficient and robust hydrogen evolution: phosphorus nitride imide nanotubes as supports for anchoring single ruthenium sites. Angew. Chem. Int. Ed. Engl. *57*, 9495–9500. https://doi.org/10.1002/ange.201804854.

Yang, H., Shang, L., Zhang, Q., Shi, R., Waterhouse, G.I.N., Gu, L., and Zhang, T. (2019a). A universal ligand mediated method for large scale synthesis of transition metal single atom catalysts. Nat. Commun. *10*, 4585. https://doi.org/10.1038/s41467-019-12510-0.

Yang, S., Yu, Y., Dou, M., Zhang, Z., Dai, L., and Wang, F. (2019b). Two-dimensional conjugated aromatic networks as high-site-density and single-atom electrocatalysts for the oxygen reduction reaction. Angew. Chem. Int. Ed. Engl. *58*, 14724–14730. https://doi.org/10.1002/ange.201908023.

Yang, C., Zhu, Y., Liu, J., Qin, Y., Wang, H., Liu, H., Chen, Y., Zhang, Z., and Hu, W. (2020a). Defect engineering for electrochemical nitrogen reduction reaction to ammonia. Nano Energy *77*, 105126. https://doi.org/10.1016/j.nanoen.2020.105126.

Yang, Y., Yang, Y., Pei, Z., Wu, K.-H., Tan, C., Wang, H., Wei, L., Mahmood, A., Yan, C., Dong, J., et al. (2020b). Recent progress of carbon-supported single-atom catalysts for energy conversion and storage. Matter *3*, 1442–1476. https://doi.org/10.1016/j.matt.2020.07.032.

Ye, S., Luo, F., Zhang, Q., Zhang, P., Xu, T., Wang, Q., He, D., Guo, L., Zhang, Y., He, C., et al. (2019). Highly stable single Pt atomic sites anchored on aniline-stacked graphene for hydrogen evolution reaction. Energy Environ. Sci. *12*, 1000–1007. https://doi.org/10.1039/c8ee02888e.

Yin, P., Yao, T., Wu, Y., Zheng, L., Lin, Y., Liu, W., Ju, H., Zhu, J., Hong, X., Deng, Z., et al. (2016). Single cobalt atoms with precise N-Coordination as superior oxygen reduction reaction Catalysts. Angew. Chem. Int. Ed. Engl. *55*, 10800–10805. https://doi.org/10.1002/ange.201604802.

Yin, X.P., Wang, H.J., Tang, S.F., Lu, X.L., Shu, M., Si, R., and Lu, T.B. (2018). Engineering the coordination environment of single-atom platinum anchored on graphdiyne for optimizing electrocatalytic hydrogen evolution. Angew. Chem. Int. Ed. Engl. *57*, 9382–9386. https://doi.org/10.1002/ange.201804817.

Yoo, J.S., Rong, X., Liu, Y., and Kolpak, A.M. (2018). Role of lattice oxygen participation in understanding trends in the oxygen evolution reaction on perovskites. ACS Catal. *8*, 4628–4636. https://doi.org/10.1021/acscatal.8b00612.

You, B., Jiang, N., Sheng, M., Drisdell, W.S., Yano, J., and Sun, Y. (2015). Bimetal–organic framework self-adjusted synthesis of support-free nonprecious electrocatalysts for efficient oxygen reduction. ACS Catal. *5*, 7068–7076. https://doi.org/10.1021/acscatal.5b02325.

Yuan, M., Shi, G., Xie, Y., Du, L., Fu, X., Chen, X., Xie, W., Lu, T.B., and Wang, M. (2022). Constructing Cu-C bond in graphdiyne-regulated Cu single atom electrocatalyst for CO_2 reduction to CH_4. Angew. Chem. Int. Ed. Engl.. e202203569.

Zamfirescu, C., and Dincer, I. (2008). Using ammonia as a sustainable fuel. J. Power Sourc. *185*, 459–465. https://doi.org/10.1016/j.jpowsour.2008.02.097.

Zang, W., Yang, T., Zou, H., Xi, S., Zhang, H., Liu, X., Kou, Z., Du, Y., Feng, Y.P., Shen, L., et al. (2019). Copper single atoms anchored in porous nitrogen-doped carbon as efficient ph-universal catalysts for the nitrogen reduction reaction. ACS Catal. *9*, 10166–10173. https://doi.org/10.1021/acscatal.9b02944.

Zeradjanin, A.R., Grote, J.-P., Polymeros, G., and Mayrhofer, K.J.J. (2016). A critical review on

hydrogen evolution electrocatalysis: Re-exploring the volcano-relationship. Electroanalysis *28*, 2256–2269. https://doi.org/10.1002/elan.201600270.

Zhang, C., Sha, J., Fei, H., Liu, M., Yazdi, S., Zhang, J., Zhong, Q., Zou, X., Zhao, N., Yu, H., et al. (2017a). Single-atomic ruthenium catalytic sites on nitrogen-doped graphene for oxygen reduction reaction in acidic medium. ACS Nano *11*, 6930–6941. https://doi.org/10.1021/acsnano.7b02148.

Zhang, H., Hwang, S., Wang, M., Feng, Z., Karakalos, S., Luo, L., Qiao, Z., Xie, X., Wang, C., Su, D., et al. (2017b). Single atomic iron catalysts for oxygen reduction in acidic media: particle size control and thermal activation. J. Am. Chem. Soc. *139*, 14143–14149. https://doi.org/10.1021/jacs.7b06514.

Zhang, L., Jia, Y., Gao, G., Yan, X., Chen, N., Chen, J., Soo, M.T., Wood, B., Yang, D., Du, A., and Yao, X. (2018). Graphene defects trap atomic ni species for hydrogen and oxygen evolution reactions. Chem *4*, 285–297. https://doi.org/10.1016/j.chempr.2017.12.005.

Zhang, Y., Yao, Y., Sendeku, M.G., Yin, L., Zhan, X., Wang, F., Wang, Z., and He, J. (2019). Recent progress in CVD growth of 2D transition metal dichalcogenides and related heterostructures. Adv. Mater. *31*. e1901694. https://doi.org/10.1002/adma.201901694.

Zhang, Z., Feng, C., Liu, C., Zuo, M., Qin, L., Yan, X., Xing, Y., Li, H., Si, R., Zhou, S., and Zeng, J. (2020). Electrochemical deposition as a universal route for fabricating single-atom catalysts. Nat. Commun. *11*, 1215. https://doi.org/10.1038/s41467-020-14917-6.

Zhao, C., Dai, X., Yao, T., Chen, W., Wang, X., Wang, J., Yang, J., Wei, S., Wu, Y., and Li, Y. (2017). Ionic exchange of metal-organic frameworks to access single nickel sites for efficient electroreduction of CO_2. J. Am. Chem. Soc. *139*, 8078–8081. https://doi.org/10.1021/jacs.7b02736.

Zhao, L., Zhang, Y., Huang, L.B., Liu, X.Z., Zhang, Q.H., He, C., Wu, Z.Y., Zhang, L.J., Wu, J., Yang, W., et al. (2019). Cascade anchoring strategy for general mass production of high-loading single-atomic metal-nitrogen catalysts. Nat. Commun. *10*, 1278. https://doi.org/10.1038/s41467-019-09290-y.

Zheng, F., Yang, Y., and Chen, Q. (2014). High lithium anodic performance of highly nitrogen-doped porous carbon prepared from a metal-organic framework. Nat. Commun. *5*, 5261. https://doi.org/10.1038/ncomms6261.

Zheng, Y., Jiao, Y., Jaroniec, M., and Qiao, S.Z. (2015). Advancing the electrochemistry of the hydrogen-evolution reaction through combining experiment and theory. Angew. Chem. Int. Ed. Engl. *54*, 52–65. https://doi.org/10.1002/anie.201407031.

Zheng, W., Yang, J., Chen, H., Hou, Y., Wang, Q., Gu, M., He, F., Xia, Y., Xia, Z., Li, Z., et al. (2019). Atomically defined undercoordinated active sites for highly efficient CO_2 electroreduction. Adv. Funct. Mater. *30*, 1907658. https://doi.org/10.1002/adfm.201907658.

Zhou, Y., Sun, S., Wei, C., Sun, Y., Xi, P., Feng, Z., and Xu, Z.J. (2019). Significance of engineering the octahedral units to promote the oxygen evolution reaction of spinel oxides. Adv. Mater. *31*. e1902509. https://doi.org/10.1002/adma.201902509.

Zhou, D., Li, X., Shang, H., Qin, F., and Chen, W. (2021a). Atomic regulation of metal–organic framework derived carbon-based single-atom catalysts for the electrochemical CO_2 reduction reaction. J. Mater. Chem. A *9*, 23382–23418. https://doi.org/10.1039/d1ta06915b.

Zhou, F., Yu‡, P., Sun, F., Zhang, G., Liu, X., and Wang, L. (2021b). The cooperation of Fe_3C nanoparticles with isolated single iron atoms to boost the oxygen reduction reaction for Zn–air batteries. J. Mater. Chem. A *9*, 6831–6840. https://doi.org/10.1039/d1ta00039j.

Zhu, Y., Cao, D., Liu, N., and Cheng, D. (2021). One-step synthesis of atomic Ru doped ultra-thin $Co(OH)_2$ nanosheets for oxygen evolution reaction in different pH values. Int. J. Hydrogen Energy *46*, 22832–22841. https://doi.org/10.1016/j.ijhydene.2021.04.088.